ANALYSIS OF PMSM MANUFACTURED USING SEGMENTED STATOR MADE FROM ORIENTED STEEL

By

Anmol Aggarwal

A DISSERTATION

Submitted to
Michigan State University
in partial fulfillment of the requirements
for the degree of

Electrical Engineering - Doctor of Philosophy

2021

ABSTRACT

ANALYSIS OF PMSM MANUFACTURED USING SEGMENTED STATOR MADE FROM ORIENTED STEEL

By

Anmol Aggarwal

Segmented stators ease the winding process, increase slot fill factor, and improve handling and assembly. Segmented stator construction also allows oriented steel with superior magnetic properties, higher permeability, and lower losses in orientation, also known as rolling direction. Therefore, using oriented steel for the segmented stator construction of PMSM may improve machine performance compared to a machine designed with non-oriented steel, such as an increase in average torque and efficiency.

Apart from the clear advantages of segmentation, the increased number of segments increases the unavoidable parasitic gaps between the segments, adversely affecting machine performance. Moreover, oriented steel modeling in modern FEA software is inaccurate, as shown in the literature. An improved model was proposed in the literature to resolve this issue, which requires magnetic properties of the oriented steel in between the rolling and transverse directions. This research aims to analyze the performance of the oriented steel segmented stator PMSM and compare it with conventional non-oriented steel stator PMSM.

In this research, the magnetic properties of the oriented steel are determined using a devised experimental setup method. In the proposed method, the flux density of controlled amplitude and frequency is imposed in the oriented steel segmented stator using specially designed devices to estimate the BH and loss curves of the oriented steel. The advantage of the proposed method is that it is comparatively less expensive than the specially modified Epstein frame test. Further, a general theory is proposed to determine the impact of

segmentation parameters on the selected performance measures: core losses, average torque, cogging torque, and Back electromotive force. Finally, the estimated magnetic properties of the oriented steel are used to model the oriented steel segmented stator PMSM, and its performance is compared with that of the conventional machine.

The experimentally-estimated magnetic characteristics of the oriented steel are different from those estimated using the FEA method. Further, the theory to show the impact of segmentation parameters on the machine performance is validated using numerical experiments on two different machine designs with 72 slots/12 poles and 72 slots/8 poles. The estimated properties are used to model the oriented steel segmented stator PMSM with 72 slots/12 poles. Its performance, with different combinations of segment size and parasitic gap, is compared with conventional stator PMSM of the same design at the same drive cycle. For some segment sizes, the segmented stator machine has lower losses. Moreover, the segmented stator machine has higher cogging torque for all segment sizes and unbalanced BEMF for specific segment sizes.

To my parents
Sushma and Rajeev
and sister
Pallavi
for their love and support through this life journey

ACKNOWLEDGMENTS

First, I would like to express my sincere gratitude and appreciation to Dr. Elias Strangas for his patience, constant guidance, encouragement, and support in helping me to complete my Ph.D. program and to become a researcher. I'd like to also thank Dr. Shanelle Foster, Dr. Ranjan Mukherjee, and Dr. Woongkul Lee for their time, support, teaching, and guidance as part of my committee and helped me complete my program.

I'd also like to thank members of the Electric Machines and Power Electronics Research (EMPowER) Laboratory at Michigan State University. Thank you, Dr. Reemon Haddad, Cristián López-Martínez, Abdullah Alfehaid, Dr. Thang Pham, Dr. William Jensen, Bhuvan Khosoo, Orwell Madovi, Prathima Nuli, Dr. Heinrich Eickhoff, Dr. Rodney Singleton, Dr. Matt Woongkul Lee, Dr. Shaopo Hwang, Dr. José Vitor B. Junior, Tiraruek Ruekamnuaychok, Tia Smith, Lauren Kalizewski, Josh Ward, and Shubham Shedge.

I'd like to specifically thank Dr. John Agapiou from General Motors Global Technical Center, Warren, MI, who helped and assisted me in all my projects. His assistance aided me tremendously towards the completion of my work. Moreover, I'd like to extend my gratitude towards Steve Hayslett and Matt Meier for helping me throughout difficult times, attending my late-night calls, and being patient with my research questions that were beyond my understanding.

I would also like to thank members of the Department of Electrical and Computer Engineering for helping me complete my degree. Thank you, Brian Wright, Gregg Mulder, Meagan Kroll, Roxanne Peacock, Michelle Stewart, and Laurie Rashid.

I want to dedicate my work to my mother Sushma, father Rajeev, and sister Pallavi. Additionally, I would like to thank my cousins Sandeep Aggarwal and Naveen Aggarwal

for motivating me to pursue my post-graduation studies. Finally, I would like to thank my friends back home, Gaurav and Prince, they were always there when my parents needed them.

TABLE OF CONTENTS

LIST OF TABLES

LIST OF FIGURES

Chapter 1

Introduction

1.1 Motivation

Segmenting the stator core allows the possibility to simplify the winding process, to increase slot fill factor and ease of handling and assembling [1]. Segmented stator design enables the use of different materials for stator and rotor with lower waste. Hence, it assists the construction of stator using lower loss magnetic steel and construction of rotor using higher tensile strength material, as required by the high-speed operation. Due to separate production of the rotor and the stator laminations, the air gap width is no longer determined by limitations of the punching tool, and hence air gap can be further reduced; this can further aid in the increase of the torque density of the machine. Faults may lead to vibrations [2] or adverse effects on the operation of the machine. They may lead to catastrophic effects on the safety of the human [3–9]. High fault tolerance is achieved in segmented stator construction due to physical separation between the segments [10]. Segmented stator construction also allows oriented steel to show superior magnetic properties, higher permeability, and lower core losses in the rolling direction [11–13]. Therefore, the proper design of oriented steel segments for the stator construction may enhance machine performance and provide other advantages of modular stator construction.

1.2 Problem Statement and Objective

Oriented steel has higher permeability and lower losses in orientation (the rolling direction) than non-oriented steel. However, in the transverse direction, oriented steel typically has lower permeability and higher losses. Strategic use of oriented steel in a modular PMSM stator can improve machine performance by increasing torque and efficiency compared to a machine designed with non-oriented steel. Typically, steel manufacturers provide magnetic properties in the rolling and transverse directions only. Furthermore, in modern FEA software, the magnetic properties between the rolling and transverse directions are interpolated using an intrinsic mathematical model. However, this interpolation method has been shown to be inaccurate. To resolve this issue, an improved model was proposed in the literature. This model requires magnetic properties of the oriented steel in between the rolling and transverse directions; therefore, a method to extract the magnetic properties of oriented steel in different directions is required. Moreover, due to manufacturing limits, parasitic air gaps are introduced between the segments; this changes the magnetic circuit of the machine, adversely affecting its performance.

The objective of the work is to develop and validate a method to determine the magnetic properties of oriented steel beyond just the oriented and transverse directions. Further, propose a theory to determine the impact of segmentation parameters on the performance of the machine. Finally, using the estimated properties to model oriented steel segmented stator PMSM, analyze the machine's performance, and compare it with the conventional, non-oriented steel stator machine.

1.3 Literature Review

1.3.1 Types of Stator and Rotor Segmentation

Depending on the operation, manufacturing requirement, and on-site assembly of the machine, stator and rotor segmentation are performed differently. This section discusses some of the modular designs and their advantages for both stators and rotors.

1.3.1.1 Segmentation of Stator for Different Winding Configuration

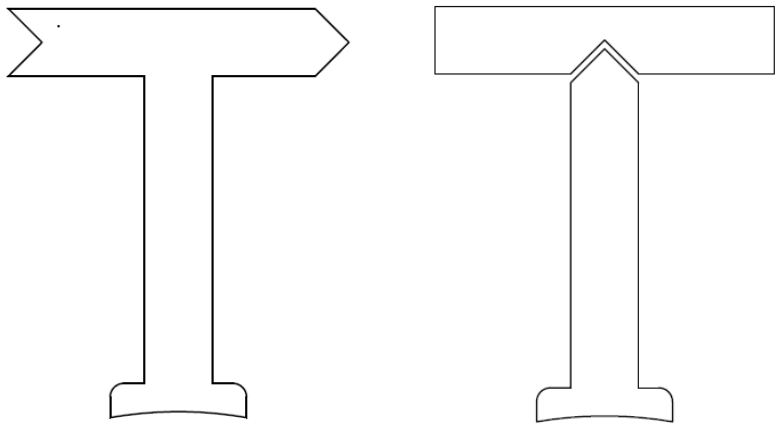

(a) Circumferential segmentation

(b) Radial segmentation

Figure 1.1: Segmented stator designs used for concentrated winding machine.

Depending on the winding, the segmented stator design is selected to ease the winding process and also increase the slotting fill factor. Fig.1.1 shows the topologies for the concentrated winding. Fig.1.1(a) shows a segment in which one single tooth is constructed, and the adjacent segments are interconnected in the back-iron while the topology of Fig.1.1(b) shows how single teeth are inserted in the yoke [14]. In both segmentation, during assembly of the segments, mechanical stresses are introduced. For the topology shown in Fig.1.1(a) the stator segments are pressed in the stator housing, while Fig.1.1(b) relies on tight-fitting dovetailed

connections to provide stiffness. One more disadvantage is the presence of unavoidable air gaps due to these connections that change the permeability of the stator.

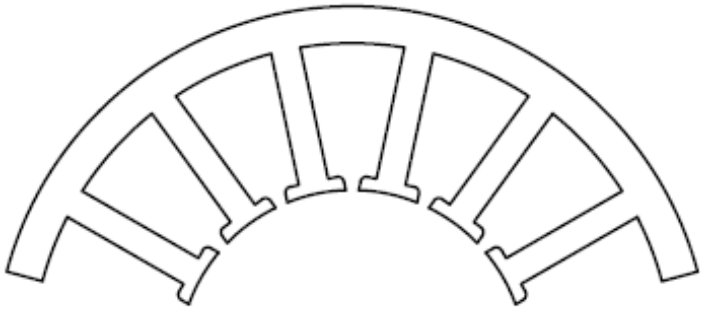

Figure 1.2: Segmented stator for distributed winding configuration.

Fig.1.2 shows the segmented stator used for distributed winding machine. This structure is essentially the distributed version of the machine shown in Fig.1.1(a). The number of phases decides the number of teeth in the stator segment in each segment that can decide the balanced operation of the machine [15].

1.3.1.2 Axial Stator Segmentation and Segmentation in Axial Flux Machines

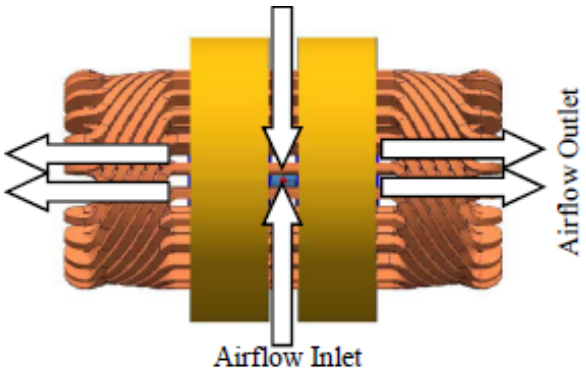

Figure 1.3: Stator build with axial segments [16].

In high speed and high power applications, the PM machines can be segmented to enhance cooling. In axial segmentation, air is forced in the stator and passes through the stator and

the windings to cool down the machine, as shown in Fig. 1.3. It was shown in [16] that axial segmentation leads to better cooling of the stator. However, due to magnet overhang at the point of segmentation, the steel saturation is increased, leading to an increase in the core losses in the stator and eddy current losses in the magnets.

In [17] segmented stator construction was utilized for axial-flux switched reluctance motor (AFSRM). In this machine, the stator teeth are made from grain-oriented electrical steel(GOES) to utilize the excellent property of the steel in the rolling direction that helps improve the machine's performance. The stator teeth are fully inserted in the stator yoke as shown in Fig.1.4.

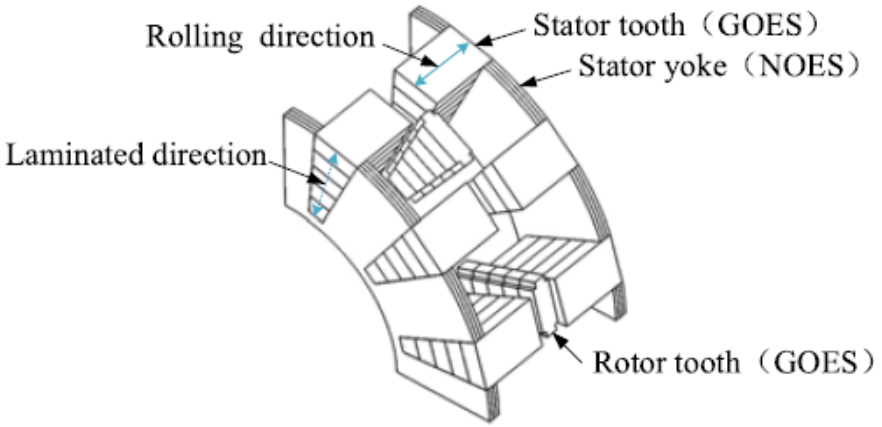

Figure 1.4: AFSRM built with axially segmented stator [17].

1.3.1.3 Removing Some Sections from the Stator for Segmentation

Some yoke sections are removed, and the segment containing the remaining section with the teeth is used to build the machine. Advantages of using this design include lightweight, reduction in punching waste, and fault tolerance capability. Since these segments do not share any common flux path, which is usually the case when the segments are connected, the problem associated with uneven air gaps between the segments is eliminated [18]. Fig.

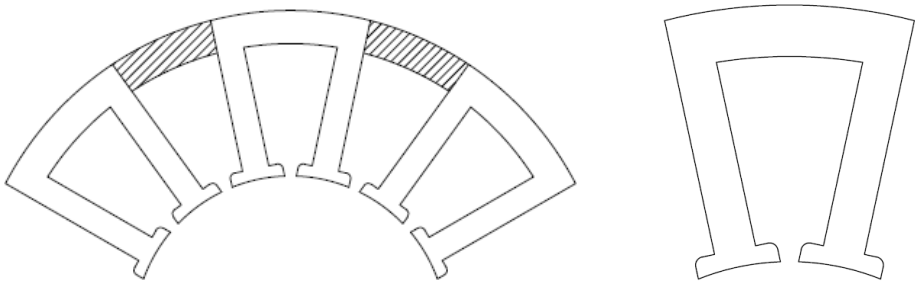

(a) (b)

Figure 1.5: Stator design as shown in (b) after removing some sections of the yoke in (a).

1.5(a) shows the stator in which shaded areas are removed to obtain segmented stator as shown in Fig. 1.5(b). A nonmagnetic frame structure mechanically retains these segments.

1.3.1.4 Rotor Segmentation

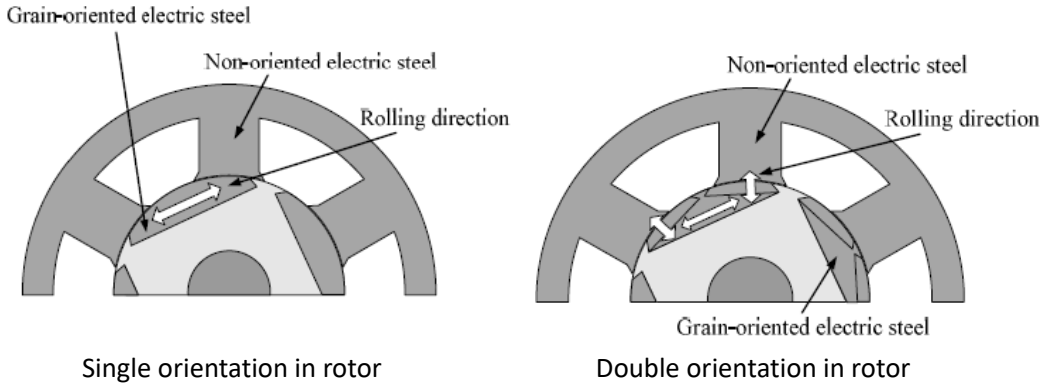

Figure 1.6: Types of orientation used in rotors of switched reluctance of the machine [19].

In switched reluctance machines (SRMs) the performance can be improved by increasing the reluctance difference between the direct and quadrature axes, leading to an increase in average torque, which is achieved by using oriented steel in the direct axis direction. In that work, two rotors were built using oriented steel, and the orientation direction was used to reduce the reluctance in the direct axis. In [19] the segmented rotor core was made of oriented electric steel that was embedded in the aluminum rotor block as shown in Fig.1.6.

The performance of the machines built with oriented steel was compared with the non-oriented steel machine, and it was shown that the efficiency of machines built with oriented steel was improved.

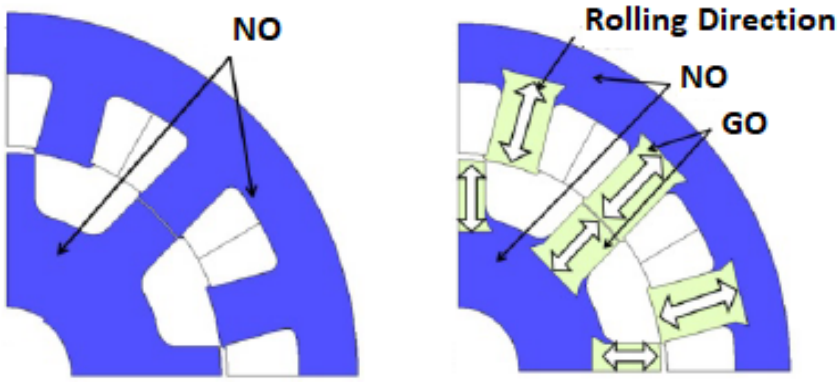

(a) Non Oriented Steel (b) Oriented Steel

Figure 1.7: Types of designs in switched reluctance machine [12].

In [12] the machine was constructed using oriented steel in the teeth of both stator and rotor as shown in Fig.1.7. The orientation direction was selected in the radial direction to reduce the reluctance of the main flux path. The two machines shown in Fig.1.7 were compared, and it was shown that the efficiency of the machine using oriented steel was improved.

1.3.2 Core Loss Reduction in the Machine Using Oriented Steel in Segmented Stator Construction

Segmented stator construction allows the use of oriented steel that offers lower losses and higher reluctance in the rolling direction in the stator as segments can be designed to use the good magnetic properties of the steel in the rolling direction. Therefore, if the stators are designed using oriented steel such that the flux path is in the direction of rolling, the losses can be minimized. In [11,14] the use of oriented steel in the construction of segmented stators

was investigated for permanent magnet synchronous machine. In [11] it was shown that the iron loss of the motor is reduced by using oriented steel in segmented stator compared to the non-oriented nonsegmented stator of the machine of the same geometry. In [14] two types of segmentation were investigated. First, yokes were segmented, and in the second case, segmentation is performed between the tooth and yoke, as shown in Fig.1.1. In both cases, the orientation is in the direction of the tooth. The losses were reduced for the same operating conditions compared to the whole stator machine design built from non-oriented steel.

Sugawara *et al.* proposed an SRM (switch reluctance machine) that was built using grain-oriented steel in the teeth of both stator and rotor, while the yoke is made of non-oriented steel that is connected to the teeth by the slight press fitting [12]. Fig.1.7 shows two models using non-oriented steel and oriented steel. Initially, the losses for two machines at high speeds are almost similar at rated torque. However, by adjusting the lamination thickness, the losses in the oriented steel were reduced compared to the non-oriented machine, and the target efficiency was achieved. From the discussion on using oriented steel in the machine for the construction of stator, it is shown that the machine's efficiency is improved. However, the research is still open for more exhaustive analysis for machines using oriented steel.

1.3.3 Effect of Segmented Stator Design on Cogging Torque

Substituting segmented stators for a single one can alter its performance, as additional air gaps due to segmentation change the permeability of the flux path in the tooth. Among other effects, this substitution changes cogging torque. Torque variation is inherent but undesirable property of Permanent Magnet Synchronous Machines (PMSMs). It has two components, cogging torque and torque ripple, that can cause vibrations, noise, or failure of

operation [20].

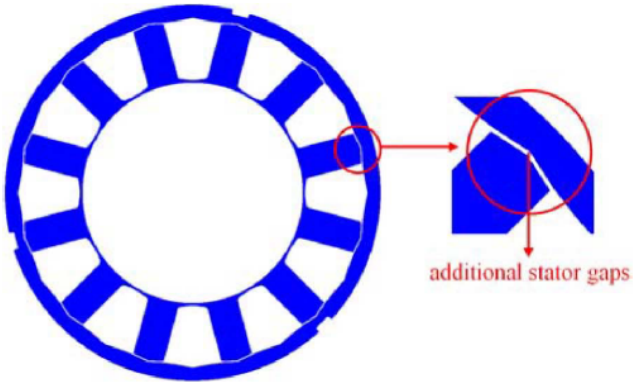

Figure 1.8: Machine used for the analysis of cogging torque [21].

Effects of segmentation on cogging torque were discussed in [21]. The tests were conducted on a 10-pole/12-slot interior PM (IPM) machine, and segmentation is shown in Fig.1.8. Due to additional stator gaps, more flux avoids tooth, and passes through slot as shown in Fig.1.9. Therefore, the cogging torque increases.

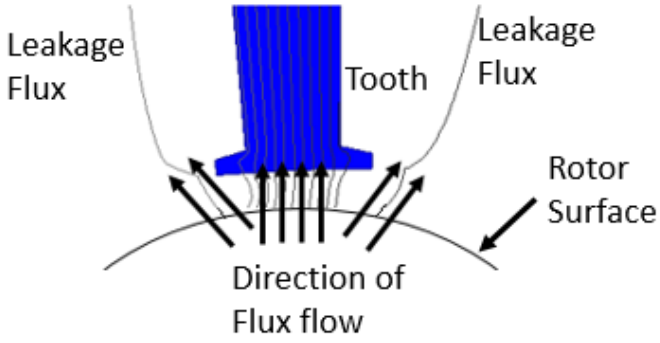

Figure 1.9: Flux lines distribution in the tooth of the stator to show the leakage due to segmentation.

Two cases, uniform and non-uniform thickness of air gap between the segments, were analyzed. In the case of uniform air gaps, the cogging torque increases with the increase in air gap length, while there is no change in the periodicity, as the interaction between

slots and poles is retained due to the symmetry of the cogging torque compared to the non-segmented machine as shown in Fig.1.10(a). The increase in the cogging torque could be compensated by skewing the rotor in steps. However, in the latter case that consists of all uniform air gaps but one, it was shown that the periodicity of the cogging torque changes; due to the interaction of higher gap with the poles as shown in Fig.1.10(b). The increase in the magnitude of the cogging torque is much larger as compared to the uniform air gap case. It was shown that simple cogging torque minimization techniques like rotor skewing could not compensate for the increased cogging torque.

In a practical scenario, the air gaps between the segments are non-uniform, which leaves an open question for the cogging torque minimization in segmented stators. As traditional cogging torque minimization design techniques in segmented stators fail, a new design technique is required.

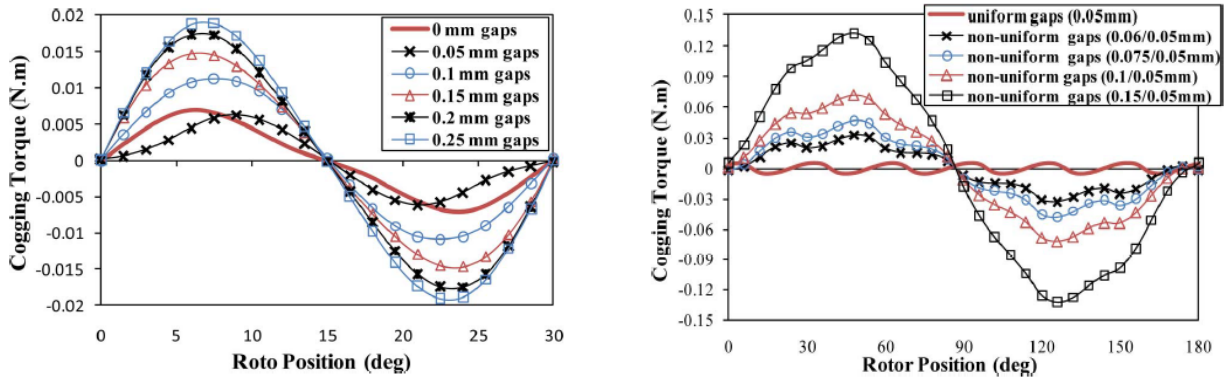

(a) Cogging torque for uniform air gaps between the segments

(b) Cogging torque for all uniform air gaps but one between the segments

Figure 1.10: Variation of cogging torque for uniform and non uniform air gaps between the segments [21].

1.3.4 Effect of Segmented Stator Design on Acoustic Noise of the Machine

Stator segmentation leads to an increase in the acoustic noise of the machine compared to its non-segmented counterpart [22,23]. It was shown in [22] that the radial forces that are developed in the machine used for analysis lead to more deformation in segmented design as compared to a non-segmented machine. In [23] a mathematical function of the radial forces acting on the segmented stator was derived. A general expression of the wavenumber of the derived force wave was obtained, and the minimum value of wavenumber is given by:

$$r_{min} = GCD(Z_s, 2p, N_s) \tag{1.1}$$

where Z_s is the number of stator slots, p is the number of pole pairs, N_s is the number of segments, and GCD is the greatest common divisor. The minimum value of wavenumber of the force wave acting on non-segmented stator is given by:

$$r_{min} = GCD(Z_s, 2p) \tag{1.2}$$

It is shown in [24] that higher values of r_{min} leads to the reduction in the vibration level as the stiffness of the yoke is higher for higher values of r_{min}. Therefore, it is clear from equations 1.1 and 1.2 that number of segments N_s affect the value of r_{min} and hence the acoustic noise. Therefore, based on the stator slots and pole pair combinations, the number of segments can be selected to increase the value of r_{min}, and hence minimize the acoustic noise of the system.

A general rule for selecting the number of circumferential segments to minimize acoustic

noise in SPMSM is proposed. However, for IPMSM, the mathematical function of the radial forces needs to be reevaluated, and the applicability of the newly derived expression must be tested. Moreover, the impact of design modifications in the stators on the acoustic noise of the segmented stator IPMSM needs to be studied.

Another effect is magnetostriction, which leads to vibrations, which was shown to be prominent in the rolling direction for the grain-oriented electrical steel as shown in [25]. Since oriented steel is commonly used in the construction of segmented stator design, machine designers need to consider noise and vibrations due to magnetostriction while using oriented steel.

1.3.5 Design Modifications to Improve the Performance in Segmented Stators

The literature shows that redesigning a non-modular machine is required if the same machine is used for modular machine construction. A study was conducted by Dajaku *et al.* for 12-slot/10-pole and 12-slot/14-pole permanent magnet machines [26] for two designs in which all or no teeth have tooth tips to determine the impact of flux gaps. It was found that for 12-slot/10-pole machine, the fundamental winding factor and on-load torque decreases due to flux gaps, whereas for 12-slot/14-pole, opposite results were obtained. Li *et al.* carried out further investigations on the modular machines and came up with a generic rule for the influence of flux gaps on machine performance [27, 28]. The developed rule states that for the machine in which the number of slots, N_s, is more than the number of poles, $2p$, ($N_s > 2p$) the presence of flux gaps decreases the average torque. However, the reverse is true for modular machines with $N_s < 2p$. In that work, no design strategy was proposed

to compensate for the decrease in average torque in modular machines for ($N_s > 2p$) due to the presence of flux gaps.

Li *et al.* continued this work for the improvement of average torque for the modular machine by changing the design of the machine [29]. To maintain a constant saturation level, the thickness of the stator width was unchanged, and the introduction of flux gaps was compensated by decreasing the slot area; this ensures that the over-saturation of the modular stator end teeth is avoided. Also, only wounded teeth were connected with tooth tips instead of using all or no teeth with tooth tips. This design variation was proposed because it was shown that the presence of tooth tips on the wounded teeth increases the slot pitch that increases the pitch factor and the winding factor. This increase in the winding factor increases average torque. The average torque increases first at a given flux gap and then decreases with an increase in tooth tip width; this occurs because the increase in tooth tip width first increases the pitch factor up to unity, which reduces after further increasing the width. Since the flux gaps can be used as water cooling ducts [30], this work is helpful as a reference to select the tooth width to achieve maximum torque for a given flux gap in cases where the thickness of the flux gaps is dependent on the water cooling ducts.

Tomida *et al.* proposed the use of oriented steel in the construction of segmented stators in interior permanent magnet synchronous machine [11]. It was shown that the use of oriented steel in the stator construction for the machine designed for non oriented steel results in an increase in flux density, for the same rotor, in the rotor under no-load conditions. The yoke width was reduced to increase the reluctance, and hence leading to less concentration of flux. The efficiency was further improved by choosing thin laminations.

Ma *et al.* proposed the use of oriented steel in the stator and rotor teeth of AFSRM [17]. In this work first three different candidates, with the difference in the placement of the stator

teeth on the stator yoke in the segmented stator, were analyzed. Out of these three designs, the design with the lowest processing complexity and lowest iron loss was selected. Then Rolling-direction optimization strategy (RDOS) was used to match the rolling direction and magnetic flux direction to enhance the machine's performance. It was shown that by using RDOS, the torque of the oriented steel segmented stator and rotor AFSRM improves by 20.5% compared to its non oriented steel counterpart.

1.3.6 Modelling of Segmented Stators in FEA

Segmented stator construction allows the freedom of using oriented steel in the segments to increase the permeability in one direction, either tooth or back iron, and reduce the core losses. Also, segmentation requires more punchings of the stator as compared to the whole conventional stator. Therefore, a finite element modeling method is required to consider the effects of extra cut edges in the segmented stators compared to whole conventional stators. Also, an accurate method to model anisotropic steel in the segmented stator is required. This section discusses the modeling techniques to consider extra cut edges and anisotropic steel developed in the literature so far.

1.3.6.1 Modelling for Extra Cut Edges in the Segmented Stators

Processing of steel laminations in the industry (cutting, punching, etc.) results in significant degradation of the material magnetic properties [31, 32]. It is shown in [33–38] that punching affects the micro-structure, internal stresses, and grain morphology of the steel near the edges that leading to a decrease in magnetic permeability and an increase in losses near the cut edge. Segmented stator construction adds more cut edges as compared to the conventional round stator construction. Therefore, correct modeling in FEA is essential in

order to achieve correct results.

Li *et al.* [14] modelled the segmented stator using the technique presented in [32,39]. The steel's BH curve and loss curves were carried out using an Epstein frame according to international standards IEC 60404-2 and IEC 60404-10. In these tests, magnetic measurements were carried out on strips of the same width with increasing sub-strips. These sub-strips were placed parallel to each other, and the number of cut-edges gradually increased with increasing sub strips. For a total width of the strip of 80 mm and N, the number of cut edges or twice the number of vertical cuts in the strip, N = 6, consists of 4 sub-strips of 20 mm in width, N = 14 consists of 8 sub-strips of 10 mm in width, and similarly, for other values of N. It should be noted that magnetic field density is distributed as a function of the distance from the cut edge. The value of magnetic field density (B) recorded at a time instant is the mean value of B averaged over the space. Tests were conducted for different numbers of sub-strips at different values of the peak value of average field density ($\hat{B}_{avg}$) and corresponding values of peak magnetic field intensity ($\hat{H}$). This provides different BH curves for different numbers of cut edges. Also, different frequencies and different peak values of average field density ($\hat{B}_{avg}$) were used to obtain the losses P (in W/kg). Further analysis was performed to define the magnetization and loss curves as a function of the distance from the cut-edge by using the fitting parameters of pre-described degradation curves [32]. Finally, zones away from the cut edge were defined, and average magnetization and loss curves were used for analysis. Fig. 1.11 shows these zones for non-segmented and segmented stators [14]. The FEA uses the BH curves and core loss information of the defined zones, and hence calculations are more accurate to the models in which no such zones are defined.

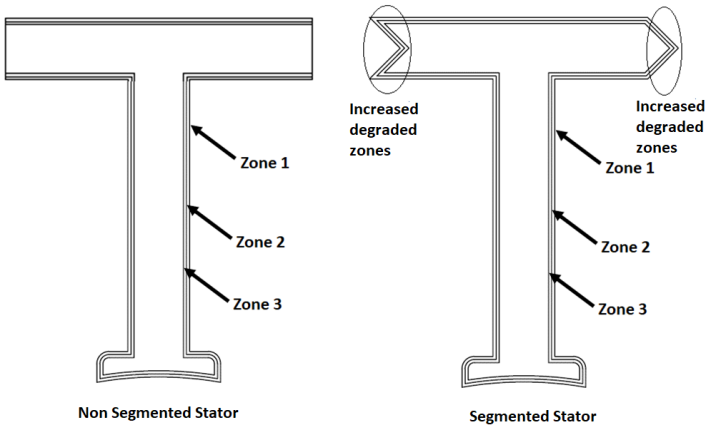

Figure 1.11: Zones Divided from the cut-edge for non-segmented and segmented stators.

1.3.6.2 Modelling for Anisotropic Steel in the Segmented Stators

The crystal structure in grain-oriented electrical steel (GOES or anisotropic steel) has crystal grains oriented in one direction, the rolling direction. Due to this internal morphology, the magnetic characteristics of GOES depend on the flux direction. Such behavior is different in non-GOES or isotropic steel, with almost the same characteristics regardless of the direction.

Furthermore, the variation of GOES magnetic characteristics with respect to flux direction has been proven to be neither linear nor follow an elliptical pattern. The magnetic permeability of any anisotropic material is the highest at the rolling direction 0°, a lower one is found at the transverse direction, i.e., 90° relative to the rolling direction, and the lowest one is obtained at around 50°–60° apart from the rolling direction [8]. Anisotropic steel follows a different BH and loss curve in every direction, unique for every steel, making it hard to model in finite element (FE) simulation. In the present-day FEA software, the magnetic properties, BH curves, and loss curves of the rolling and transverse directions are used to interpolate the magnetic properties in between the rolling and transverse directions. Moreover, the method of interpolation is not controlled by the user, which may lead to

inaccuracy in the results.

In [40] a method that can be used in FEA to analyze the performance of PMSM with GOES stator laminations accurately was developed. In this method, the stator is divided into sections and based on the direction of flux, the BH curves and loss curves are assigned to individual sections. Thus the simulation is reduced to a connected structure of isotropic materials. Because of the proposed model's structure, it is termed the piecewise isotropic model in the present work. The machine used for analysis in [40] is a 12 slot/ 14 pole PMSM consisting of six segments, where each segment is oriented in the direction of teeth. The direction of orientation of one segment is shown in Fig.1.12.

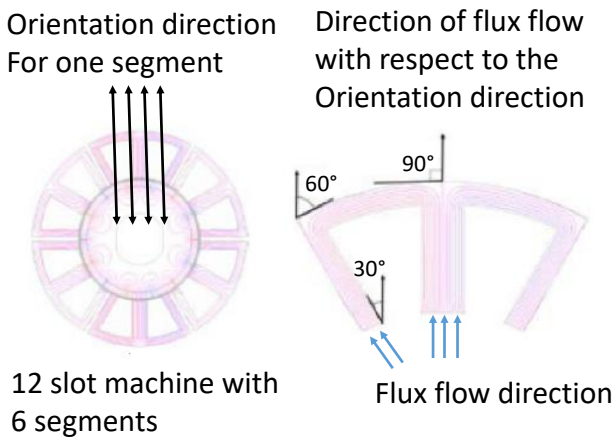

Figure 1.12: Direction of orientation, and flux direction in the whole machine and one segment under no load condition [40].

The flux direction in the whole machine and segments under no-load condition is shown in Fig.1.12. For one segment, the direction of flux for the middle tooth is in the direction of alignment, i.e., 0° away from the rolling direction, and for the adjacent two teeth, the flux direction is 30° away from the rolling direction. For the back iron between the middle and adjacent tooth, the flux changes the direction from 90° to 60° as it flows through the back iron. The proposed model in [40] is obtained by connecting the segments with the BH and loss curves of the 0° direction on the central tooth, the BH and loss curves of the 30°

direction on the lateral teeth, and the back iron is modeled using the BH and loss curves for the 75° direction which is the average value of the angles 60° and 90°. The model of one of the segments is given in Fig.1.13, and six segments connected along the circumferential is used to model the complete machine.

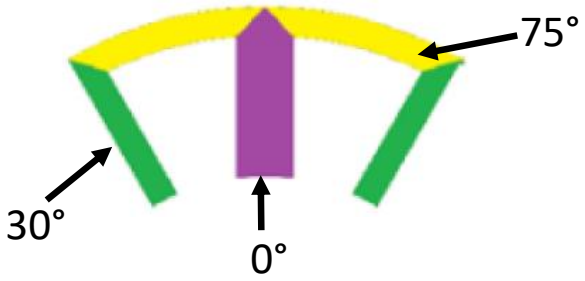

Figure 1.13: Piece-wise isotropic model used for analysis. Each color corresponds to the angle away from the rolling direction that uses the magnetic properties of the oriented steel for that angle [40].

The piecewise isotropic model, as shown in Fig.1.13, can be used for PMSM modeling accurately if the magnetic properties, BH, and loss curves, of the steel, are known at a certain angle away from the rolling direction.

1.4 Contribution of the Present Work to the State of Art

As discussed in section 1.3.6.2 the accurate modeling of the oriented steel segmented requires BH and loss curves in all the directions of orientations; the accuracy of the model proposed in [40], for the machine with the high number of teeth, is discussed in appendix A. Therefore, using the Epstein frame test is very expensive, and hence makes it impractical. The first contribution of this research is to propose and validate a method for the characterization of the oriented steel that is comparatively less expensive than the Epstein frame

test. Further, the impact of segmentation parameters, number of segments, and length of the parasitic gaps, on the machine's performance is not discussed for the distributed winding integral slot machine. The second contribution of this work proposes and validates a theory to determine the impact of the segmentation on the performance of the distributed winding integral slot machine. Finally, this work proposes the systematic steps for the comparative analysis of the oriented steel segmented stator PMSM with the conventional stator PMSM.

1.5 Proposed Research Methodology

In this section, the overview of the proposed research methodology is discussed. In section 1.3.6.2 the necessity of using the piecewise isotropic model for modeling of anisotropic steel stator for better accuracy was discussed. In order to use the piecewise isotropic model, there is a need for BH and loss curves in between the rolling and transverse axis direction for accurate modeling. The proposed method requires a specially designed experimental setup to estimate the magnetic characteristics of oriented steel. The oriented steel's estimated magnetic properties are used to model the oriented steel segmented stator based on the topology of segmentation and the direction of orientation. Circumferential segmentation in the direction of the slot is used for analysis, where all the segments are symmetrical, and each consists of integral values of teeth. Fig.1.14 shows an example of circumferential segmentation in the direction of the slot. N_s denotes the total number of segments in each machine. All the gaps are assumed uniform where the parasitic gap length is denoted by g_p.

The selected orientation direction of each segment is along the general direction of the teeth, i.e., the center tooth is at 0°. This orientation direction is selected because the flux density in the teeth is higher than in the back iron. Since oriented steel may improve the

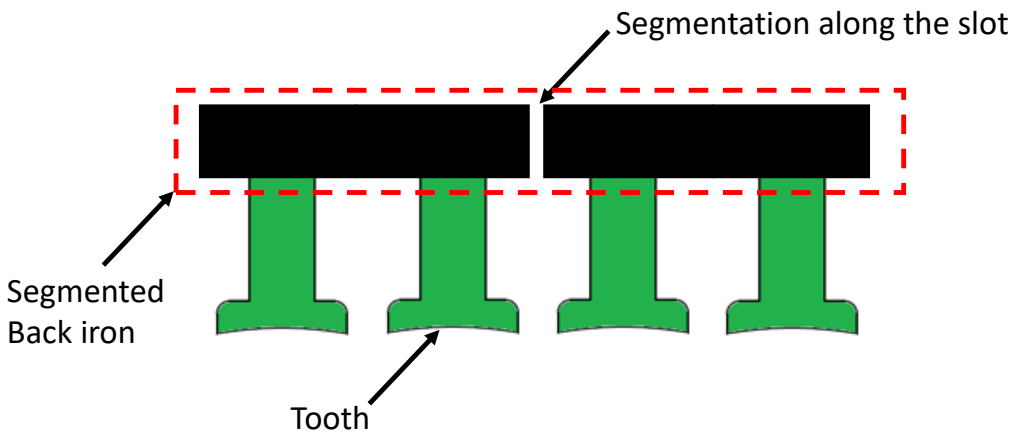

Figure 1.14: Circumferential segmentation in the direction of slot with each segment consisting of two teeth.

stator's overall core loss and permeability, the core loss and average torque are used for performance analysis. Moreover, the effect of segmentation on cogging torque was discussed in section 1.3.3. Hence, cogging torque is another performance measure. Finally, the unsymmetrical placement of the segmentation may lead to unbalanced back electromotive force (BEMF). Therefore, the BEMF is selected as the final design measure. A general theory is proposed to find the impact of segmentation parameters on each selected performance parameter. Finally, using the magnetic properties of oriented steel along with the proposed general theory, the performance of the oriented steel segmented stator PMSM predicted and compared with the conventional stator PMSM.

In summary the proposed method for the analysis of oriented steel segmented stator PMSM is:

1. Use the designed experimental setup to estimate BH and loss curves between the rolling and transverse direction.

2. Develop a general theory to determine the impact of segmentation parameters on the performance of the machine.

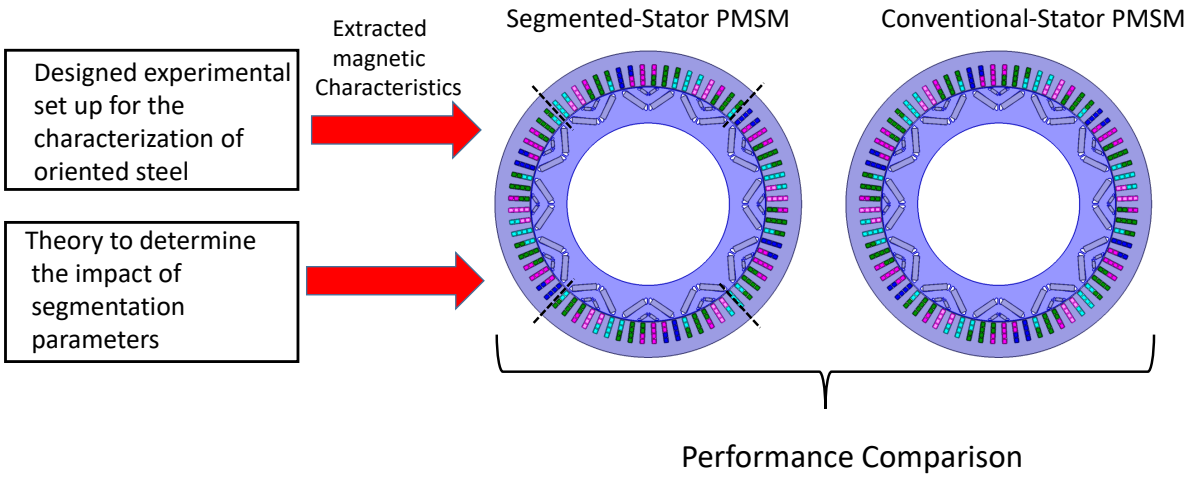

Figure 1.15: The process flow for the analysis of oriented steel modular PMSM using the proposed method.

3. Use, BH, and loss curves in the piecewise isotropic model for modeling oriented steel modular stator PMSM for comparison with a conventional machine.

The process flow of the proposed method is shown in Fig.1.15.

1.6 Organization

Chapter 2 discusses the method for the characterization of oriented steel. Chapter 3 and 4 discusses the impact of segmentation parameters on core loss/average torque, and cogging torque/BEMF respectively. Chapter 5 discusses the comparison of the performance of oriented steel segmented stator PMSM with the conventional stator PMSM. Finally, Chapter 6 concludes the thesis.

Chapter 2

Method for the Characterization of the Oriented Steel

In this chapter, a relatively less expensive method is proposed to estimate the properties of the oriented steel relative to the rolling and transverse directions that can be used to model oriented steel segmented stator PMSM discussed in section 1.3.6.2. The idea of the research methodology is to develop and use an experimental setup to inject the flux of desired magnitude and frequency in the portions of the oriented steel segmented stator. Based on the direction of the flux with respect to the rolling direction, the magnetic properties of the oriented steel are obtained. The proposed method can be applied to the stator of any initial design.

2.1 Proposed Method for the Extraction of Magnetic Properties of the Oriented Steel

The proposed method is applicable for modular stators consisting of circumferential segmentation. This study focuses on the machine where the orientation of each segment is in the direction of teeth, although the proposed method can be expanded to other orientation directions. The core idea of the proposed method is to calculate the core loss and MMF drop

at different levels of flux densities and frequencies of the teeth and the back iron segments of the segmented stator. Then these values are used to estimate the BH and Loss curves in between the rolling and transverse directions. A specially designed device, along with data post processing, is used to measure the core loss or MMF drop of a portion of the stator, which is the combination of the core loss of the teeth and back iron. Therefore, devices of different spans are used to calculate the core loss and MMF drop of each tooth and back iron segment. In this section, first, the use of oriented-steel segmented stator and devices is discussed, along with the basic idea of the proposed method. Then, the mathematical model is discussed to solve for the core loss and MMF drop in each tooth and back iron segment.

2.1.1 Basic Idea of the Proposed Method

Consider a machine consisting of oriented steel modular stator of N_t teeth. The adjacent teeth of this machine are located $360/N_t$ degrees apart, and the steel orientation of these two teeth is also $360/N_t$ degrees apart. For example: for a 12 slot machine, the two consecutive teeth are 30° apart, as shown in Fig.1.13. As the number of teeth increases, the change in their orientation decreases, so experimental data at more discrete orientations is needed to model the machine accurately; this implies that Epstein frame tests become more impractical as N_t increases. In the proposed method, the stator used for measuring magnetic properties should be the same as the final desired stator design, and the number of segments should be chosen to provide enough different orientation angles for the final analysis. An example shows this in Fig.2.1, where the magnetic properties of the teeth and back iron in one segment are shown for a machine consisting of 72 teeth and N_s number of segments. The machine with $N_s = 4$ can provide magnetic data for the oriented steel at more orientation angles than the machine with $N_s = 6$. The components with similar magnetic properties are colored the

same.

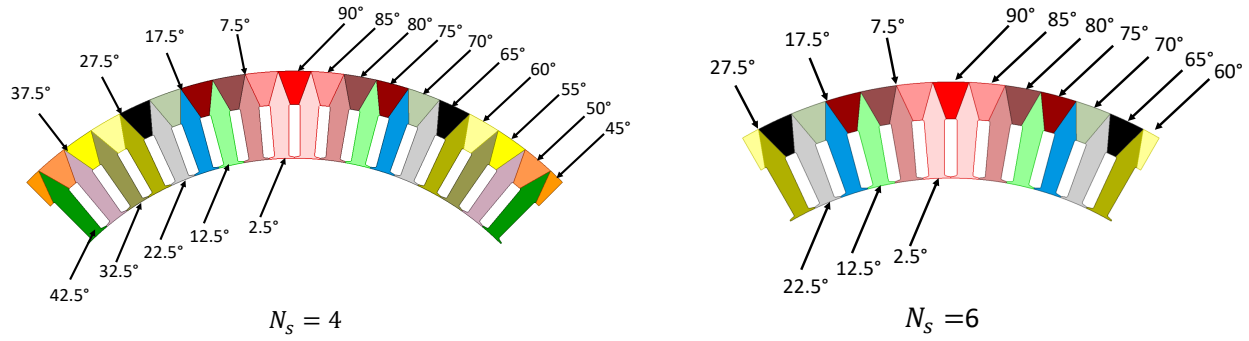

Figure 2.1: An example to show which teeth and back iron sections have similar magnetic properties for a 72-tooth machine with 4 and 6 segments [41].

A typical starting point to design the modular stator is the stator used in its non-modular counterpart [1]. In this work, the design of the geometry of the stator already used for testing is the initial design of the non-modular stator.

The second requirement of the proposed method is the specially designed device that imposes a time-dependent magnetic flux of controlled amplitude and frequency in the stator teeth and back iron. In this work, these device is termed sensor. These devices consist of an H-shaped core of high-quality magnetic steel laminations and two coils: a drive coil to impose a current and a resulting magnetomotive force (MMF) to the circuit and a pickup coil to measure the induced voltage. The voltage and currents are post-processed to find the MMF drop and core losses. Therefore, in this work, it is safe to say that the sensor is used to measure the core loss and MMF drop of the portion of the segment in which it is used to impose the flux of desired magnitude and frequency. Fig.2.2 shows the experimental setup consisting of oriented steel stator and sensor, indicating the drive coil or primary coil and pickup coil or secondary coil.

The flux injected by the sensor emulates the direction of flux in the stator teeth and back

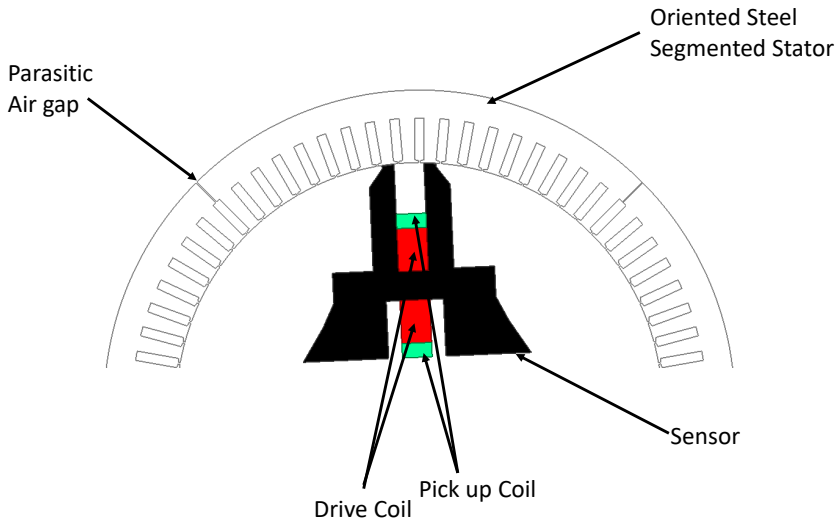

Figure 2.2: Experimental set up consisting of oriented steel segments, sensor, drive coil and pickup coil [41].

iron similar to that of machine operation. The applied flux passes through the teeth, follows the path from the back iron spanned by the sensor, and returns through the second tooth opposite the second sensor limb. The teeth directly in line with the sensor limbs provide the properties of the oriented steel in the orientation of said teeth. The same is true for the portion of the back iron in between the adjacent teeth. A third component is the teeth between the sensor limbs, but this is not used for analysis due to the nonuniformity of the flux. The flux lines in the segment injected by the sensor that spans over one tooth with the orientation angle are shown in Fig.2.3. The relative placement of the teeth for this example is 5°.

The flux is not uniform in yellow teeth, and the tendency of the flux to flow through the teeth increases as the segment gets more and more aligned in the direction of teeth as shown in Fig. 2.4.

The flux in the pink and green teeth emulates the flux of the machine teeth under operation. Similarly, the red and orange components of the back iron emulate the flux of the

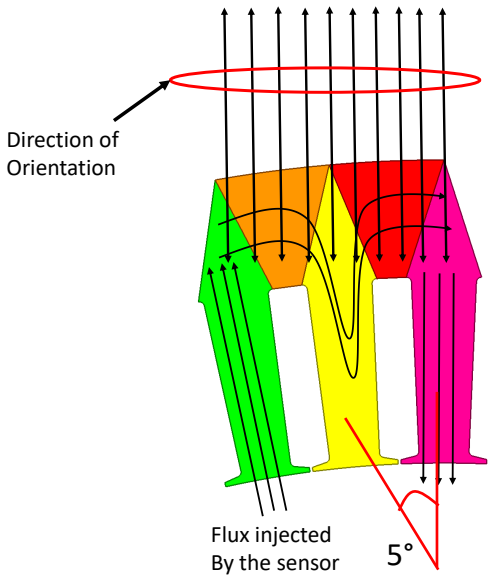

Figure 2.3: Conceptual drawing of the flux lines in the portion of the segment injected by the sensor spanning over one tooth [41].

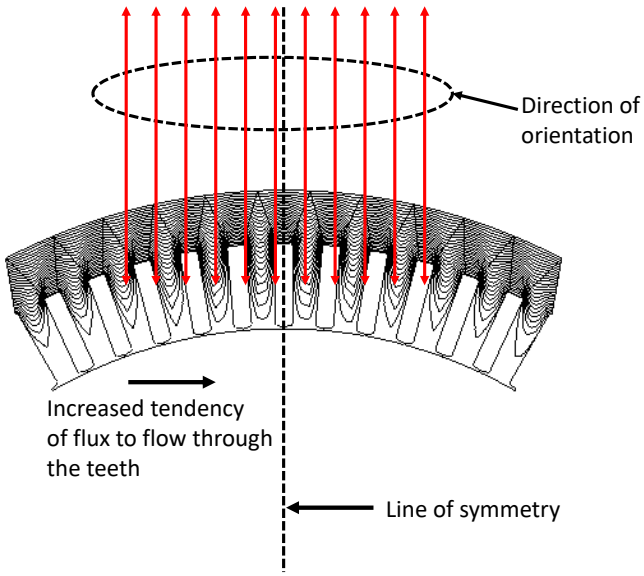

Figure 2.4: Flux, computed by JMAG FEA software, in the stator back iron to show the tendency of the flux to flow through the teeth.

machine back under operation. As discussed in section 1.3.6.2 the pink teeth, green teeth, red back iron, and orange back iron represent the measurements in the experiments to the magnetic properties of 0°, 10°, 87.5° and 82.5° away from the rolling direction. However, due

to the nonuniformity of the flux in the yellow portion, the magnetic properties in those teeth cannot be determined with confidence. Therefore, in this work, the magnetic properties of these components are not used to estimate the magnetic properties of the oriented steel. The variables, core losses or MMF drop, measured by the sensors are denoted by "Y". Therefore, the core losses or MMF drop in the stator portions involved in this experiment measured by the Sensor from Fig.2.3 is:

$$Y_{StatorPortion} = Y_{\text{Pink Teeth}} + Y_{\text{Green Teeth}} + Y_{\text{Red Back Iron}} + Y_{\text{Orange Back Iron}} + Y_{\text{Yellow Portion}} \tag{2.1}$$

In this work, the back iron, teeth with uniform flux, and teeth with non-uniform flux are denoted by X, T, and $\hat{T}$ respectively. Therefore, (2.1) reduces to:

$$Y_{StatorPortion} = Y_{T_{0^\circ}} + Y_{T_{10^\circ}} + Y_{X_{87.5^\circ}} + Y_{X_{82.5^\circ}} + Y_{\hat{T}_{5^\circ}} \tag{2.2}$$

where the angles in the suffix show the magnetic properties X or T. Notice that for $\hat{T}$ the suffix is denoted by 5° just to indicate the location of $\hat{T}$ with respect to the orientation direction. The sensors are used to measure the core losses and MMF drop at different values of flux densities and frequencies at different positions in the stator. For each value of flux density, frequency, core loss values, and MMF drop for each X and T are calculated and then used to estimate the core loss and BH curves.

In order to calculate the core loss or MMF drop of X and T, sensors of different spans are used. A set of linear equations relates the measured values of core losses and MMF drop at different positions, from different sensors, within the oriented steel stator. These equations

are solved, and the values of MMF drop or core losses of individual teeth and back iron are obtained. The number and span of sensors required to achieve this depends on the number of segments and teeth in the oriented steel stator used for testing. An example illustrates the selection of span and number of the sensor.

Suppose a segment consists of an even number of teeth, denoted by "n". Each segment of the stator is symmetric along the axis that divides the segment into two identical parts. Fig.2.5 shows the line of symmetry, and all the components are colored the same to represent identical magnetic properties.

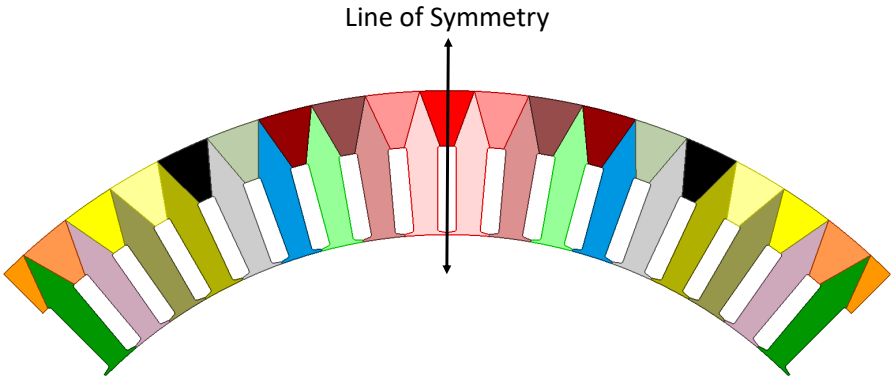

Figure 2.5: An example to show the line of symmetry which divides the segment into two identical halves [41].

This means there are n/2 different T and $\hat{T}$, and n/2+1 different X that may show different values of core losses or MMF drop for the exact value of flux density and frequency; this results in 3n/2+1 variables to be solved with different spans and numbers of sensors. The sensor spanning over an odd number of teeth provides n/2 unique equations, while the sensor spanning over an even number of teeth provides n/2+1 unique equations. These equations are obtained when the experiments measure the core losses or MMF drop in the stator at different positions. These equations, when combined, may not yield a total of 3n/2+1 unique equations. However, it can be shown that by using simple assumptions, these equations can

be solved. This implies that a combination of two sensors spanning an odd number of teeth and one sensor spanning an even number of teeth can be used to obtain the values of all the components. For the sake of simplicity, the measured core losses or MMF drop, which is the linear combinations of the three components, are arranged in the form of the matrices:

$$\underset{\frac{n}{2}\times 1}{\mathrm{Y}_{\mathrm{oddsen1}}} = \underset{\frac{n}{2}\times\frac{3n+2}{2}}{A_{oddsen1}} \times \underset{\frac{3n+2}{2}\times 1}{K} \tag{2.3}$$

$$\underset{\frac{n}{2}\times 1}{\mathrm{Y}_{\mathrm{oddsen2}}} = \underset{\frac{n}{2}\times\frac{3n+2}{2}}{A_{oddsen2}} \times \underset{\frac{3n+2}{2}\times 1}{K} \tag{2.4}$$

$$\underset{\frac{n+2}{2}\times 1}{\mathrm{Y}_{\mathrm{evensen}}} = \underset{\frac{n+2}{2}\times\frac{3n+2}{2}}{A_{evensen}} \times \underset{\frac{3n+2}{2}\times 1}{K} \tag{2.5}$$

where vector Y consists of the measured values at different sensor positions, matrix A accounts for the number of times each discrete steel orientation angle appears in the sensor span, and vector K represents the core losses or MMF drop of all three components. The matrices are obtained for each combination of the flux density and frequency and solved to obtain each component's core loss and MMF drop at the given flux density and frequency level. The same discussion can be extended to measurements with a sensor spanning an odd number of teeth. The application of the proposed method is discussed in the next section that explains all the matrices in equations 2.3, 2.4 and 2.5.

2.1.2 Application of the Proposed Method

The stator used for testing has 72 teeth, and the selected number of segments is four. Four segments are selected to extract data at all angles away from the rolling direction in

steps of 5° as shown in Fig.2.1. Therefore, the information extracted from the four segments can still be used to model the machine consisting of 2 or 3 segments.

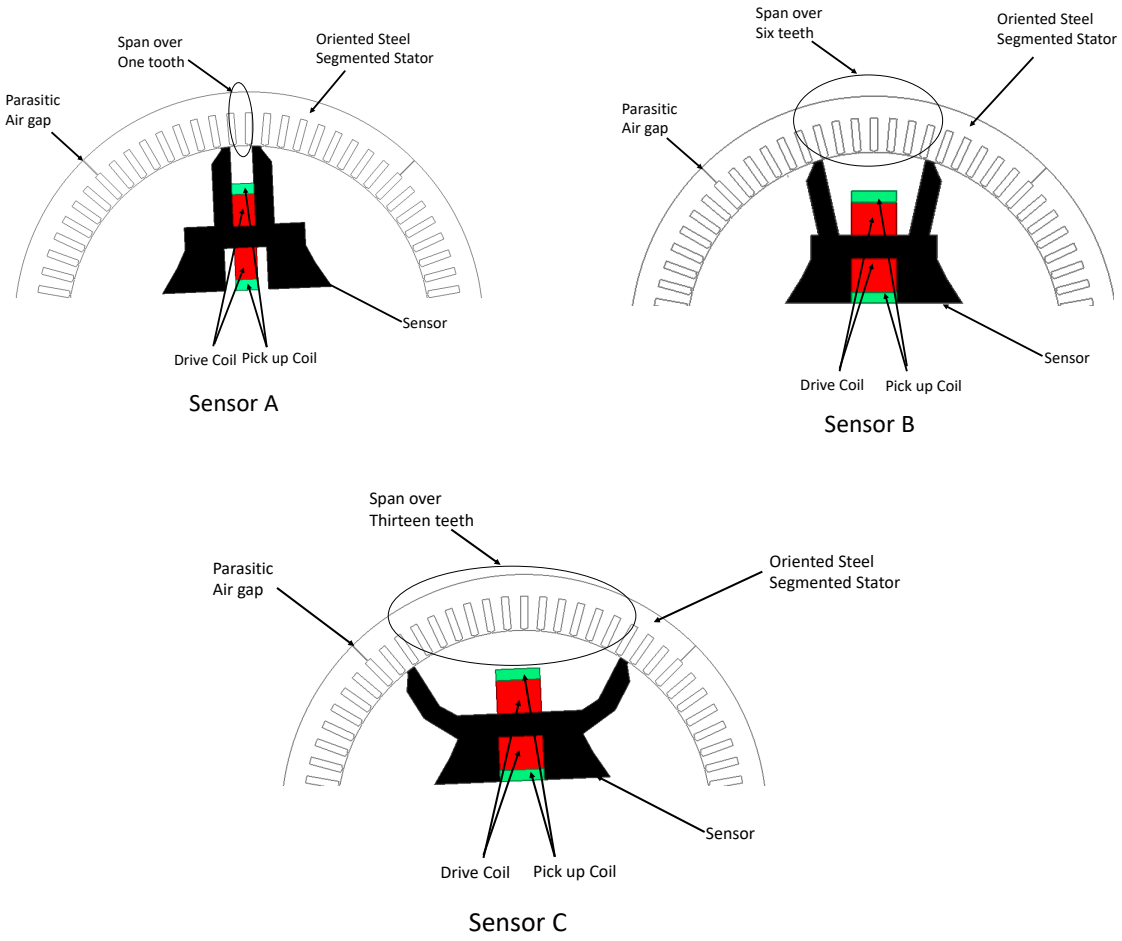

Figure 2.6: The designed sensors with three different spans.

The three designed sensors, as shown in Fig.2.6, are named Sensor A, B and C. The spans for three different sensors are:

1. Sensor spans one tooth in stator (Sensor A)

2. Sensor spans six teeth in stator (Sensor B)

3. Sensor spans thirteen teeth in stator (Sensor C)

where A and C are odd span sensors, and B is even span sensor. The back iron division

is shown in Fig.2.7 with respect to the line of symmetry. The pairs of X_i, $\forall\ i \in [2, 10]$, are aligned identically with respect to the rolling direction, and hence they have similar magnetic properties. Moreover, X_1 represents the properties of 90° away from the rolling direction, X_2 represents properties of 85° away from the rolling direction and so on.

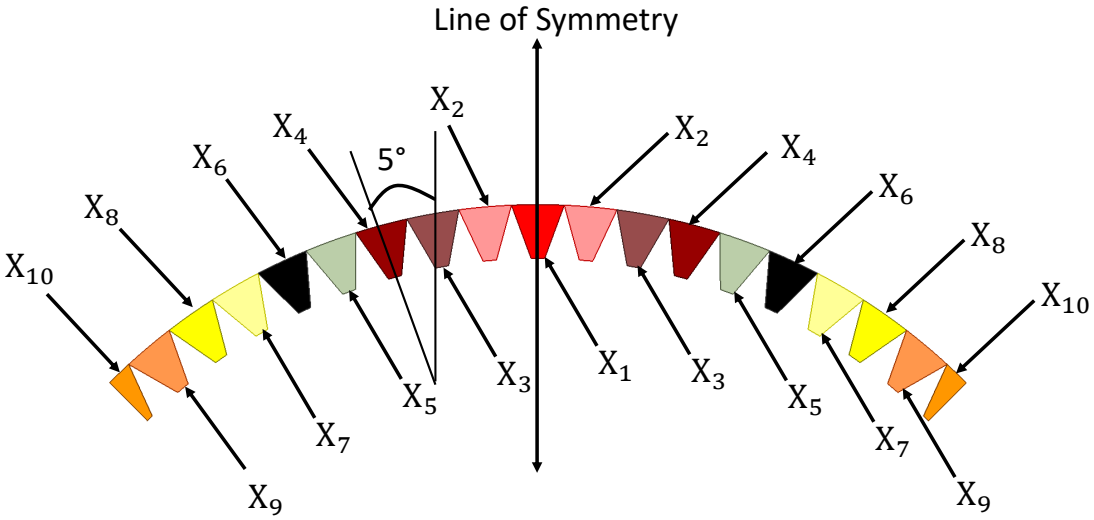

Figure 2.7: Symmetry for the backiron sections of one segment for a 72-tooth machine consisting of four segments [41].

The placement of teeth with respect to the line of symmetry is shown in Fig.2.8. The pairs of T_j, $\forall\ j \in [1, 9]$, have identical magnetic properties due to symmetry. Moreover, T_1 represents the property of 2.5° away from the rolling direction, T_2 represents properties 7.5° away from the rolling direction, and so on. Similarly, symmetry holds for $\hat{T}_j$ as well.

The lower values of i and j correspond to the positions of X_i, T_j or $\hat{T}_j$ closer to the symmetrical axis as shown in Figs. 2.7 and 2.8. Starting from 1, for every 5° shift, the value of i increases by 1. Each sensor is used to measure the core losses and MMF drop of different pieces of the segmented stator at different positions in the stator. The following nomenclature is developed to denote the position of the sensor:

1. The symmetric placement of sensor is denoted by "Sensor name$_1$". For example, for

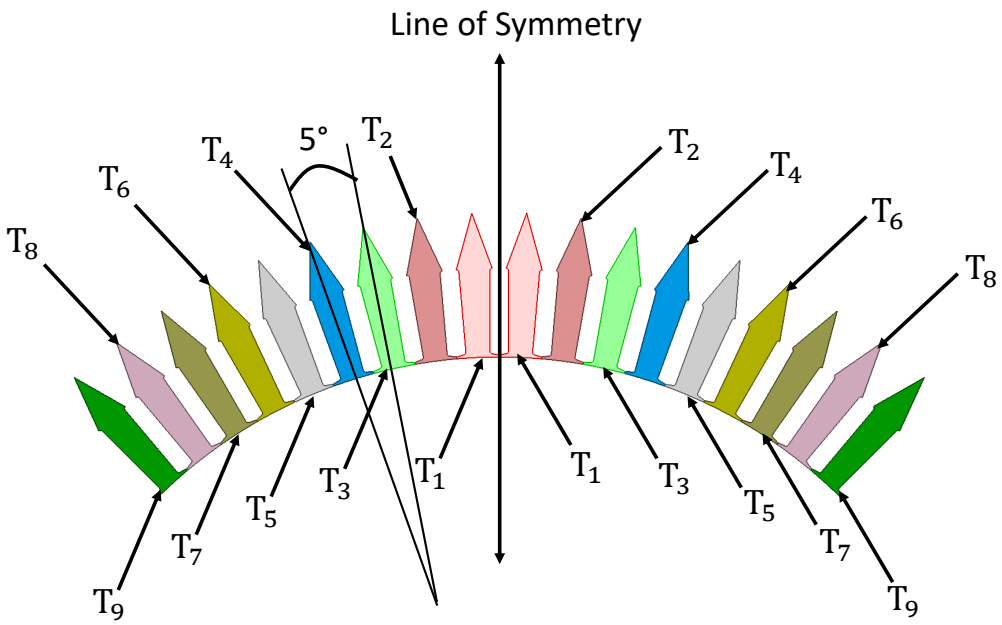

Figure 2.8: The division one segment to show the relative placement of teeth for the machine consisting of 72 teeth and four segments based on symmetry [41].

sensors A, B and C the symmetric placement of sensors with respect to the symmetrical line are denoted by A_1, B_1 and C_1, respectively.

2. The second position of the sensor is its 5° anti-clockwise shift from its position 1. For sensors A, B and C these positions are denoted by A_2, B_2 and C_2 respectively.

3. Similarly, the third position of the sensor is its 10° anti-clockwise shift from its position 1.

Positions A_1 and A_2 in Fig.2.9 show how the position of the sensor with respect to the stator is denoted in this method.

The core losses or MMF drop measured using the sensors are denoted by "Y". Therefore, the core losses or MMF drop measured using Sensor A in symmetrical position are denoted by Y_{A_1}. Similarly, the core losses or MMF drop of element X_1 are denoted by Y_{X_1} and so on. The loss measured by sensor A in position A_1 as shown in Fig.2.9 is written as the sum

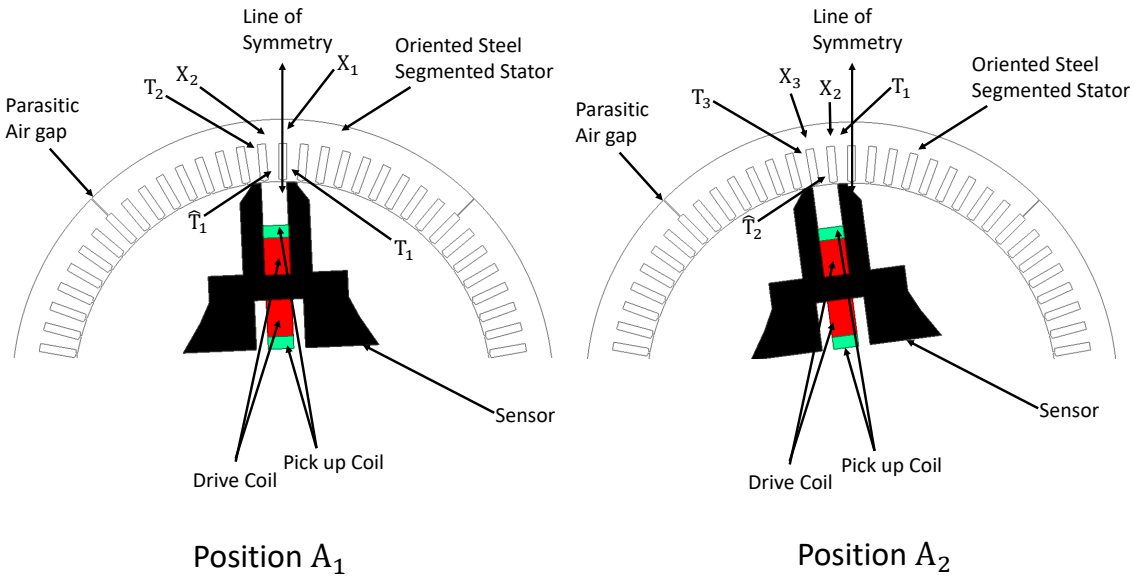

Figure 2.9: Positioning of Sensor A in positions A_1 and A_2 [41].

of five components:

$$Y_{A_1} = Y_{X_1} + Y_{X_2} + Y_{\hat{T_1}} + Y_{T_1} + Y_{T_2} \tag{2.6}$$

This method divides the core losses or MMF drop in one portion of the segmented stator into the five components, as shown in (2.6). Using these equations, the core losses and MMF drop for all values of X_i, T_i, and $\hat{T}_i$ are determined at each level of flux density and frequency. In this example number of teeth in each segment is 18, which is denoted by "n" in equations 2.3, 2.4 and 2.5. Therefore, the matrices dimensions for sensor A(odd span), B(even span) and C(odd span) are:

$$\underset{9\times1}{\mathrm{Y_A}} = \underset{9\times28}{A_A} \times \underset{28\times1}{K} \tag{2.7}$$

$$\underset{10\times1}{\mathrm{Y_B}} = \underset{10\times28}{A_B} \times \underset{28\times1}{K} \tag{2.8}$$

$$\underset{9\times1}{\mathrm{Y_C}} = \underset{9\times28}{A_C} \times \underset{28\times1}{K} \tag{2.9}$$

All possible 28 equations given in (2.7), (2.8) and (2.9) along with the K vector is:

$$\begin{bmatrix} Y_{A_1} \\ Y_{A_2} \\ Y_{A_3} \\ Y_{A_4} \\ Y_{A_5} \\ Y_{A_6} \\ Y_{A_7} \\ Y_{A_8} \\ Y_{A_9} \end{bmatrix} = \begin{bmatrix} 1&1&0&0&0&0&0&0&0&0&1&1&0&0&0&0&0&0&0&1&0&0&0&0&0&0&0&0 \\ 0&1&1&0&0&0&0&0&0&0&1&0&1&0&0&0&0&0&0&0&1&0&0&0&0&0&0&0 \\ 0&0&1&1&0&0&0&0&0&0&0&1&0&1&0&0&0&0&0&0&0&1&0&0&0&0&0&0 \\ 0&0&0&1&1&0&0&0&0&0&0&0&1&0&1&0&0&0&0&0&0&0&1&0&0&0&0&0 \\ 0&0&0&0&1&1&0&0&0&0&0&0&0&1&0&1&0&0&0&0&0&0&0&1&0&0&0&0 \\ 0&0&0&0&0&1&1&0&0&0&0&0&0&0&1&0&1&0&0&0&0&0&0&0&1&0&0&0 \\ 0&0&0&0&0&0&1&1&0&0&0&0&0&0&0&1&0&1&0&0&0&0&0&0&0&1&0&0 \\ 0&0&0&0&0&0&0&1&1&0&0&0&0&0&0&0&1&0&1&0&0&0&0&0&0&0&1&0 \\ 0&0&0&0&0&0&0&0&1&1&0&0&0&0&0&0&0&1&1&0&0&0&0&0&0&0&0&1 \end{bmatrix} \cdot K \tag{2.10}$$

where K is a column vector:

$$K^T = [Y_{X_1}\, Y_{X_2}\, Y_{X_3}\, Y_{X_4}\, Y_{X_5}\, Y_{X_6}\, Y_{X_7}\, Y_{X_8}\, Y_{X_9}\, Y_{X_{10}}\, Y_{T_1}\, Y_{T_2}\, Y_{T_3}\, Y_{T_4}\, Y_{T_5}\, Y_{T_6}\, Y_{T_7}\, Y_{T_8}\, Y_{T_9}\, Y_{\hat{T_1}}\, Y_{\hat{T_2}}\, Y_{\hat{T_3}}\, Y_{\hat{T_4}}\, Y_{\hat{T_5}}\, Y_{\hat{T_6}}\, Y_{\hat{T_7}}\, Y_{\hat{T_8}}\, Y_{\hat{T_9}}]$$

$$\begin{bmatrix} Y_{B_1} \\ Y_{B_2} \\ Y_{B_3} \\ Y_{B_4} \\ Y_{B_5} \\ Y_{B_6} \\ Y_{B_7} \\ Y_{B_8} \\ Y_{B_9} \\ Y_{B_{10}} \end{bmatrix} = \begin{bmatrix} 1 & 2 & 2 & 2 & 0 & 0 & 0 & 0 & 0 & 0 & 0 & 0 & 0 & 2 & 0 & 0 & 0 & 0 & 0 & 2 & 2 & 2 & 0 & 0 & 0 & 0 & 0 & 0 \\ 1 & 2 & 2 & 1 & 1 & 0 & 0 & 0 & 0 & 0 & 0 & 0 & 1 & 0 & 1 & 0 & 0 & 0 & 0 & 2 & 2 & 1 & 1 & 0 & 0 & 0 & 0 & 0 \\ 1 & 2 & 1 & 1 & 1 & 1 & 0 & 0 & 0 & 0 & 0 & 1 & 0 & 0 & 0 & 1 & 0 & 0 & 0 & 2 & 1 & 1 & 1 & 1 & 0 & 0 & 0 & 0 \\ 1 & 1 & 1 & 1 & 1 & 1 & 1 & 0 & 0 & 0 & 1 & 0 & 0 & 0 & 0 & 0 & 1 & 0 & 0 & 1 & 1 & 1 & 1 & 1 & 1 & 0 & 0 & 0 \\ 0 & 1 & 1 & 1 & 1 & 1 & 1 & 1 & 0 & 0 & 1 & 0 & 0 & 0 & 0 & 0 & 0 & 1 & 0 & 0 & 1 & 1 & 1 & 1 & 1 & 1 & 0 & 0 \\ 0 & 0 & 1 & 1 & 1 & 1 & 1 & 1 & 1 & 0 & 0 & 1 & 0 & 0 & 0 & 0 & 0 & 0 & 1 & 0 & 0 & 1 & 1 & 1 & 1 & 1 & 1 & 0 \\ 0 & 0 & 0 & 1 & 1 & 1 & 1 & 1 & 1 & 1 & 0 & 0 & 1 & 0 & 0 & 0 & 0 & 0 & 1 & 0 & 0 & 0 & 1 & 1 & 1 & 1 & 1 & 1 \\ 0 & 0 & 0 & 0 & 1 & 1 & 1 & 1 & 1 & 2 & 0 & 0 & 0 & 1 & 0 & 0 & 0 & 1 & 0 & 0 & 0 & 0 & 0 & 1 & 1 & 1 & 1 & 2 \\ 0 & 0 & 0 & 0 & 0 & 1 & 1 & 1 & 2 & 2 & 0 & 0 & 0 & 0 & 1 & 0 & 1 & 0 & 0 & 0 & 0 & 0 & 0 & 0 & 1 & 1 & 2 & 2 \\ 0 & 0 & 0 & 0 & 0 & 0 & 1 & 1 & 2 & 2 & 0 & 0 & 0 & 0 & 0 & 2 & 0 & 0 & 0 & 0 & 0 & 0 & 0 & 0 & 0 & 2 & 2 & 2 \end{bmatrix} \cdot K \tag{2.11}$$

$$\begin{bmatrix} Y_{C_1} \\ Y_{C_2} \\ Y_{C_3} \\ Y_{C_4} \\ Y_{C_5} \\ Y_{C_6} \\ Y_{C_7} \\ Y_{C_8} \\ Y_{C_9} \end{bmatrix} = \begin{bmatrix} 1 & 2 & 2 & 2 & 2 & 2 & 2 & 1 & 0 & 0 & 0 & 0 & 0 & 0 & 0 & 0 & 1 & 1 & 0 & 2 & 2 & 2 & 2 & 2 & 2 & 1 & 0 & 0 \\ 1 & 2 & 2 & 2 & 2 & 2 & 1 & 1 & 1 & 0 & 0 & 0 & 0 & 0 & 0 & 1 & 0 & 0 & 1 & 2 & 2 & 2 & 2 & 2 & 1 & 1 & 1 & 0 \\ 1 & 2 & 2 & 2 & 2 & 1 & 1 & 1 & 1 & 1 & 0 & 0 & 0 & 0 & 1 & 0 & 0 & 0 & 1 & 2 & 2 & 2 & 2 & 1 & 1 & 1 & 1 & 1 \\ 1 & 2 & 2 & 2 & 1 & 1 & 1 & 1 & 2 & 1 & 0 & 0 & 0 & 1 & 0 & 0 & 0 & 1 & 0 & 2 & 2 & 2 & 1 & 1 & 1 & 1 & 1 & 2 \\ 1 & 2 & 2 & 1 & 1 & 1 & 1 & 2 & 2 & 1 & 0 & 0 & 1 & 0 & 0 & 0 & 1 & 0 & 0 & 2 & 2 & 1 & 1 & 1 & 1 & 1 & 2 & 2 \\ 1 & 2 & 1 & 1 & 1 & 1 & 2 & 2 & 2 & 1 & 0 & 1 & 0 & 0 & 0 & 1 & 0 & 0 & 0 & 2 & 1 & 1 & 1 & 1 & 1 & 2 & 2 & 2 \\ 1 & 1 & 1 & 1 & 1 & 2 & 2 & 2 & 2 & 1 & 1 & 0 & 0 & 0 & 1 & 0 & 0 & 0 & 0 & 1 & 1 & 1 & 1 & 1 & 2 & 2 & 2 & 2 \\ 0 & 1 & 1 & 1 & 2 & 2 & 2 & 2 & 2 & 1 & 1 & 0 & 0 & 1 & 0 & 0 & 0 & 0 & 0 & 0 & 1 & 1 & 1 & 2 & 2 & 2 & 2 & 2 \\ 0 & 0 & 1 & 2 & 2 & 2 & 2 & 2 & 2 & 1 & 0 & 1 & 1 & 0 & 0 & 0 & 0 & 0 & 0 & 0 & 0 & 1 & 2 & 2 & 2 & 2 & 2 & 2 \end{bmatrix} \cdot K \tag{2.12}$$

All the equations given in 2.10, 2.11 and 2.12 are used to calculate the values of Y_{X_i} and Y_{T_i}. The equations 2.10, 2.11 and 2.12 is a set of 28 equations, and 28 variables. However, there is an additional inevitable variable that is present in the system, which is not considered in the above set of equations. This variable is the impact of parasitic gaps present at the connections of the segments that may have an impact on the accuracy of the calculated values of Y_{A_i} and Y_{T_i}. The solution of the equations 2.10, 2.11 and 2.12 is discussed in

appendix B.

2.2 Sensor Design Considerations and Characterization

Sensors were designed for the method proposed in section 2.1. The key points of sensor design and application in experiments are summarized in section 2.2.1. The experiment measures the total MMF drop or core loss of the of the portion of the segment and sensor; therefore, the magnetic characteristics of the sensor must be subtracted to calculate the magnetic characteristics of the portion of the stator segment. The details of the sensor characterization are discussed in section 2.2.2.

2.2.1 Sensor Design Considerations

In this section, based on the proposed method, numerical simulations results, and experimental setup constraints, the following steps were performed for the design of the sensors:

2.2.1.1 Selecting the Total Number and Span of Each Sensor

The number and span of the sensors were obtained by performing FEA simulations and using the conditions discussed in section 2.1, to obtain the maximum possible accuracy of the proposed method.

2.2.1.2 Selecting Same Limb for All Sensors

All three sensors are designed with identical limbs. This ensures that the flux injected by all three sensors in the stator tooth is the same for the same value of flux in the sensor

limb. This flux can be controlled by controlling the voltage of the coil wound on the sensor limb. Fig.2.10 shows the limb pickup coil.

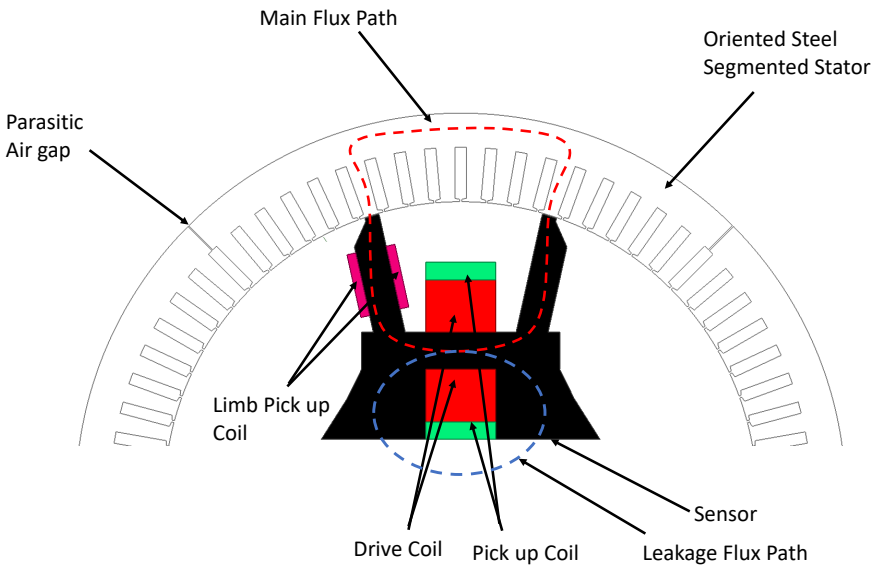

Figure 2.10: Sensor B consisting of Drive, Pickup and Limb pickup coils.

The reason to choose limb pickup coil voltage as a reliable measure to find the flux injected in the stator is the additional leakage path that passes through the pickup coil. The main flux path, shown in red, and leakage path, shown in blue, is shown in Fig.2.10. The leakage depends on the sensor design so that it may be different for all designed sensors. Therefore, the same flux injection for all sensors can be assured using the limb pickup coil.

2.2.1.3 Selecting the Air Gap Between the Limb of the Sensor and the Stator Tooth, and Number of Turns in Drive, Pickup and Limb Pickup Coil

Considering both the voltage and current limitations of the power amplifier the parameters shown in Table. 2.1 were selected for the experiments:

Parameter	Value
Number of turns in Drive Coil	50
Number of turns in Pickup Coil	50
Number of turns in Limb Pickup Coil	20
Air gap between the sensor limb and stator tooth	0.25 mm

Table 2.1: Parameters selected for experiments

2.2.1.4 Minimizing the Losses in the Sensor Laminations

The losses in the sensor should be kept as low as possible so that the power amplifier supplies lower power during the test to avoid overheating. Therefore, the sensors were made from high-quality steel laminations that offer lower losses.

2.2.1.5 Sensor Arrangement for Testing

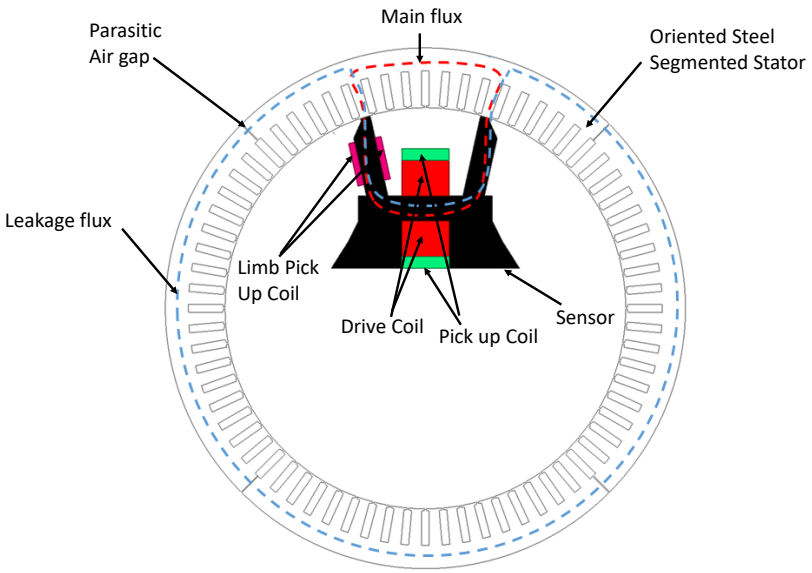

Figure 2.11: Flux distribution in one sensor arrangement.

The sensor is designed to calculate the MMF drop and core loss of the two teeth directly

opposite to the sensor limbs and the back iron spanned by the sensor. However, when only one sensor is used, the flux passes through the teeth and then splits into two paths. The first path closes through the teeth, and the back iron is spanned by the sensor, which is the main flux path. The second path closes through the teeth and the back iron that is not spanned by the sensor, which is the leakage path. The flux distribution of one sensor arrangement is shown in Fig.2.11.

The leakage in flux leads to considerable error in core loss calculation. The problem is resolved by using the symmetry of the two sensor arrangement. This arrangement creates an exactly similar reluctance path opposite to the position of the sensor. Therefore, the flux leakage through the back iron is avoided. Fig.2.12 shows the flux distribution in two sensor arrangement.

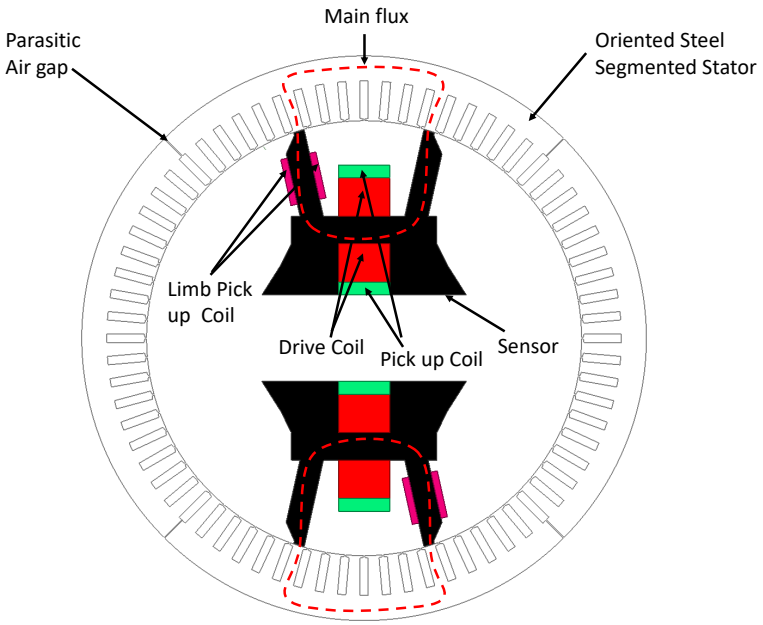

Figure 2.12: Flux distribution in two sensor arrangement.

2.2.2 Characterization of Sensors

2.2.2.1 Design of Characterization Set up

For characterization, the two sensors of the same design were placed head-on, and the drive coils of both sensors were supplied with the same current so that the flux distribution in both sensors was identical. Therefore, the losses in the sensors can be estimated as:

$$\text{Core Loss in the sensor} = \frac{\text{Total Loss in the Characterization set up}}{2} \tag{2.13}$$

There are two air gaps in the experimental setup corresponding to each limb. To obtain the net MMF drop in the sensor and two air gaps, the characterization setup must include the MMF drop of four air gaps and two sensors so that the MMF drop of the sensor and two air gaps is:

$$\text{MMF drop in one sensor} + \text{MMF drop in the two air gaps} = \frac{\text{Total MMF drop in the Characterization set up}}{2} \tag{2.14}$$

Small steel pieces were designed and placed in-between space of the limb of two sensors, due to their geometry, is avoided as shown in Fig. 2.13.

The geometry of the steel pieces was designed such that the flux distribution in the sensor is similar to flux distribution in the experimental setup. The steel pieces were designed such that:

1. The curvature of the steel piece is similar to the curvature of the stator.

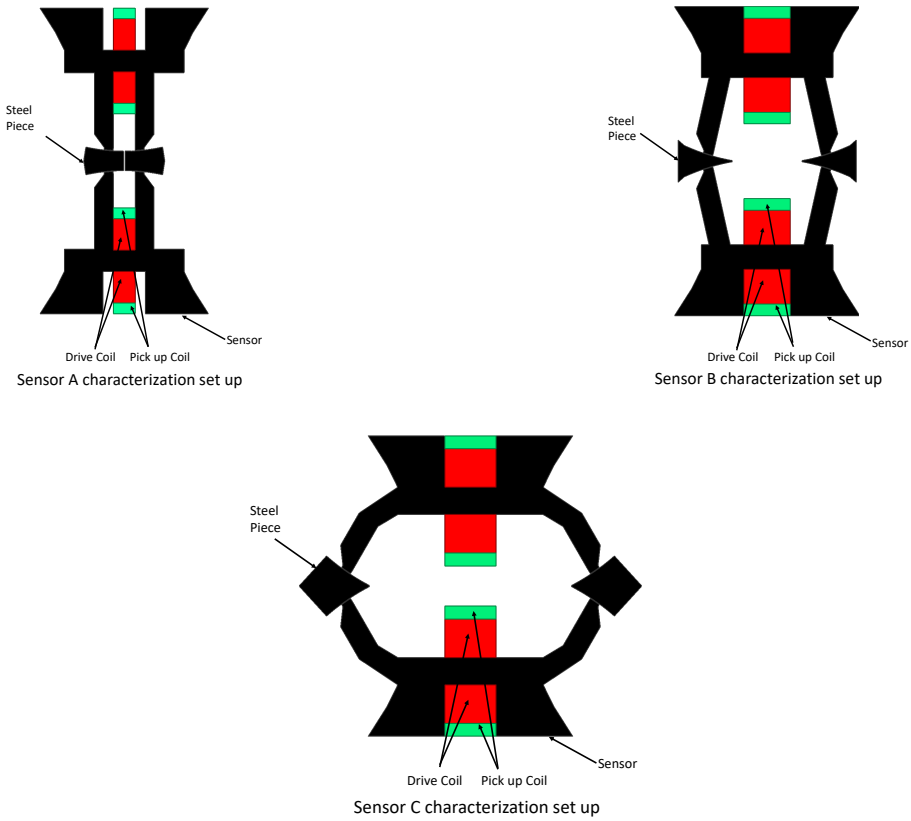

Figure 2.13: Sensor characterization arrangement with small steel pieces for all sensors.

2. The air gap between all sensor limbs and the steel pieces is equal to the air gap between the sensor and stator tooth.

Incorporating the core losses and the MMF drop in the steel piece, the equations 2.13 and 2.14 are modified as:

$$\text{Core Loss in the sensor} + \text{Core loss in the steel piece} = \frac{\text{Total Loss in the Characterization set up}}{2} \quad (2.15)$$

$$\text{MMF drop in one sensor} + \text{MMF drop in the two air gaps+}$$
$$\text{MMF drop in the steel piece} = \frac{\text{Total MMF drop in the Characterization set up}}{2} \quad (2.16)$$

2.2.2.2 Error in the Estimation of Core Losses and MMF Drop of the Sensors from Characterization Results

The error due to the presence of steel piece in the estimation of core losses and MMF drop, as given in equations 2.15 and 2.16, is decreased by designing the area for the flow of flux in the steel piece large enough such that flux density is small.

Sensor	Sensor core loss (in W)	Steel piece loss (in W)	% error
A	3.64	0.14	3.84
B	4.02	0.18	4.47
C	4.74	0.22	4.64

Table 2.2: Numerical Simulation Results for the Core losses of sensor and steel piece at 1.5 T flux density in the sensor limb and supply frequency of 50 Hz

The loss in the steel piece is less than 5% compared to the sensor, ensuring the accuracy in the estimation of sensor losses is not affected significantly after using sensor-steel piece arrangement for characterization. The core losses comparison of the sensor and steel piece for all three sensors is shown in Table.2.2.

For the same value of current in the drive coil, which is the same applied MMF, the flux distribution in the sensor limb is compared in three different conditions through simulations. The three different conditions are:

1. Experimental setup (Sensor-Stator arrangement).

2. Sensor-steel piece arrangement with steel piece permeability similar to steel used to build the sensor.

3. Sensor-steel piece arrangement with steel piece build from infinite permeability.

The flux distribution is found to be almost identical in all three conditions, as shown in Fig. 2.14; this proves that the MMF drop in the steel piece is negligible compared to the MMF drop in the sensor and two air gaps. Hence, (2.16) reduces to (2.14).

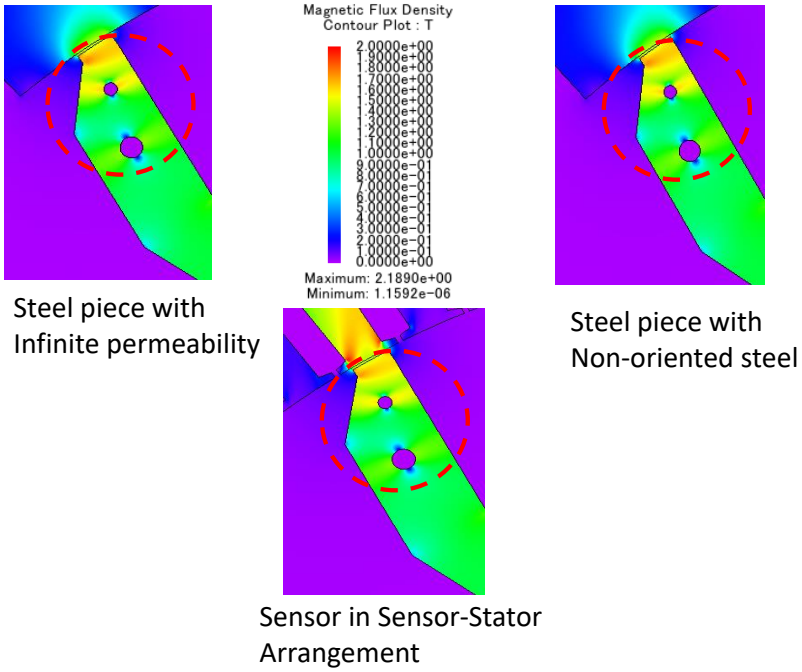

Figure 2.14: Flux Distribution, computed by JMAG FEA simulations, in the sensor limb at three different arrangements for Sensor C that shows flux density distribution in all three red circles is similar.

2.3 Experimental Set up

All the sensor limbs are identical, and the limb pickup coil voltage is maintained as a sinusoidal signal. The amplitude of the limb pickup coil voltage is adjusted by adjusting the drive coil supply voltage as discussed in [42], to obtain a desired flux density in the sensor limb ($\hat{B}_{limb}$). The experiment measures the total MMF drop of a portion of the segment, the sensor itself, and the air gaps between sensor limb and stator tooth. It also measures the total core loss of the sensor and the corresponding portion of the segment. The MMF drop/core loss of the portion of the stator segment is calculated by subtracting the MMF drop of the sensor and the air gaps/core loss of sensor. The MMF drop/core loss of the sensor and the two air gaps/sensor is calculated by measuring the MMF drop and core loss of two identical sensors placed head-on, as shown in Fig.2.15.

Both the drive coils are excited with the same current to obtain the desired flux density($\hat{B}_{limb}$) in the sensor limb. The total MMF drop of the setup consists of two sensors and four air gaps, each with a steel piece and sensor limb, and the total core loss of two sensors. Hence, the sensor's MMF drop/core loss and two air gaps are half of the total. The error due to the presence of steel pieces in the estimation of core losses and MMF drop is within acceptable limits by designing the area of the steel piece large enough such that the flux density is small.

The experimental setup consisting of a sensor and oriented steel segmented stator is shown in Fig. 2.16. A two-sensor arrangement, shown in [43], is used for testing to avoid flux leakage through back iron.

The drive coil voltage is applied through the amplifier, and the limb pickup coil voltage, pick-up voltage, and drive coil current are recorded using LabVIEW through an SCB box from National Instruments. The overall experimental setup consists of a computer that

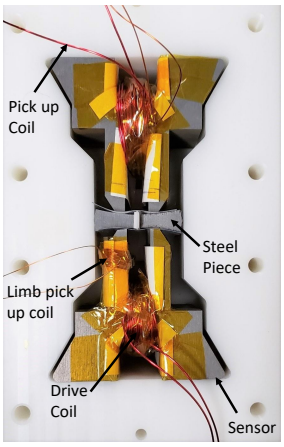

Sensor A experimental set up

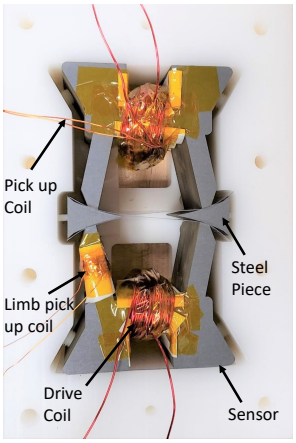

Sensor B experimental set up

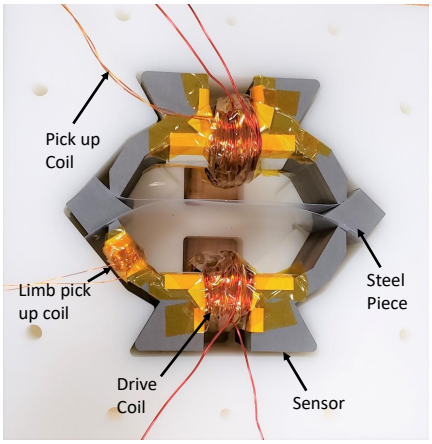

Sensor C experimental set up

Figure 2.15: Sensor characterization experimental set up with small steel pieces for all sensors [41].

controls LabVIEW, which is used to send and receive signals from the SCB box, and finally, the amplifier supplying voltage to the drive coil is shown in Fig.2.17.

2.4 Procedure for the Estimation of BH and Loss Curves of the Oriented Steel

The equations discussed in section 2.1 are used to calculate the values of core losses and MMF drop of X_i and T_i, details of the same are included in appendix C, at the selected

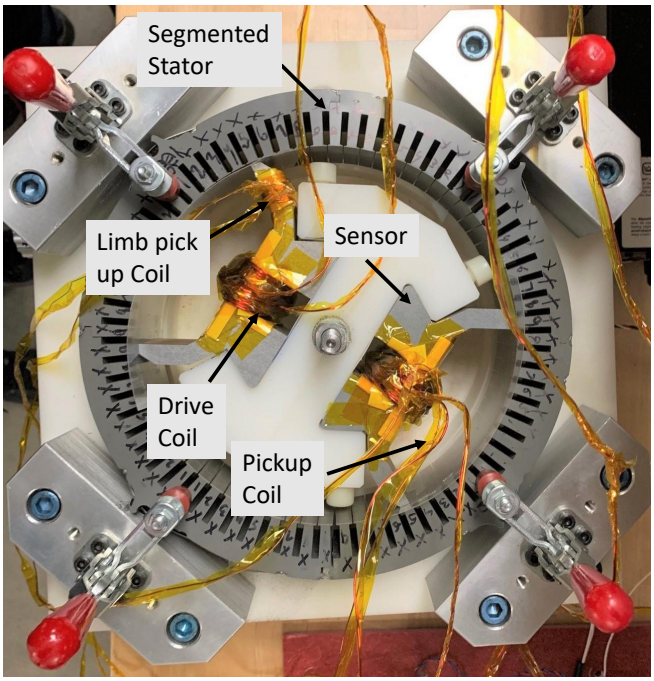

Figure 2.16: Experimental set up consisting of sensor and stator with the drive, pickup and limb pickup coils [41].

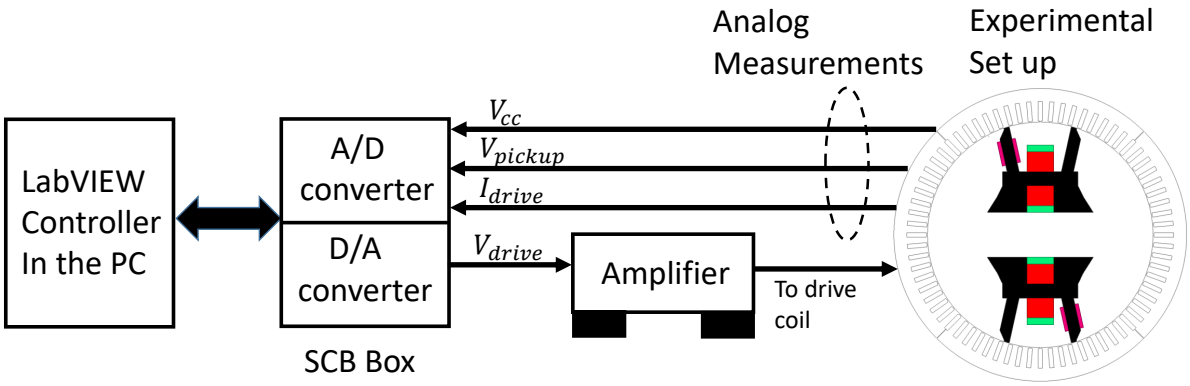

Figure 2.17: Schematics showing the overall experimental setup and its main components [41].

values of flux density and frequencies shown in Table.2.3.

The core loss and field intensity (H) for each orientation angle is calculated using the core loss and MMF drop values of X_i and T_i, combined with the data supplied by the manufacturer for the rolling and transverse directions. It is shown in section 2.1.2 that

Supply Frequency (n Hz)	Levels of $\hat{B}_{limb}$ (in T)
50	0.2, 0.4, 0.6, 0.8, 1.0, 1.2, 1.4, 1.5
100	0.2, 0.4, 0.6, 0.8, 1.0, 1.2, 1.4
150	0.2, 0.4, 0.6, 0.8, 1.0, 1.2, 1.3

Table 2.3: Values of $\hat{B}_{limb}$ and frequency used to perform the experiments

X_1 represents the properties of 90° away from the rolling direction, and X_2 represents the properties of 85° away from the rolling direction and so on. For a given value of flux density and frequency, the % change of core loss of X_i with X_i is:

$$\Delta x_i = \frac{Y_{X_i} - Y_{X_1}}{Y_{X_1}} \cdot 100 \tag{2.17}$$

Since X_1 is oriented at 90° away from the rolling direction, the core loss density in (W/m^3) in the transverse direction for the same value of flux density and frequency, denoted by $Y_{transverse}$, is used to calculate the core loss corresponding the angle of orientation of X_i. For example, the value of Y_{85° is calculated using the following:

$$\Delta x_2 = \frac{Y_{X_2} - Y_{X_1}}{Y_{X_1}} \cdot 100 = \frac{Y_{85^\circ} - Y_{transverse}}{Y_{transverse}} \cdot 100 \tag{2.18}$$

Therefore, the estimated value of core loss (in W/m^3) for the angle 85° away from the rolling direction at a given value flux density and frequency is:

$$Y_{85^\circ} = \frac{\Delta x_2 + 100}{100} \cdot Y_{transverse} \tag{2.19}$$

The exact process is repeated for all the values of X_i at all the flux densities and frequen-

cies values to obtain the core losses for the values of orientation from 85° to 45°. Moreover, flux data is generated using the MMF drop values of X_i from the process discussed above and using the value of H (in A/m) from the transverse direction. The calculations for all the orientation angles from 85° to 45° at a given value of flux density and frequency is summarized in Table.2.4.

Back Iron Component	Angle of Orientation	% change with Y_{X_1}	Core Loss Density(in W/m^3) or H (in A/m)
X_2	85°	Δx_2	$Y_{transverse} \cdot ((\Delta x_2 + 100)/100)$
X_3	80°	Δx_3	$Y_{transverse} \cdot ((\Delta x_3 + 100)/100)$
X_4	75°	Δx_4	$Y_{transverse} \cdot ((\Delta x_4 + 100)/100)$
X_5	70°	Δx_5	$Y_{transverse} \cdot ((\Delta x_5 + 100)/100)$
X_6	65°	Δx_6	$Y_{transverse} \cdot ((\Delta x_6 + 100)/100)$
X_7	60°	Δx_7	$Y_{transverse} \cdot ((\Delta x_7 + 100)/100)$
X_8	55°	Δx_8	$Y_{transverse} \cdot ((\Delta x_8 + 100)/100)$
X_9	50°	Δx_9	$Y_{transverse} \cdot ((\Delta x_9 + 100)/100)$
X_{10}	45°	Δx_{10}	$Y_{transverse} \cdot ((\Delta x_{10} + 100)/100)$

Table 2.4: Calculation of core loss (in W/m^3 or H(in A/m) for the back iron components X_i using the core losses or MMF drop obtained from the experiments for X_i at a given value of flux density and frequency, where $Y_{transverse}$ is the value of core loss density (in W/m^3) from the manufacturer data sheet at the same value of flux density and frequency

Finally, the core loss and MMF drop values of T_i with T_1 are used to estimate the core loss and BH curves for all the orientation angles from 0° to 40°.

2.5 Experimental Results

The estimated BH and loss curves were obtained from the core loss and MMF drop values of X_i and T_i using the analysis discussed in section 2.4, the details of the experimental results are included in appendix D. It was observed that the 55° away from the rolling direction has highest core losses, and the lowest losses are in the rolling direction. This is a long-known result and proves the correctness of the proposed method. The same varition is shown by the permeability. However, for the FEA interpolated curves the rolling direction has the lowest losses, and the transverse direction has the highest losses. The core loss curves obtained from the analysis of the experimental results and FEA interpolated core loss curves at 50 Hz supply frequency are shown in Fig.2.18.

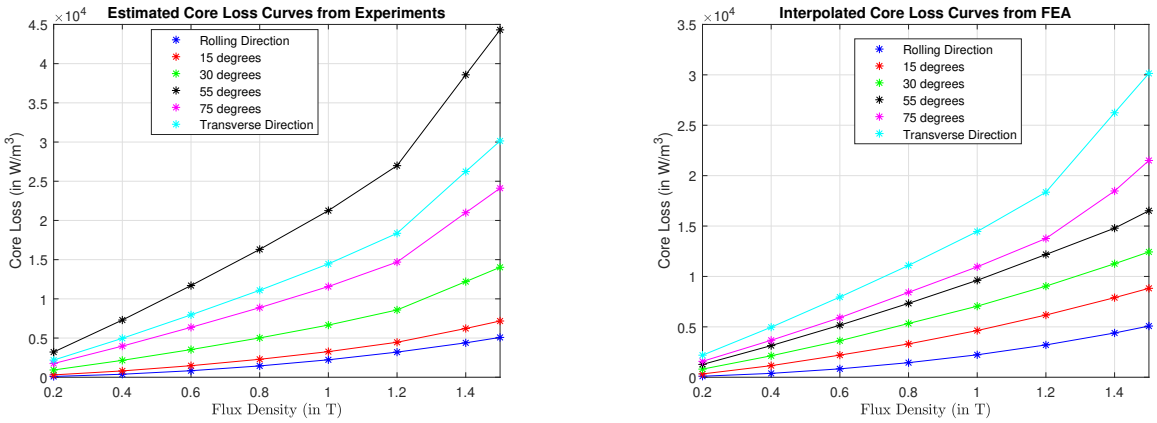

(a) Experimental Results (b) FEA Results

Figure 2.18: Comparison of the core losses obtained from the analysis of experimental results and FEA interpolated core loss curves using the inbuilt function in the JMAG software for different angles away from the rolling direction at supply frequency of 50 Hz

The variation of core loss curves with the orientation angle obtained from the analysis of experimental results and FEA interpolated core loss curves for 1.5 T and supply frequency of 50 Hz is shown in Fig.2.19. This variation shows the difference between the interpolated properties of the oriented steel in the FEA (the conventional method) compared to the actual

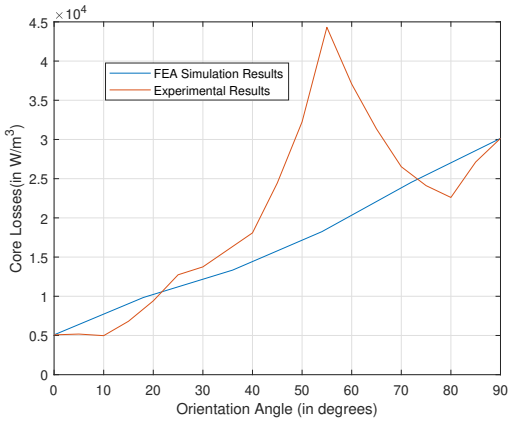

Figure 2.19: The variation of core losses with orientation angle obtained from the analysis of experimental results and simulations using JMAG FEA software at 1.5 T and supply frequency of 50 Hz

properties of the oriented steel obtained from the experiments. This shows the importance of the proposed method to obtain the characteristics of oriented steel for correct modeling of the oriented steel modular PMSM.

2.6 Conclusion

In this chapter, a method to estimate the magnetic characteristics of the oriented steel is proposed. A newly designed experimental setup was developed to obtain the magnetic characteristics of the oriented steel. It is shown that the experimentally-estimated magnetic characteristics of the oriented steel are different from the FEA method that utilizes the properties of both rolling and transverse direction to interpolate the magnetic characteristics.

Chapter 3

Impact of Segmentation Parameters on Core Loss and Average Torque of Oriented Steel Segmented Stator PMSM

In [44] general design rules for average torque maximization in segmented stator machines are proposed. However, the proposed rules are limited to fractional slot concentrated winding machines. Moreover, in [11,12] the core loss minimization in the segmented stator is achieved by using oriented steel in the stator. However, the impact of design parameters on the core loss is not discussed. Therefore, the impact of design parameters on the core loss and average torque is missing in the current state of the art that can be extended to the integral slot machines. In this chapter, a new theory to determine the impact of segmentation parameters, the number of segments(N_s) and length of parasitic gap(g_p), on the average torque, core loss, d axis flux(λ_d), and q axis flux(λ_q) that is applicable for integral slot machines is proposed. The proposed theory is validated using FEA simulations.

3.1 Impact of Segmentation on the Core Loss and Average Torque

Segmentation increases the overall reluctance of the stator due to the additional parasitic gaps between the segments. The flux distribution changes when there is a possibility of avoiding the high reluctance path and increasing the overall co-energy. One such possibility is when the number of segments (N_s) is such that the poles per segment are even number, which changes the flux direction that leads to the following:

1. Increase in core loss with increase in parasitic gaps.

2. Decrease in flux linkage with increase in parasitic gap while increasing the co-energy.

3.1.1 Proposed Theory to Show the Impact of Even Poles per Segment on Core Loss and Average Torque

In this section, the claims made in the previous section are supported using the proposed theory that discusses the flux distribution in PMSM due to segmentation.

It is shown in [45] that the rotation of the rotor leads to change only in the co-energy for the air gap. Therefore, only the co-energy in the machine air gap is considered, and the co-energy change due to stator slots is ignored. The co-energy in the air gap of the machine is:

$$W_{air} = \frac{1}{2 \cdot \mu_o} \cdot \int_V B_{air}^2 \, dV \tag{3.1}$$

where μ_o is the permeability of the air, B_{air} is the air gap flux density, and dV is the

differential volume along the circumference of the rotor. The rotor tends to align in the maximum co-energy position, which is stable equilibrium position [46].

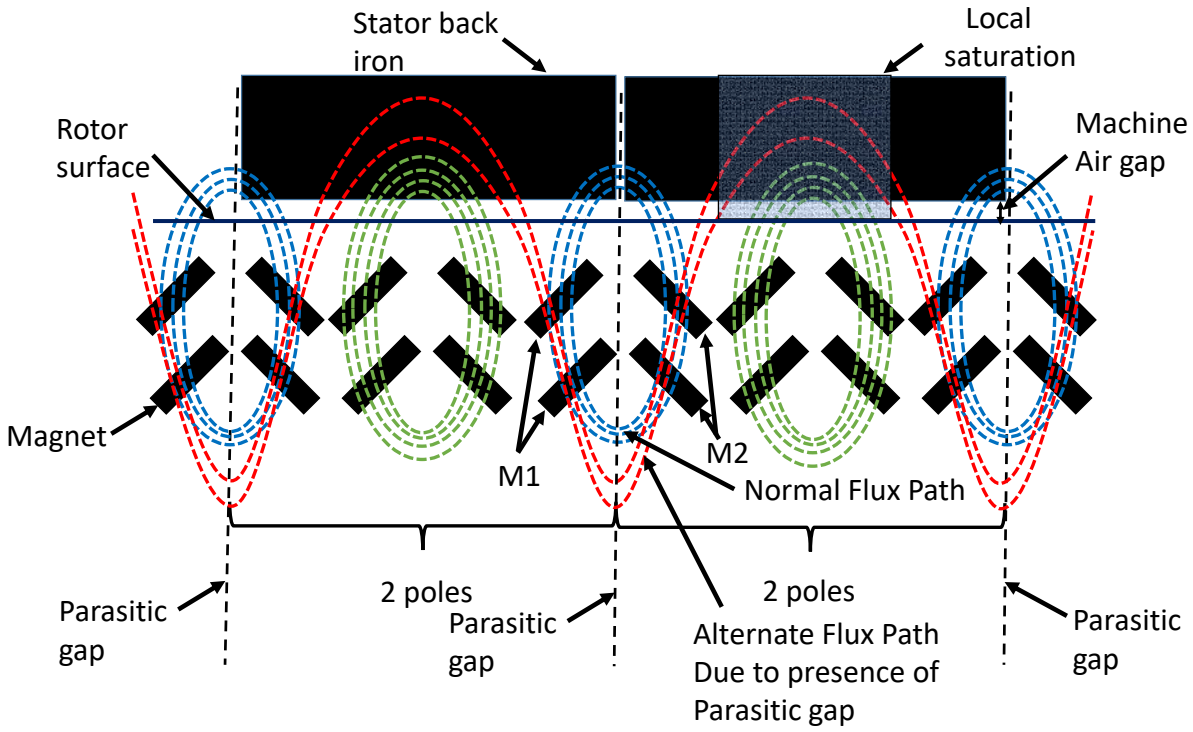

Figure 3.1: Symmetrical flux distribution with 2 poles per segment leading to local saturation in the back iron due to flux splitting.

If the flux path is through the parasitic gaps, then there is a decrease in the flux density and consequently a decrease in the co-energy. When the poles per segment are an even number, the flux lines change the direction to avoid the parasitic gap to maximize the co-energy. The flux lines under the no-load condition when there are two poles per segment are shown in Fig.3.1.

The flux from the magnets M1 and M2 complete the blue path if there is no parasitic gap. However, when the parasitic gaps are present, the flux follows the red path that avoids the parasitic gaps. This alternate path for the flux is only preferable when the poles per segment are an even number. Any other poles per segment will force the red path to encounter at least

one parasitic gap. If the increased flux concentration does not change the steel permeability, all the flux from the magnets M1 and M2 will follow the red path. However, the permeability of the steel decreases with saturation, and hence some flux still follow the blue path, while some follow the red path. Therefore, the presence of an even number of poles per segment leads to the following:

1. Increase in core loss due to local saturation and increases further with the parasitic gaps.

2. Decrease in flux linkage, which further decreases with increase in parasitic gap, due to high reluctance path due to both saturated steel and parasitic gaps. However, this still increases the co-energy of the machine.

Moreover, a decrease in overall flux linkage leads to a decrease in average torque.

The proposed theory shows that the flux path changes in machines with even poles per segment, increasing core loss and decreasing average torque. For any other combination of design parameters, no such effect is possible.

3.2 Impact of Segmentation and Change in Steel on λ_d and λ_q

Segmentation leads to decrease in the flux linkage due to the parasitic gaps, and the decrease in the q axis flux linkage is more prominent than the d axis flux linkage. Moreover, improving the quality of the steel increases q axis flux linkage more than the d axis flux linkage.

3.2.1 Proposed Theory to Determine Impact of Segmentation and Change in Steel on λ_d and λ_q

In this section, the effect of parasitic gaps due to segmentation and change in steel on the variation of λ_d and λ_q linkage is explained using the first reluctance path, the second reluctance path, and the magnet path, proposed in [47], as shown in Fig.3.2.

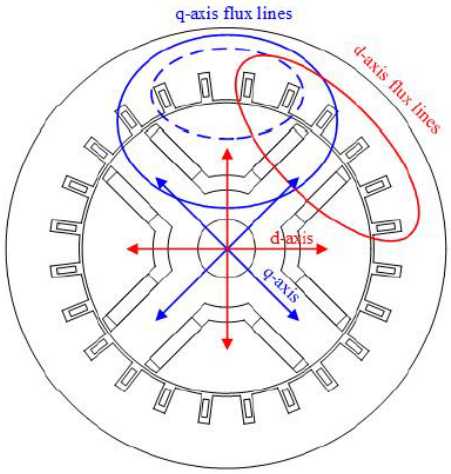

Figure 3.2: IPM flux paths: first reluctance path (solid blue), second reluctance path (dashed blue), and magnet path (solid red) [47].

In [47] it is stated that the primary and secondary reluctance flux paths contribute towards λ_q, while the magnet flux path contributes towards λ_d. The presence of parasitic gaps between the segments in the stator leads to an increase in the reluctance in the direction of both d- and q-axis flux paths. The reluctance in the d-axis flux path in the nonsegmented stator is due to the magnet, the machine air gap, and steel in both the stator and rotor. In comparison, the reluctance in the q-axis flux path in the nonsegmented stator is only due to the machine air gap and steel in both stator and rotor. The reluctance of rare earth magnets is close to that of air. Therefore, segmentation leads to a more significant change in the reluctance for the q-axis than the d-axis; the decrease in the q-axis flux is more dominant

than the change in the d-axis flux. Moreover, the change in flux linkage due to the improved quality of steel is more prominent in the q-axis than the d-axis.

3.3 Example Machines Used for the Validation of the Proposed Theories Using FEA Simulations

The theories proposed in sections 3.1 and 3.2 are validated using the two example PMSMs: Machine A has 12 poles/72 slots, and Machine B has 8 poles/72 slots. Fig.3.3 shows the cross-section of the machines, and the machine specifications are shown in Table.3.1.

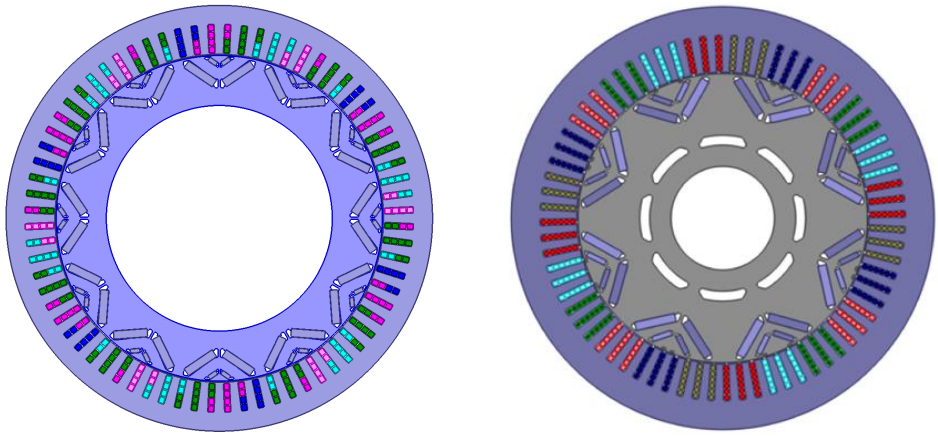

(a) Machine A (b) Machine B

Figure 3.3: Cross section of the PMSMs used an example in JMAG simulation software.

Laser-cutting tolerances result in a maximum possible parasitic gap of 0.2 mm. Therefore, in this study, the value of parasitic air gap length (g_p) is increased from 0 mm, which is the ideal case, to 0.2 mm in steps of 0.05 mm.

Machine Specifications	Machine A	Machine B
Number of Poles	12	8
Number of Slots	72	72
Stator inner Diameter	203.5 mm	140.75
Stator outer Diameter	264 mm	204
Motor Stack Length	51.5 mm	125 mm
Machine Air Gap	0.75 mm	0.625 mm
Winding Type	Distributed Double Layer	Distributed Single Layer
Coil Pitch	6	9

Table 3.1: Machine Specifications.

3.4 Validation of the Proposed Theory in Section 3.1 Under No Load Conditions in FEA Simulations

In this section the validation of the theory proposed in section 3.1 using the two example machines discussed in section 3.3 is discussed. The theory states: When the number of segments (N_s) is such that the poles per segment are even number, it leads to an increase in the core losses and decreases the flux linkage. To validate this statement machines A and B are simulated for N_s = 3, 4, 6, 8, 9, 12 and 18, and N_s = 2, 3, 4, 6, 8, 9, 12 and 18 respectively under no-load condition at 100 Hz of electrical frequency. Moreover, for each value of N_s the value of parasitic gap length (g_p) is swept from 0 to 0.2 mm in steps of 0.05 mm as discussed in section 3.3.

The conceptual drawing of the flux splitting for Machine A with N_s = 3, 4 poles per segment, is shown in Fig.3.4.

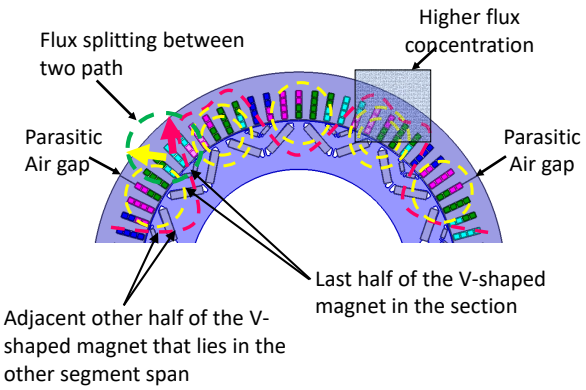

Figure 3.4: Conceptual Drawing of Flux splitting due to the presence of parasitic gaps when 4 poles per segment are present in Machine A.

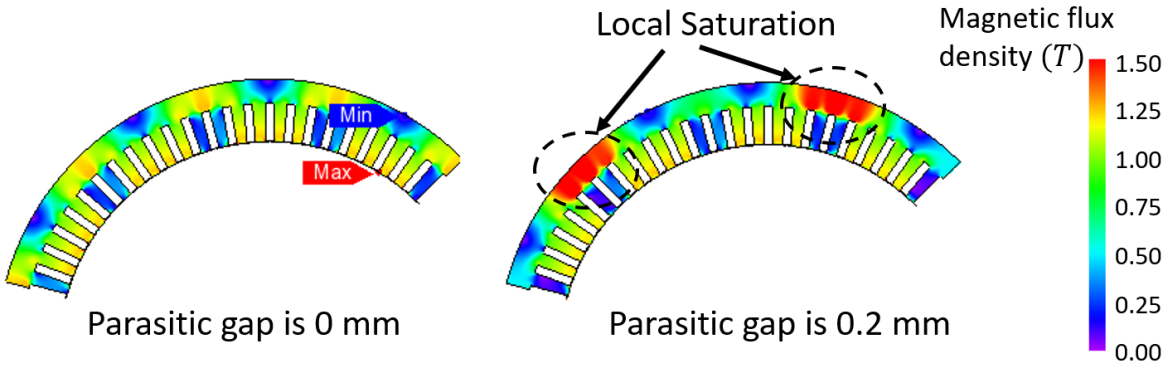

(a) Flux density distribution

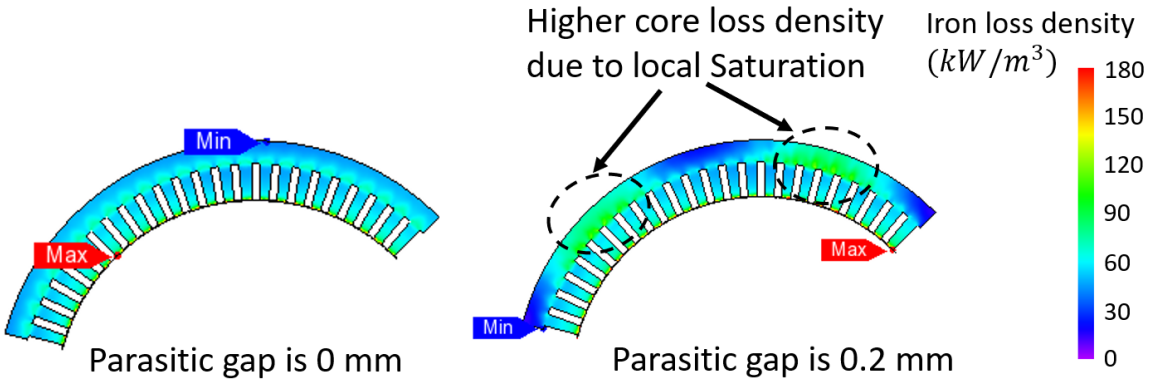

(b) Core loss distribution

Figure 3.5: Flux density distribution under no-load condition for the machine A consisting of 3 segments when both halves of the V-shaped magnets are aligned with the segments, and the no load core loss density distribution at 100 Hz of electrical frequency presenting the impact of local saturation due to the presence of parasitic gap calculated using JMAG simulation software.

The corresponding local saturation showed by flux density distribution under non-zero parasitic gap condition, and the corresponding core loss density when poles per segment are 4, $N_s = 3$, is shown in Fig.3.5.

Moreover, the flux density distribution of Machine B is shown in Fig.3.6 for $N_S = 4$ (2 poles per segment), which indicates the lower flux density compared to machine A due to thicker back iron.

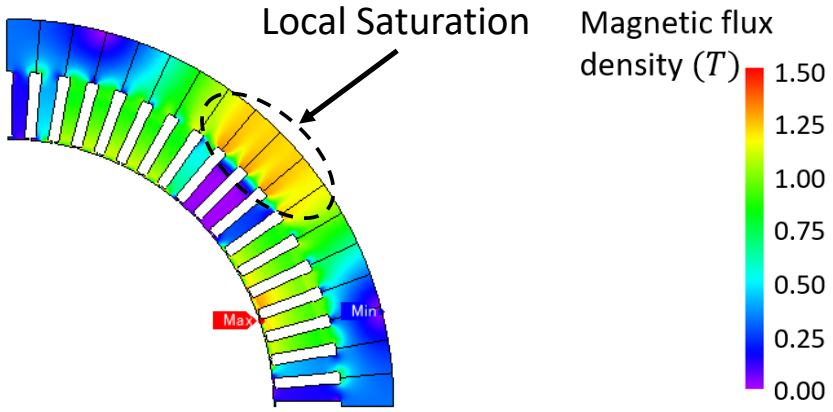

Figure 3.6: Flux density distribution under no load condition, of one segment, for the machine B consisting of 4 segments (2 poles per segment) when both halves of the V-shaped magnets are aligned with the segments with 0.2 mm parasitic gap calculated using JMAG simulation software.

3.4.1 Core Loss

The no-load core loss variation of the complete stator for both Machines A and B is shown in Fig.3.7. The core losses increase in large proportions with the parasitic gap when the poles per segment are 2 and 4 for $N_s = 6$ and $N_s = 3$ for machine A, and $N_s = 4$ and $N_s = 2$ for machine B as shown in Fig.3.7. This validates the proposed theory in section 3.1.

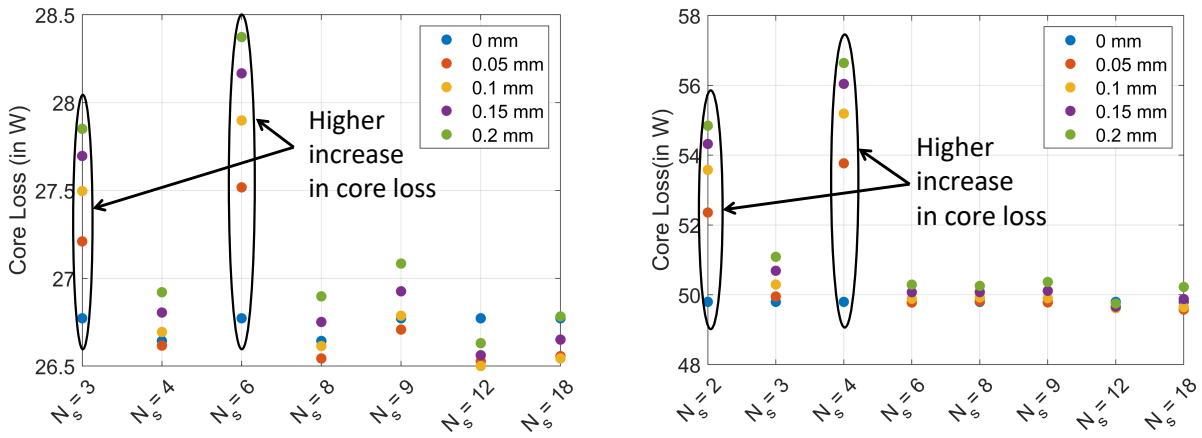

(a) Machine A (b) Machine B

Figure 3.7: No load core loss variation with the number of segments(N_s) and parasitic gaps (g_p) for machines A and B of the complete stator at 100 Hz of electrical frequency calculated using JMAG simulation software.

3.4.2 Flux Linkage from the Magnets(λ_{pm})

The values of λ_{pm} decrease with the increase in the parasitic gap because of the increased reluctance from the segmented stator. The decrease in values of λ_{pm} is more prominent with the higher number of segments as shown in Fig.3.8 for both machines. The exception to this variation is shown with $N_s = 3$ (4 poles per segment) and $N_s = 6$ (2 poles per segment) for machine A. The values of λ_{pm} for machine A with $N_s = 3$ and $N_s = 6$ is lower with $N_s = 4$ and $N_s = 8$ respectively. The reason for this exception is the local saturation due to the flux splitting as explained in section 3.1, which leads to a further decrease in the values of the λ_{pm} due to the higher permeability from the saturated back iron; this further validates the proposed theory.

However, for values of λ_{pm} for machine B with $N_s = 2$ (4 poles per segment) and $N_s = 4$ (2 poles per segment) is higher with $N_s = 3$ and $N_s = 6$ respectively, which is the expected variation; this is because of the thicker back iron of machine B that does not lead to higher saturation as shown in Fig.3.6, and hence do not surpass the effect of the higher parasitic

gaps from $N_s = 2$ to $N_s = 3$.

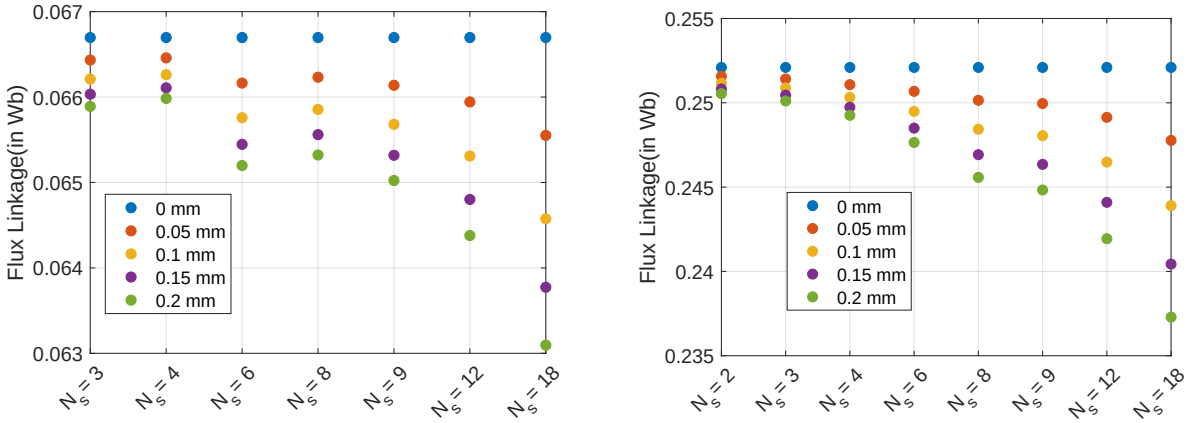

(a) Machine A

(b) Machine B

Figure 3.8: Variation of λ_{pm} for machines A and B with the number of segments(N_s) and parasitic gaps (g_p) calculated using JMAG simulation software.

3.5 Validation of the Proposed Theories Under Loaded Conditions

The theories proposed in sections 3.1 and 3.2 are validated using example machines A and B under loaded conditions at 100 A, 120°, and 100 Hz of electrical frequency (Point O). Same values of N_s and g_p, used in no-load validation, are used under loaded conditions. First, the impact of segmentation is discussed on the d-axis and q-axis flux. After that, the impact on core loss under loaded conditions is discussed. Finally, the impact of segmentation for the average torque is discussed.

3.5.1 d-axis flux linkage (λ_d) and q-axis flux linkage (λ_q)

Fig.3.9 shows the variation of λ_d and λ_q at point O for machine A with the parasitic gaps and number of segments.

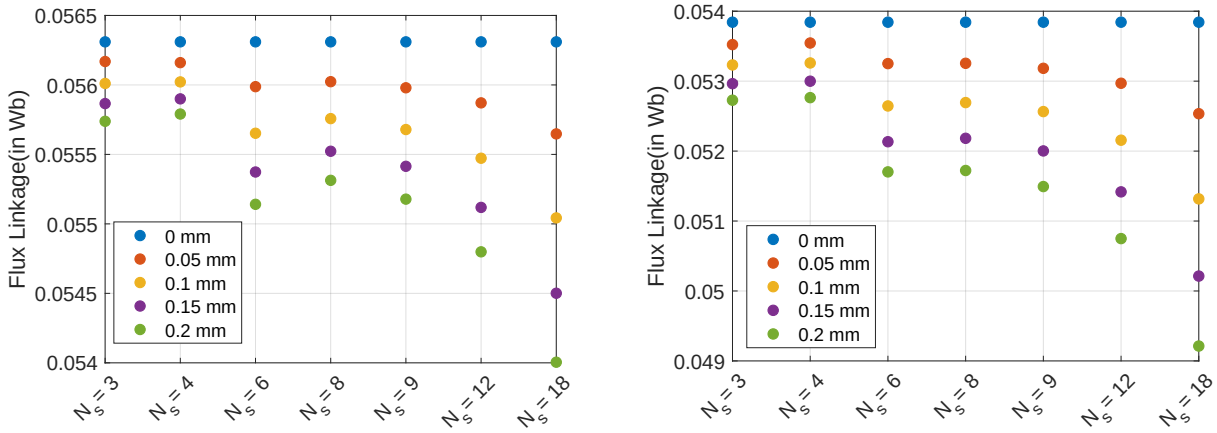

(a) λ_d variation (b) λ_q variation

Figure 3.9: Variation of λ_d and λ_q for machine A with the number of segments(N_s) and parasitic gaps (g_p) at point O calculated using JMAG simulation software.

The values of λ_d and λ_q decrease, as shown in Fig.3.9, due to the increase in the values of parasitic gaps. The decrease in the values of λ_d and λ_q is higher, as proposed in the theory in section 3.2, for higher values of the number of segments. An exception to this variation is the change in λ_d and λ_q from $N_s = 3$ to $N_s = 4$, and $N_s = 6$ to $N_s = 8$ due to the local saturation explained earlier. Another observation is that the change in the values of λ_q with the parasitic gap is more prominent than λ_d. Again, this is predicted by the proposed theory in section 3.2.

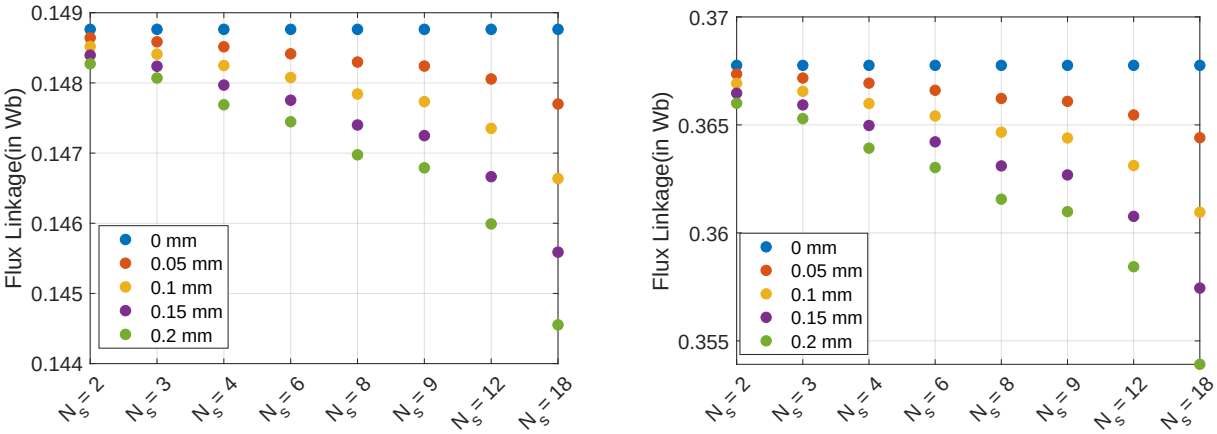

(a) λ_d variation (b) λ_q variation

Figure 3.10: Variation of λ_d and λ_q for machine B with the number of segments(N_s) and parasitic gaps (g_p) at point O calculated using JMAG simulation software.

However, for machine B, the decrease in λ_d and λ_q with increasing N_s for a given nonzero parasitic gap is as expected, as shown in Fig.3.10 because the local saturation is not prominent due to higher back iron thickness. Moreover, change in the values of λ_q with the parasitic gap is more prominent than λ_d, which is predicted by the proposed theory in section 3.2.

3.5.2 Core Loss

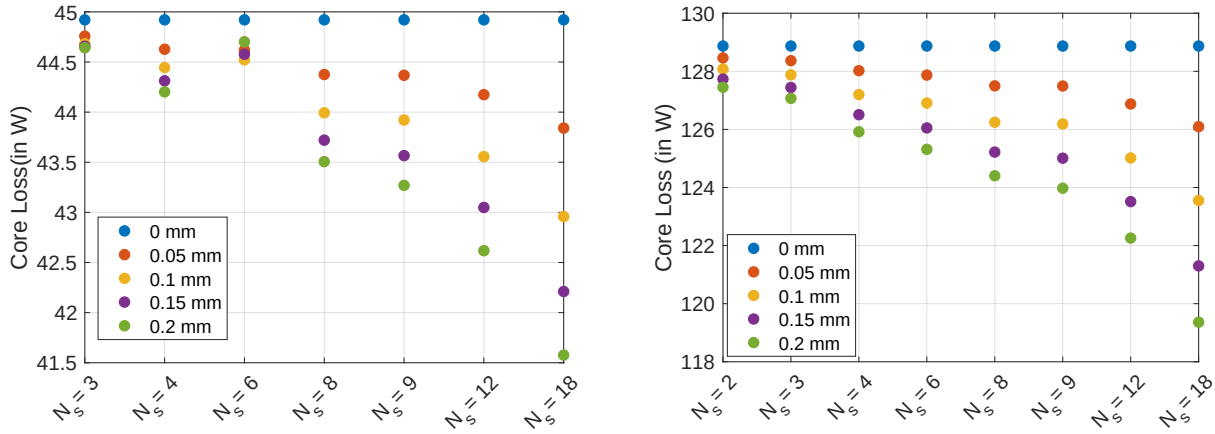

(a) Machine A (b) Machine B

Figure 3.11: Core loss variation with the number of segments(N_s) and parasitic gaps (g_p) for machines A and B of the complete stator at point O calculated using JMAG simulation software.

The variation of core losses with the number of segments (N_s) and parasitic air gaps for point O, for machine A, is shown in Fig.3.11(a). The core losses for $N_s = 3$ and $N_s = 6$ show a lower decrease in the core losses with the parasitic gaps compared with other values of N_s even though there is a more significant decrease in overall flux linkage as shown in Fig.3.9. As explained earlier, this is due to higher saturation levels when the poles per segment are an even number that leads to higher losses even at lower overall flux linkage. However, for Machine B, the core losses decrease with an increase in the parasitic gap and a higher decrease with an increased value of N_s as shown in Fig.3.11(b); this is due to lower back

iron saturation in machine B.

3.5.3 Average Torque

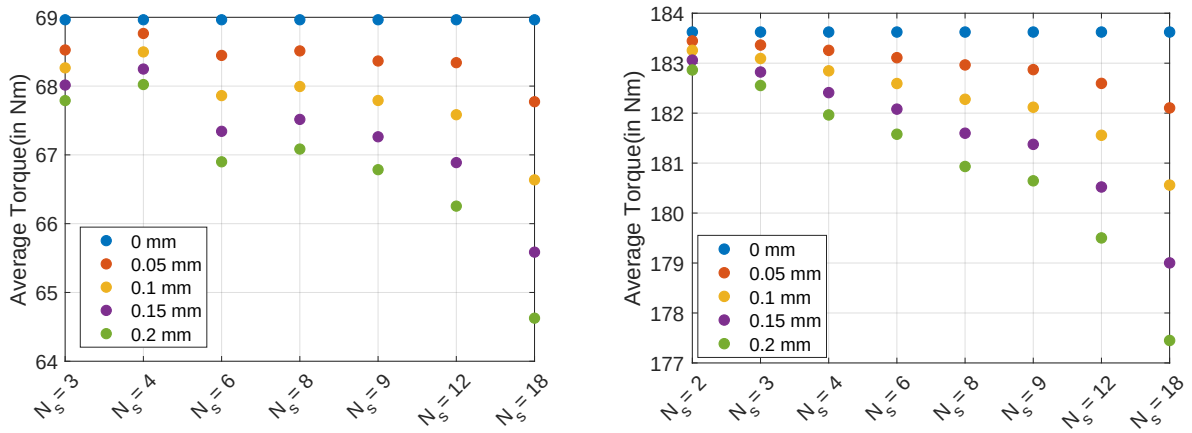

(a) Machine A

(b) Machine B

Figure 3.12: Variation of Average Torque for machines A and B with the number of segments(N_s) and parasitic gaps (g_p) at point O calculated using JMAG simulation software.

The equation of average torque for an IPMSM is:

$$\text{Average Torque} = 1.5p(\lambda_d i_q - \lambda_q i_d) \tag{3.2}$$

where p is the pole pairs and i_d and i_q are the d and q axis currents. Therefore, for the same values of i_d and i_q, the variation of the average torque is similar to the variation of λ_d and λ_q as shown in Figs.3.9 and 3.10 respectively. Fig.3.12 shows the variation of average torque at point O for both machines A and B for all values of segments and parasitic gaps.

3.6 Conclusions

In this chapter, a general theory to determine the impact of segmentation parameters on the average torque and core loss is proposed. Moreover, applying the reluctance theory for IPMSM is used to determine the impact of segmentation on d axis flux(λ_d), and q axis flux(λ_q). The proposed theory states that the even poles per segment increase core loss and may lead to a decrease in average torque. Moreover, based on the reluctance theory, the parasitic gaps due to segmentation decrease the q-axis flux more than the d-axis flux. Both the proposed theories are validated using the FEA on two example machines: machine A, 12 poles/72 slots, and machine B, 8 poles/72 slots.

Chapter 4

Impact of Segmentation Parameters on Cogging Torque and Back Electromotive Force of Oriented Steel Segmented Stator PMSM

This chapter proposes and validates a novel theory to determine the impact of segmentation on the cogging torque. The proposed theory predicts the impact of different combinations of design parameters on the cogging torque, which is vital for machine designers. Moreover, the balanced back electromotive force conditions are proposed and validated, applicable for both single and double layer integral slot distributed winding.

First, the proposed theory to determine the impact of segmentation parameters on the cogging torque in segmented stator PMSM is discussed, followed by the validation of the proposed theory in FEA simulations using the two example machines discussed in chapter 3. After that, the conditions to obtain balanced BEMF are proposed, followed by validating the proposed conditions in FEA simulations using the same two machines.

4.1 Cogging Torque in Segmented Stators

Cogging torque in the segmented stator exists due to the pole-slot interaction and pole-parasitic gap interaction [48]. It is also shown in [48] that the segmentation does not affect the cogging torque due to pole-slot interaction. Moreover, due to stator slotting, the offset on the amplitude of the cogging torque due to pole-parasitic gap interaction is constant. Therefore, for a fixed geometry of slots, the variation of cogging torque due to pole-parasitic gap interaction is due to N_s/g_p only. Therefore, in this study, the two cogging torques are treated independently.

4.1.1 Cogging Torque due to Pole-Slot Interactions

In this section, the basic concepts of the cogging torque due to pole-slot interactions are discussed. The tendency of the permanent magnet rotor to align to a position of maximum co-energy leads to an increase in cogging torque. When the magnet inter-pole axis coincides with the teeth for a full pole-pitched magnet, then the co-energy is maximum; the reluctance offered to the flux path for the edges of magnets is minimum, and the position is referred to as a stable equilibrium position. On the other hand, when the magnet inter-pole axis coincides with the slot, the co-energy is minimum, and the position is referred to as an unstable equilibrium position [46]. The same concept can be extended to a short pole-pitched magnet where the equilibrium is with respect to the relative placement of the magnet edge with the tooth or slot, which is shown in Fig. 4.1.

Moreover, it is shown in [49] that the co-energy stays constant until the magnet edge approaches the slot opening edge. The fundamental electrical order of the cogging torque due to slot-pole interactions, as discussed in [46, 49], is:

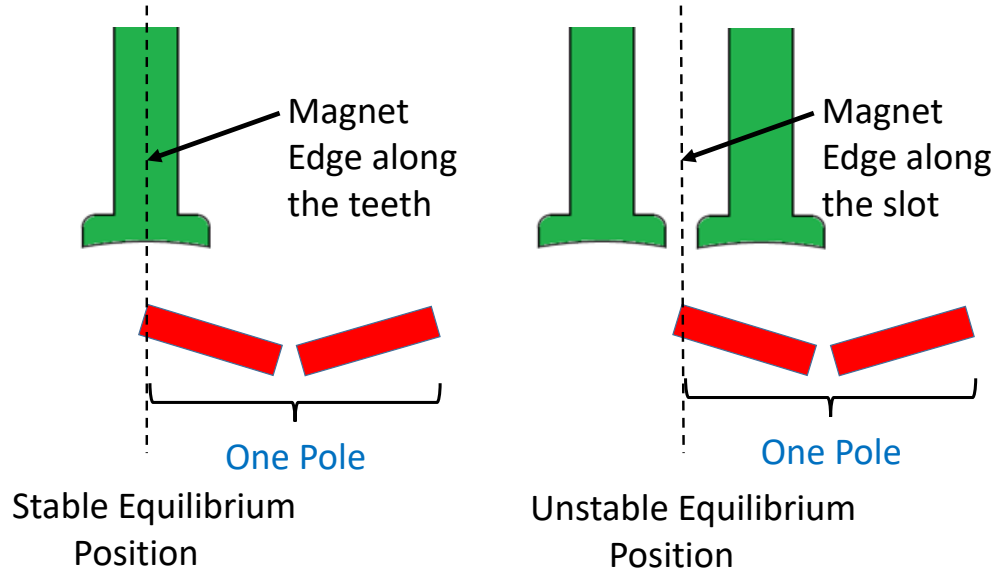

Figure 4.1: Stable and unstable equilibrium positions due to pole-slot interaction

$$\frac{2 \cdot Z_s}{\mathrm{GCF}(2p, Z_s)} \tag{4.1}$$

where 2p is the number of poles, and Z_s is the number of slots. Moreover, the value of cogging torque is zero at both equilibrium positions.

4.2 Proposed Theory

In this section, first the equilibrium positions for the pole-parasitic gap interactions is defined, followed by applying the concept of equilibrium positions due to both pole-slot and pole-parasitic gap interactions to determine impact of segmentation parameters on the cogging torque.

4.2.1 Equilibrium Positions due to Pole-Parasitic Gap Interactions

The co-energy in the air varies with rotor position in segmented stator machine, as flux from the magnets passes through the parasitic gaps in some positions, while in some positions, it does not. For a given pole pair, the co-energy is minimum and maximum in a position, where the flux passes and does not pass through the parasitic gap, defined as unstable and stable equilibrium positions, respectively, in this work. Fig.4.2 shows the stable and unstable equilibrium positions in the PMSM manufactured using a segmented stator. For the sake of clarity, only the back iron is shown.

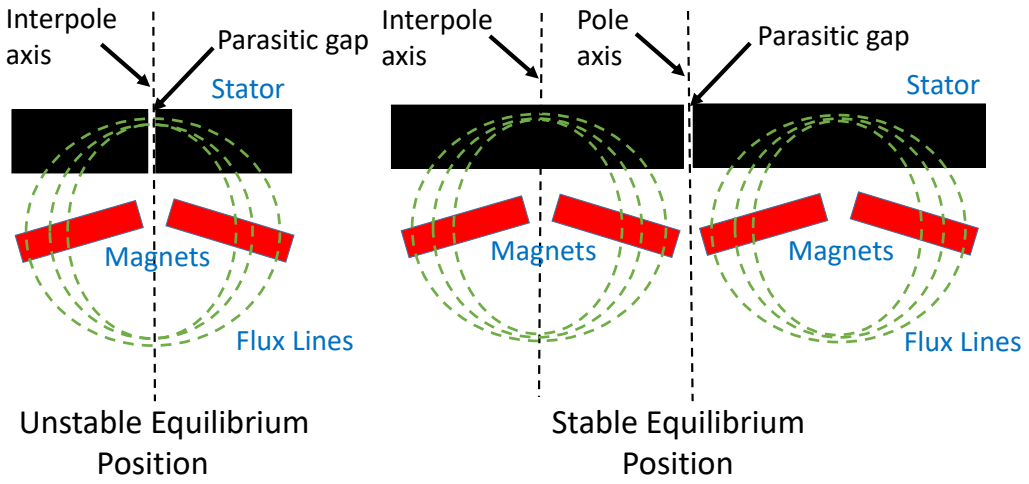

Figure 4.2: Stable and unstable equilibrium positions due to pole-parasitic gap interaction

The fundamental electrical order of the cogging torque due to pole-parasitic gap interaction, as discussed in [48], is:

$$\frac{2 \cdot N_s}{\mathrm{GCF}(2p, N_s)} \tag{4.2}$$

4.2.2 Proposed Theory to Determine the Impact of Segmentation Parameters on Cogging Torque

The proposed theory states that the cogging torque of the segmented stator might increase or decrease if the order of the two cogging torque due to pole-slot and pole-parasitic gap interactions is the same. Further, if the number of segments is such that the poles per segment is/are an integer, it may lead to a very high peak of the cogging torque. Finally, if the number of segments is such that the poles per segment are an odd multiple of half, it may lead to a very high peak of the cogging torque. All the claims are shown to be accurate by using the concept of stable and unstable equilibrium positions for both pole-slot and pole-parasitic gap interactions in the following sub-sections.

4.2.2.1 Order of Cogging Torque Due to Pole-Slot Interaction and Pole-Parasitic Gap Interaction is Same

The stable and unstable equilibrium positions due to pole-slot and pole-parasitic gap interactions, respectively, are the same due to the segmentation being performed along the direction of the slot. This position is shown in Fig.4.3. Mathematically, the condition for cogging torque electrical order, due to the two interactions, are equal from (4.1) and (4.2) is:

$$\frac{2 \cdot N_s}{\mathrm{GCF}(2p, N_s)} = \frac{2 \cdot Z_s}{\mathrm{GCF}(2p, Z_s)} \tag{4.3}$$

Therefore, if both the cogging torques have similar electrical order, the transition from stable to unstable equilibrium position with rotation is the opposite. Therefore, If the parasitic air gap and slot opening are designed such that the change in co-energy due to

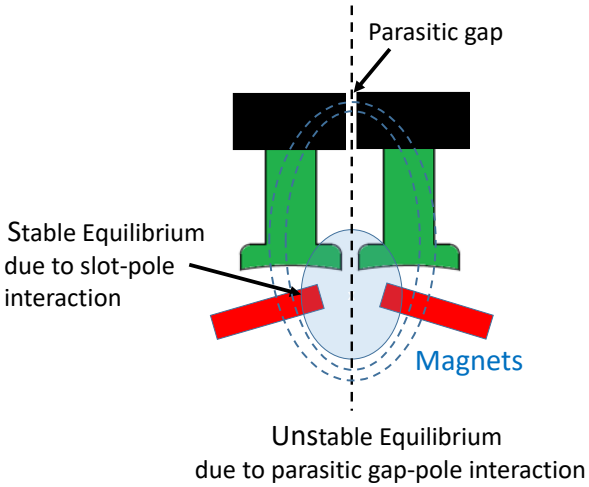

Figure 4.3: Stable and unstable equilibrium positions due to pole-slot and pole-parasitic gap interactions respectively at same position when the order is same.

rotation is minimum, then the peak of the cogging torque can be minimized. However, if the number of segments is large enough, the two cogging torques might have an additive effect; this might be possible due to the alignment of the pole axis along the parasitic gap, which is the stable equilibrium position for pole-parasitic gap interaction, as shown in Fig.4.4. This relative placement of the magnet and the parasitic gap depends on the machine design.

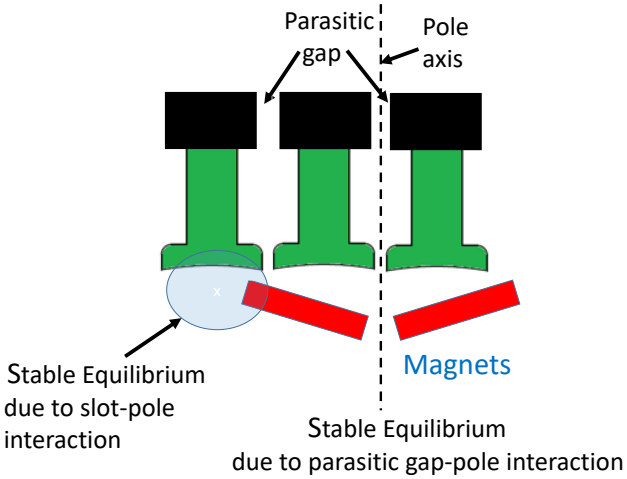

Figure 4.4: Stable equilibrium positions due to pole-slot and pole-parasitic gap interactions at same position when the order is same.

4.2.2.2 Poles per Segment is an Integer

If pole(s) per segment is(are) an odd number, then there are two extreme positions. No flux from all-pole pairs passes through the parasitic gaps in one position, while in the second position, it does. Due to a more considerable change in co-energy in these two positions, the peak of the cogging torque is also very high. Fig.4.5 shows the flux distribution when poles per segment is an odd number in the two positions above.

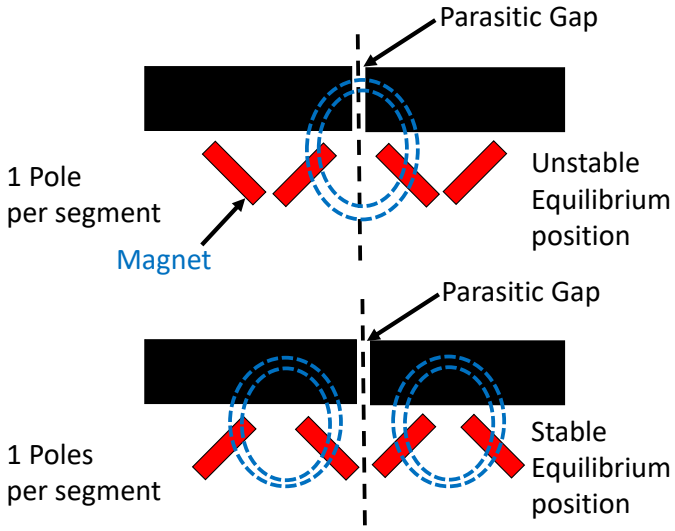

Figure 4.5: Flux distribution of stable and unstable equilibrium positions when poles per segment is an odd number.

The only difference between odd and even poles per segment is the flux splitting, as explained in section 3.1, which leads to a lower change in co-energy, and hence comparatively lower cogging torque. Moreover, it is shown in section 3.1 the flux splitting leads to local saturation that restricts the increase in the co-energy. Therefore, in machines where the back iron is not exceptionally large, the cogging torque is expected to be higher when poles per segment are an even number.

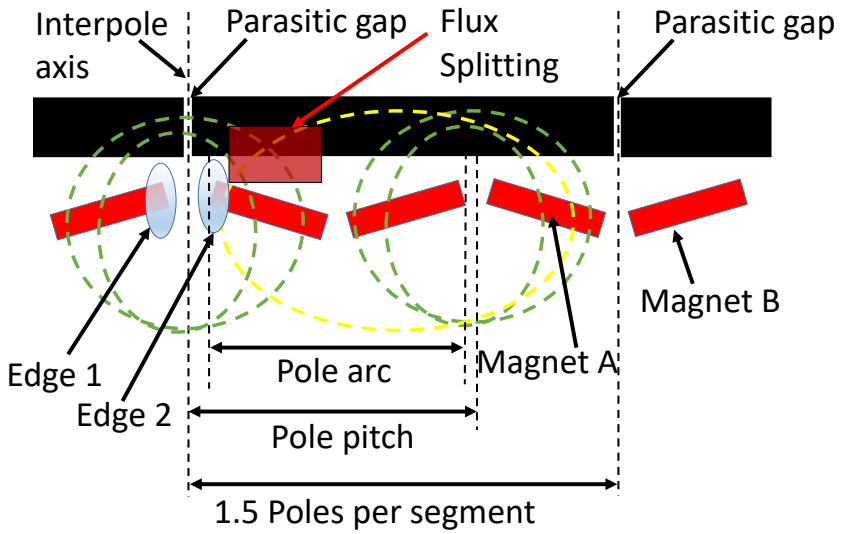

Figure 4.6: Flux distribution when number of poles per segment is 1.5.

4.2.2.3 Poles per Segment is (2n+1/2) where n is an integer such that $n \geq 0$

When the number of poles per segment is (2n+1/2), where n is an integer such that $n \geq 1$, the flux redistributes to maximize the co-energy. This energy distribution leads to two stable equilibrium positions when the pole pitch is greater than the pole arc. Three positions are discussed to explain the presence of two stable equilibrium positions, which is shown in Fig.4.6:

1. Position 1: When edge 1 is along the parasitic gap.

2. Position 2: When inter-pole axis is along the parasitic gap.

3. Position 3: When edge 2 is along the parasitic gap.

The positions 1 and 3 are identical due to the symmetry.

In all three positions, some parts of flux complete the path through the adjacent magnet to avoid the parasitic gap, as shown by yellow dotted lines in Fig.4.6, which leads to two

different energy levels corresponding to positions 1/3 and 2. Position 1/3 has higher co-energy due to the participation of adjacent magnets, for example, magnet B adjacent to magnet A, to aid more flux splitting. Therefore, small peaks appear between position 1-position 2 and position 2-position 3 and higher peaks between stable-unstable equilibrium positions. The increase in the difference between stable-unstable equilibrium positions may be considerably higher if the flux splitting, dependent on machine design, is high. The energy diagram and corresponding cogging torque are shown in Fig.4.7.

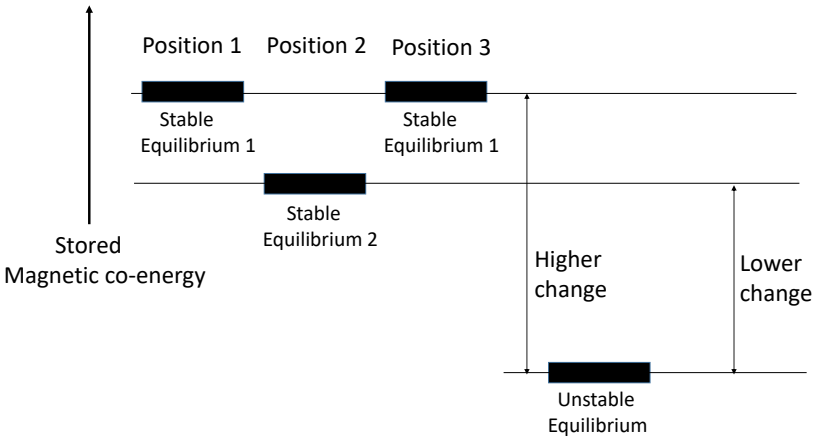

(a) Energy levels

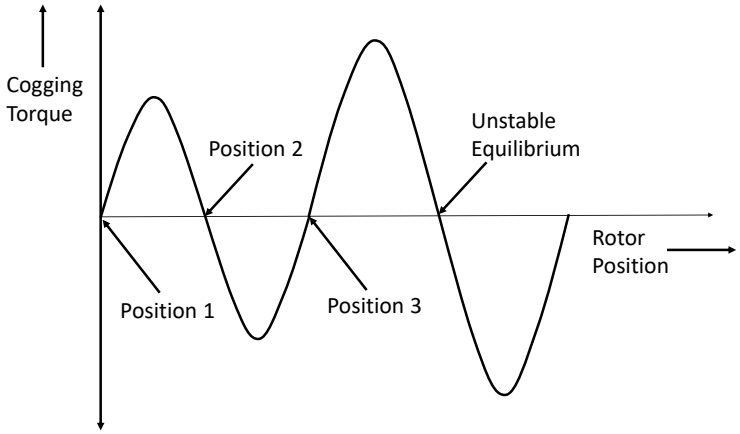

(b) Cogging torque waveform

Figure 4.7: Energy levels for position 1, 2 and 3, and the corresponding cogging torque waveform.

Moreover, when n=0, the flux avoids the parasitic gap for positions 1 and 3, leading to two peaks and a higher energy difference between the stable-unstable equilibrium positions.

It is worth mentioning that the flux splitting might happen in some other cases too, for example, when the number of poles per segment is 4/3, but it is not expected to be prominent for most machine designs because the entire half pole does not participate in facilitating flux splitting as it is present in the case discussed above.

4.3 Validation of the Proposed Theory of Cogging Torque Using FEA Simulations

In this section, the theory proposed in section 4.2.2 to determine the impact of segmentation is validated using the two example machines: machines A and B using FEA simulations. The results of the number of segments (N_s) that match the conditions proposed in theory for the two machines are discussed, and the parasitic gap length (g_p) is swept from 0 mm to 0.2 mm in steps of 0.05 mm as discussed in chapter 3.

4.3.1 Order of Cogging Torque Due to Pole-Slot Interaction and Pole-Parasitic Gap Interaction is Same

An example is discussed to illustrate the proposed concept using Machine B that has nine segments that satisfy the following:

$$\frac{2 \cdot N_s}{\mathrm{GCF}(2p, N_s)} = \frac{2 \cdot Z_s}{\mathrm{GCF}(2p, Z_s)} = 18 \tag{4.4}$$

As shown in Fig.4.8 that as the parasitic gap increases, the peak of the cogging torque decreases; this is due to increased cogging torque due to pole-parasitic gap interaction, which counters the pole-slot interaction as predicted by the proposed theory. It is worth noting

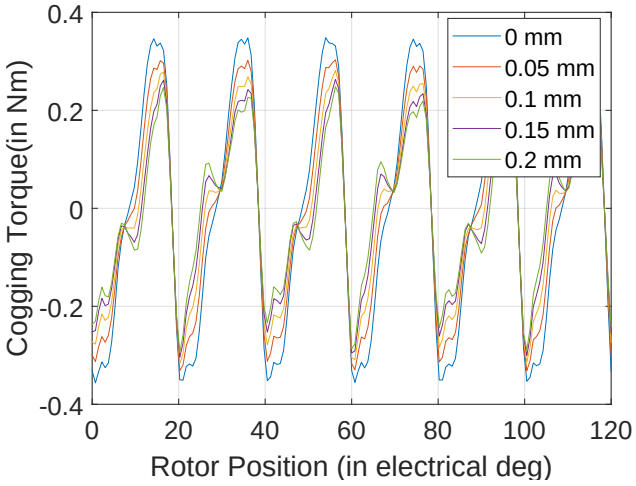

Figure 4.8: Variation of cogging torque with parasitic gap (g_p) for Machine B when $\frac{2 \cdot N_s}{\text{GCF}(2p, N_s)} = \frac{2 \cdot Z_s}{\text{GCF}(2p, Z_s)} = 18$ calculated using JMAG simulation software.

that there is a slight delay in the peak reduction of the cogging torque; this is because the peak does not appear when the edge of the magnet is along the slot opening as shown in [49].

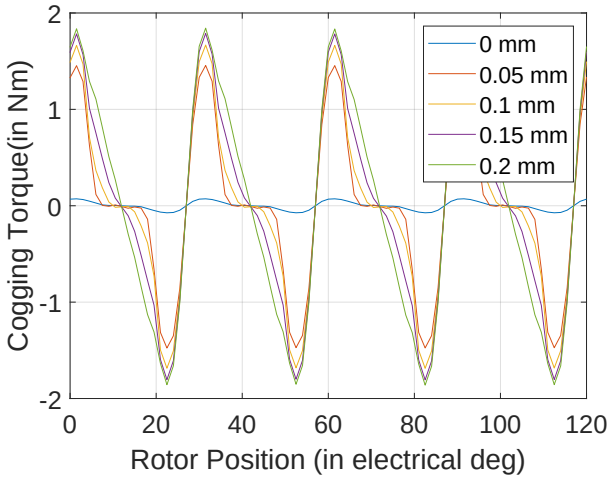

Figure 4.9: Variation of cogging torque with parasitic gap (g_p) for Machine A when $\frac{2 \cdot N_s}{\text{GCF}(2p, N_s)} = \frac{2 \cdot Z_s}{\text{GCF}(2p, Z_s)} = 12$ calculated using JMAG simulation software.

For machine A the following conditions is satisfied when $N_s = 72$:

$$\frac{2 \cdot N_s}{\text{GCF}(2p, N_s)} = \frac{2 \cdot Z_s}{\text{GCF}(2p, Z_s)} = 12 \tag{4.5}$$

As shown in Fig.4.4 the two cogging torques have an additive effect, which is also predicted by the proposed theory. The variation of cogging torque for machine A consisting of 72 segments is shown in Fig.4.9 where the cogging torque increases with an increase in parasitic gap.

4.3.2 Poles per Segment is/are an Integer

Fig.4.10 shows a significant increase in the peak to peak values of the cogging torque with the parasitic gap when the poles per segment is an integer for machines A and B, which is predicted from the proposed theory.

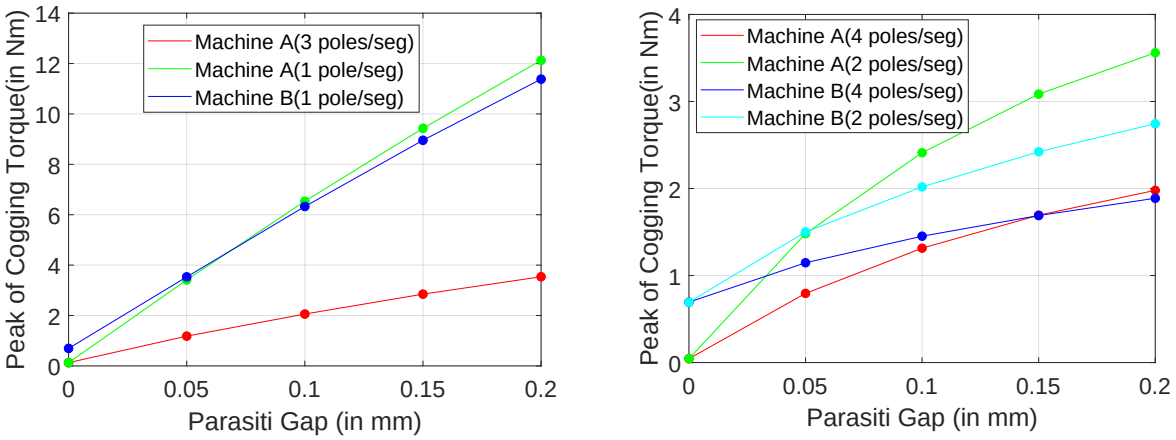

(a) Pole(s) per segment is(are) an odd number

(b) Poles per segment are an even number

Figure 4.10: Variation of the peak-to-peak value of the cogging torque with the parasitic gap (g_p) for machines A and B when the poles per segment is an integer calculated using JMAG simulation software.

Moreover, the peak-to-peak value of the cogging torque is considerably less when poles per segment are an even number, compared to when pole(s) per segment is/are an odd number, as explained earlier.

4.3.3 Poles per Segment is (2n+1/2)

The cogging torque waveform of machine A with eight segments, 3/2 poles per segment, and 24 segments, 1/2 poles per segment, is shown in Fig.4.11. As discussed in Fig.4.7, the positions are highlighted for both 8 and 24 segments machines, which is predicted from the proposed theory. It is worth noting that in one fundamental electrical cycle of the cogging torque, calculated from (4.2), there are two peaks because of the flux splitting.

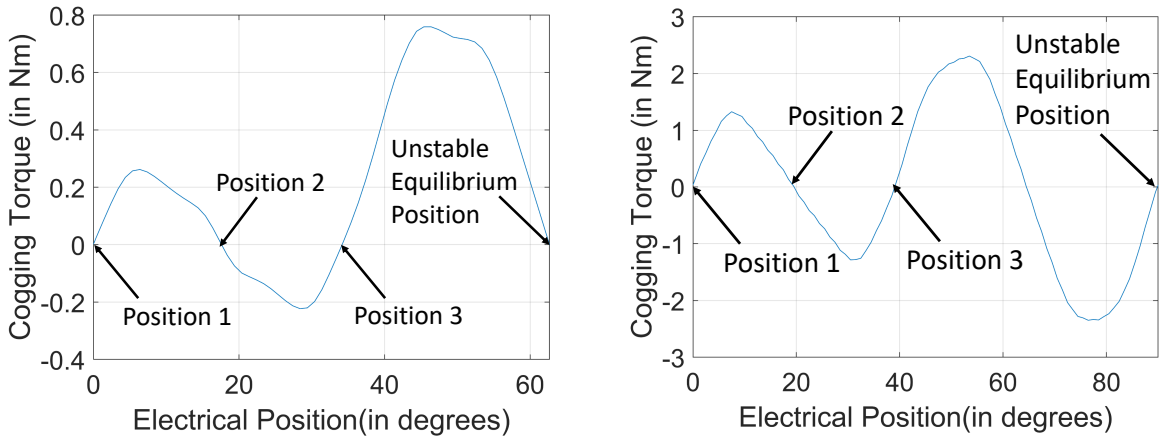

(a) 3/2 poles per segment

(b) 1/2 poles per segment

Figure 4.11: Cogging torque for machine A with poles per segment is (2n+1/2) with 0.2 mm parasitic gap for one fundamental cycle calculated using JMAG simulation software.

4.4 Back Electromotive Force in Segmented Stators

The conductors in the vicinity of the parasitic gap see a lower magnitude of flux cutting than the conductors well within the segment. If the segmentation is not performed symmetrically with respect to the conductors in each phase, it will be lead to unbalanced back electromotive force (BEMF).

Fig.4.12 shows one segment of machine A consisting of 3 segments. The pink and green conductors, corresponding to phases A and B, respectively, experience lower flux cutting and

lower BEMF in the presence of the non-zero parasitic gap. Moreover, the blue conductors, corresponding to phase C, experience higher values of flux cutting due to flux splitting, as shown in Fig.3.4.

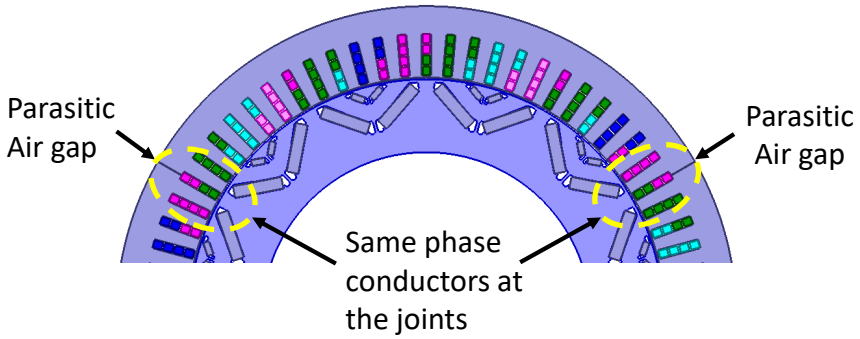

Figure 4.12: Pink and green conductors in the vicinity of the parasitic gap of Machine A consisting of 3 segments.

The variation of the fundamental component of the BEMF with the parasitic gap is shown in Fig.4.13 for machine A consisting of three segments supporting the claims made above.

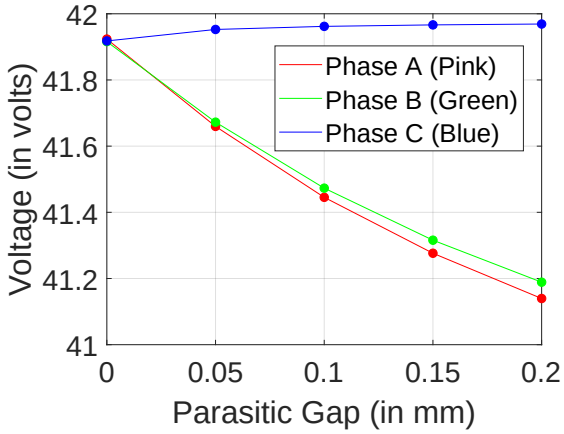

Figure 4.13: Variation of fundamental component of BEMF with parasitic gap for machine A with $N_s = 3$ calculated using JMAG simulation software.

In this section, the conditions to obtain balanced BEMF in an integral slot distributed winding machine are proposed and validated using FEA simulations.

4.4.1 Proposed Conditions for Balanced Back Electromotive Force

In this section, first the conditions for single layer integral slot distributed winding is proposed, followed by integral slot double layer winding. The flux linkage is equal for all the phases; each phase's same number of conductors should be placed along with the segmentation.

Simultaneously, the relative position of the conductor within one phase placed along with the segmentation should be maintained for all phases to maintain symmetry. An example for a machine consisting of three slots per pole per phase is shown in Fig.4.14.

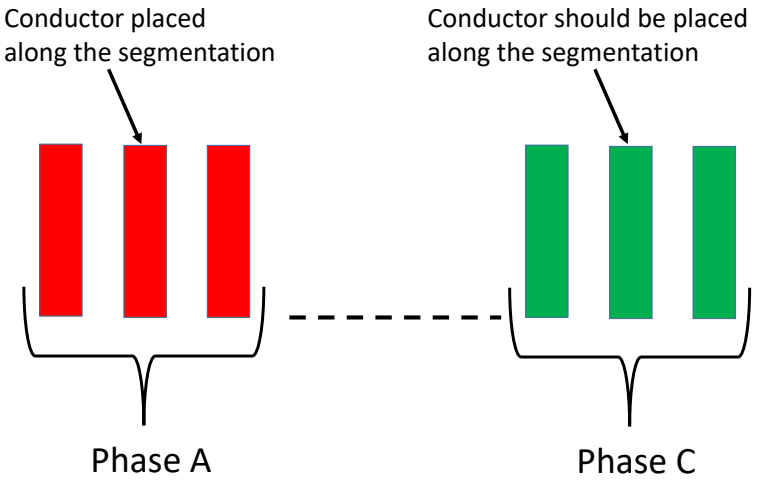

Figure 4.14: Relative position of the conductors along with the segmentation to maintain balanced BEMF in a machine with three slots per pole per phase with single layer winding.

The above conditions for the balanced BEMF are also applicable to the double layer integral slot distributed winding machine due to the symmetry.

4.4.2 Validating the Proposed Conditions for Balanced Back Electromotive Force Using FEA Simulations

Fig.4.15 shows the variation of the fundamental of the BEMF of Machines A and B with the parasitic gap for $N_s = 18$, that satisfy the conditions for balanced BEMF for both machines A and B, respectively validating the developed conditions.

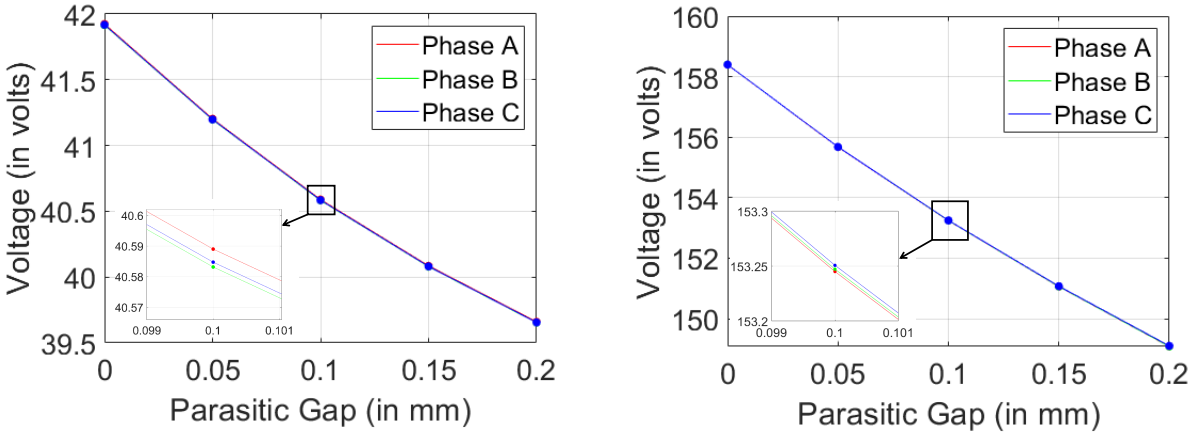

(a) Machine A with $N_s = 18$

(b) Machine B with $N_s = 18$

Figure 4.15: Variation of the fundamental of the BEMF with the parasitic gap for selected number of segments for machines A and B calculated using JMAG simulation software.

4.5 Conclusions

In this chapter, a general theory to determine the impact of segmentation parameters on the cogging torque is proposed, followed by the conditions to achieve balanced BEMF are proposed. The proposed theory states that the same electrical order for pole-slot interactions and pole-parasitic gap interactions may increase or decrease cogging torque. Further, integral or odd multiple of half poles per segment may lead to a considerably higher increase in cogging torque. The proposed conditions for the balanced BEMF are based on the symmetric placement of the conductors of each phase with respect to the segmentation. The proposed

theory and conditions are validated using two example machines of different designs using FEA simulations.

Chapter 5

Performance Comparison of the Oriented Steel Segmented Stator PMSM to the Conventional Machine

In this chapter, the utilization of BH and loss curves obtained from the analysis of experimental results in the piecewise isotropic model, discussed in chapter 2, are used to model an oriented-steel segmented stator. The oriented steel has the lowest core loss and highest permeability along the rolling direction, while the highest losses and lowest permeability along the 55° direction as shown in chapter 2. Therefore, building the whole stator with a single sheet of oriented steel will not properly utilize its magnetic properties. Therefore, a segmented-stator PMSM with different numbers of segments is used for analysis. The analysis is performed on Machine A, 12 poles/72 slots.

The performance of the anisotropic modular stator PMSM is compared with conventional non-oriented steel PMSM using the FEA simulations. The rolling direction has both higher permeability and lower losses compared to the non-oriented steel. Moreover, the non-oriented steel has slightly better permeability and lower losses than the oriented steel's transverse direction. The BH and loss curves in oriented and non-oriented steel are shown in Fig.5.1

First, the application of the theories, proposed and validated in chapters 3 and 4, on the

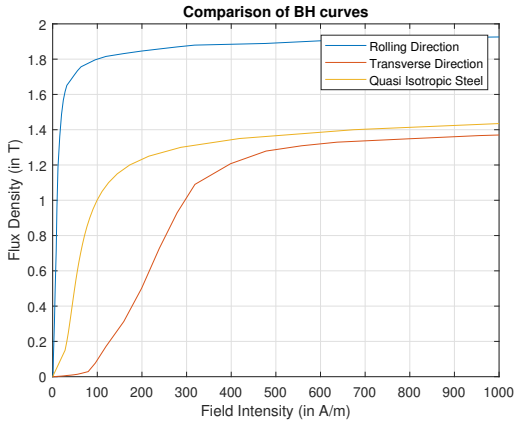

(a)

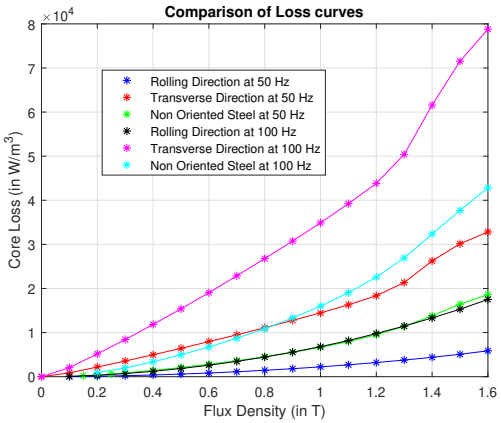

(b)

Figure 5.1: Comparison of the BH and core loss curves for the rolling, transverse direction and quasi-isotropic steel.

oriented steel segmented stator is discussed, along with the impact of using oriented steel on the machine's performance. After that, the comparison between the two models, consisting of modular oriented steel stator(A_{ori}) and non-oriented steel conventional stator($A_{conventional}$) that has the same geometry and design except that it has a conventional stator, is discussed. Total losses over a given drive cycle, cogging torque, and BEMF are compared for A_{ori} with the different number of segments and $A_{conventional}$.

5.1 Application of the Proposed Theory to Oriented Steel Segmented Stator PMSM

In this section, the performance of A_{ori} due to oriented steel, and segmentation parameters, proposed and validated in chapters 3 and 4, is studied. First, the observations are made under no-load conditions for the core loss and flux linkage, followed by the loaded conditions for flux linkage, core loss, and average loss. Finally, the discussion is extended to cogging torque and BEMF. The values of N_s used are: 3, 4, 6, 8, 9, 12, 18, 24, 36 and 72, while the

parasitic gap is swept from 0 mm to 0.2 mm in steps of 0.05 mm as discussed in chapters 3 and 4.

5.1.1 No Load Condition

5.1.1.1 Core Loss

The three teeth closest to the rolling direction have almost identical magnetic properties, approximately the same as the properties in the rolling direction. The core losses from the fourth teeth onward, i.e., more than 12.5° from the rolling direction, increase as shown in Fig.5.2.

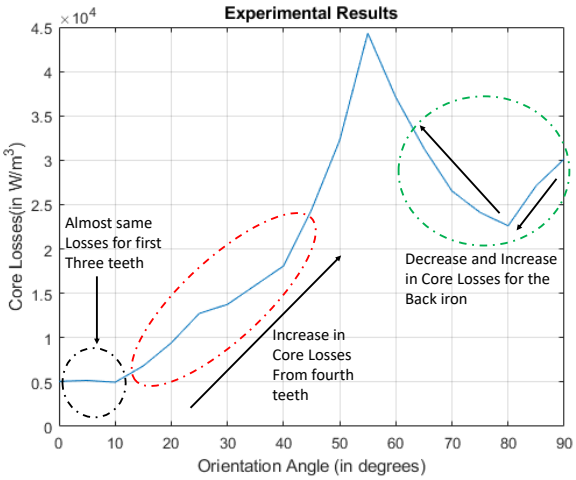

Figure 5.2: The variation of core losses with the orientation angle obtained from the analysis of experimental results at 1.5 T and supply frequency of 50 Hz that shows the core loss variation for the teeth and the back iron from the line of symmetry obtained from experiments as shown in Fig.2.19.

The core loss in the back iron decreases as the orientation angle changes from 90° to 80° and then increases as shown in Fig.5.2. Therefore, the back iron has the best properties for the first three divisions. Therefore, in each segment, when the number of teeth and back iron divisions is 6, which means $N_s = 12$, the segment has the best possible magnetic properties.

Fig.5.3 shows the variation of no-load core loss at 100 Hz electrical frequency. The minima occurs at $N_s = 12$ when parasitic gap is 0mm, while the core loss increases for $N_s = 3$ and $N_s = 6$ with the parasitic gap as shown in Fig.3.7 for machine A. Moreover, the decrease in the losses for higher values of N_S with increased parasitic is due to overall decrease in flux.

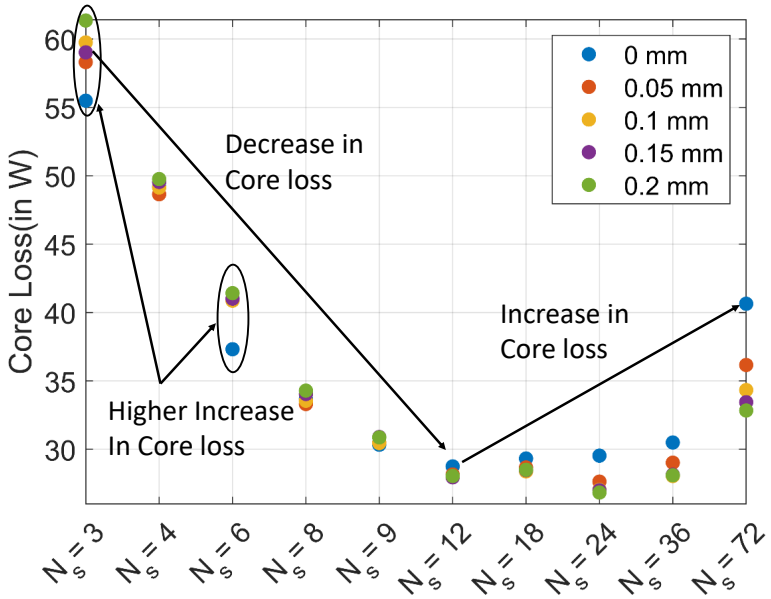

Figure 5.3: No load core loss variation with the number of segments(N_s) and parasitic gaps (g_p) for A_{ori} of the complete stator at 100 Hz of electrical frequency calculated using JMAG simulation software.

5.1.1.2 Flux Linkage from the Magnets(λ_{pm})

The decrease in λ_{pm} with parasitic gap is higher for $N_s = 3$ (4 poles per segment), and $N_s = 6$ (2 poles per segment) compared to $N_s = 4$ and $N_s = 8$ respectively, due to local saturation, explained in section 3.1, as shown in Fig.5.4. Moreover, with increase in number of segments the decrease in λ_{pm} is significantly higher due to higher parasitic gap.

Moreover, when the number of segments is 12, the permeability from A_{ori} stator is maximum; this is because the lower core losses and higher permeability variation are the

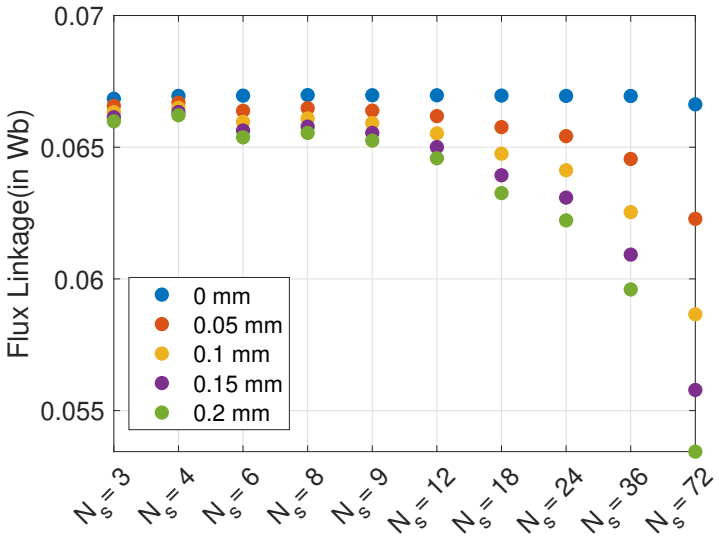

Figure 5.4: λ_{pm} variation with the number of segments(N_s) and parasitic gaps (g_p) for A_{ori} calculated using JMAG simulation software.

same for the same orientation directions. Therefore, both the lowest losses, as discussed in section 2.5, and highest permeability is from the A_{ori} machine with 12 segments. The change in the λ_{pm} is very small, no-load d-axis flux, as explained in section 3.2. Therefore, the material improvement barely affects the value of λ_{pm}. Moreover, this change due to improved quality of steel is overshadowed by the parasitic gaps, especially at the higher number of segments. Fig.5.5 shows the variation of λ_{pm} with the number of segments for A_{ori} at 0 and 0.2 mm parasitic gap.

From the above discussion, it is inferred that the maximum permeability, and hence the highest value of λ_{pm}, is $N_s = 12$ when the parasitic gap is 0 mm. Moreover, when the value of the parasitic gap is 0.2 mm, the increase in λ_{pm} is entirely overshadowed by the higher reluctance of the parasitic gaps.

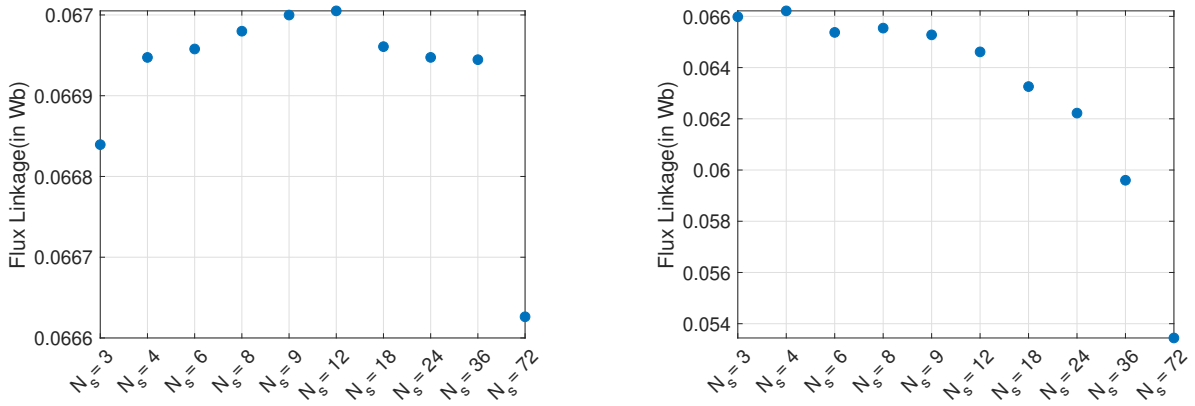

(a) Parasitic gap 0 mm

(b) Parasitic gap 0.2 mm

Figure 5.5: Variation of λ_{pm} for A_{ori} with the number of segments(N_s) with parasitic gap of 0 and 0.2 mm calculated using JMAG simulation software.

5.1.2 Loaded Condition

The study for A_{ori} under loaded conditions is carried out at O, which is used in section 3.5.

5.1.2.1 d-axis flux linkage (λ_d) and q-axis flux linkage (λ_q)

Similar to λ_{pm}, the decrease in λ_d and λ_q with parasitic gap is higher for $N_s = 3$ (4 poles per segment), and $N_s = 6$ (2 poles per segment) compared to $N_s = 4$ and $N_s = 8$ respectively, due to local saturation, explained section 3.1, as shown in Fig.5.6. Moreover, the change in the q-axis flux linkage is larger compared with the d-axis flux linkage as highlighted for $N_s = 12$ in Fig.5.6.

Similarly, the highest value of both λ_d and λ_q is at $N_s = 12$ when the parasitic gap is 0 mm. Moreover, when the value of the parasitic gap is 0.2 mm, the increase is entirely overshadowed by the higher reluctance of the parasitic gaps. Figs.5.7 and 5.8 shows the variation of λ_d and λ_q for 0 and 0.2 mm parasitic gaps.

The above discussion, which is consistent with proposed theory in section 3.2, is summa-

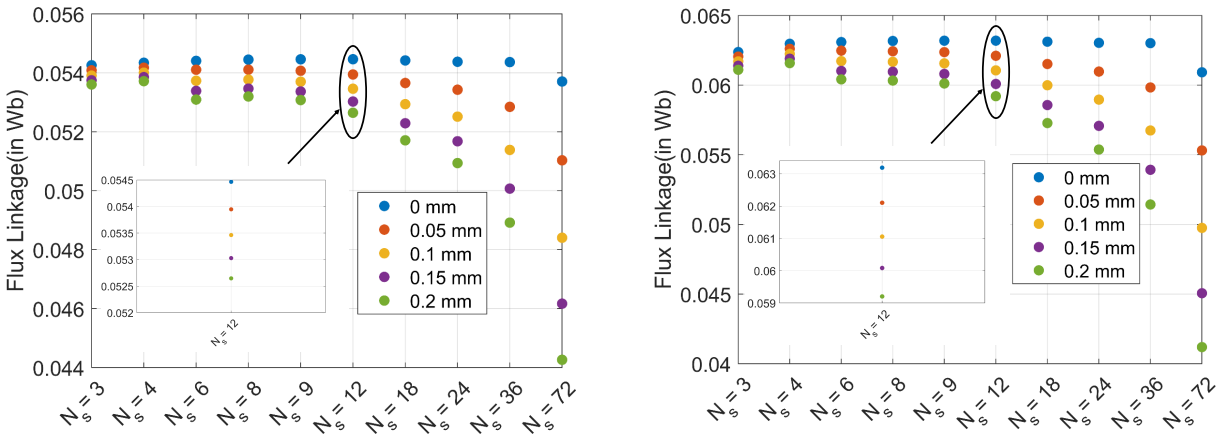

(a) λ_d variation (b) λ_q variation

Figure 5.6: Variation of λ_d and λ_q with the number of segments(N_s) and parasitic gaps (g_p) for A_{ori} calculated using JMAG simulation software.

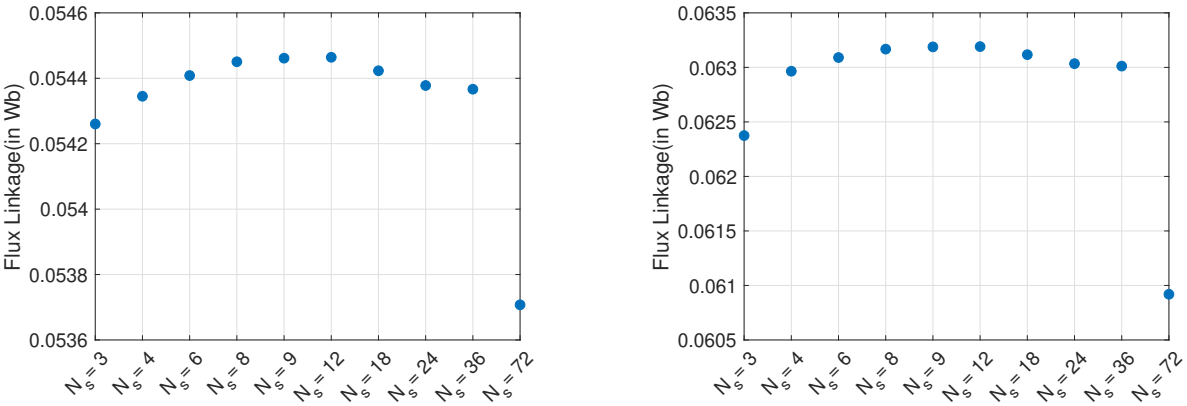

(a) λ_d variation (b) λ_q variation

Figure 5.7: Variation of λ_d and λ_q for machine A with the number of segments(N_s) at point O for the parasitic gap of 0 mm calculated using JMAG simulation software.

rized as:

1. The presence of parasitic gaps in the segmented stator leads to the decrease in λ_d and λ_q.

2. The decrease in λ_q with parasitic gaps is more prominent than λ_d.

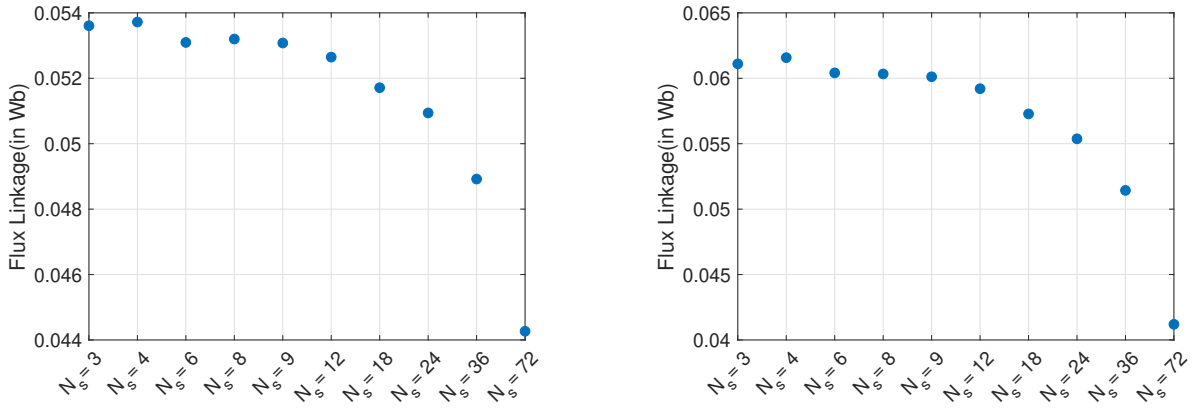

(a) λ_d variation (b) λ_q variation

Figure 5.8: Variation of λ_d and λ_q for machine A with the number of segments(N_s) at point O for the parasitic gap of 0.2 mm calculated using JMAG simulation software.

5.1.2.2 Core Loss

The variation similar to shown in Fig.5.3 of core loss is observed for A_{ori} machine under loaded conditions for the parasitic gap of 0 mm; this is because the teeth back iron has the lowest possible losses at all saturation levels when the number of segments is 12. However, the core losses also decrease due to a higher decrease in flux at higher N_s.

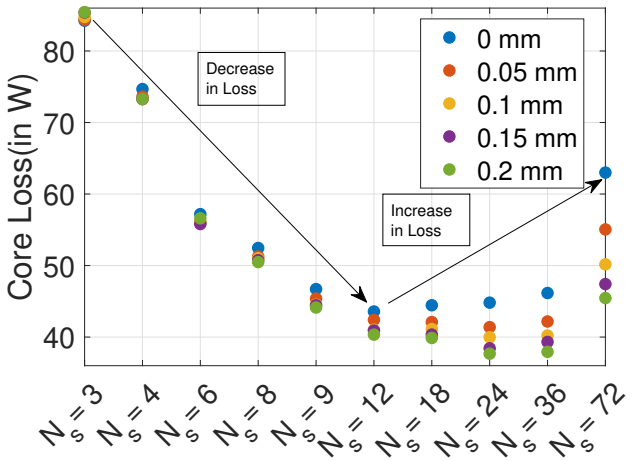

Figure 5.9: Core loss variation with the number of segments(N_s) and parasitic gaps (g_p) for A_{ori} of the complete stator at point O calculated using JMAG simulation software.

However, for $N_s = 3$, core loss increases with g_p even with a net decrease in λ_d, and λ_q as shown in Fig.5.6(a) is due to local saturation. On the other hand, for $N_s = 6$, the decrease in overall flux is higher than $N_s = 6$ because of more parasitic gaps, and hence losses first decrease then start to increase with the parasitic gap as shown in Fig..5.6(b). It is worth mentioning here that in the case of the no-load condition, the losses increase for $N_s = 6$ but under the loaded condition, the losses first decrease, and then increase; this is due to a higher decrease in the λ_q compared to λ_{pm}, which is essentially no-load λ_d.

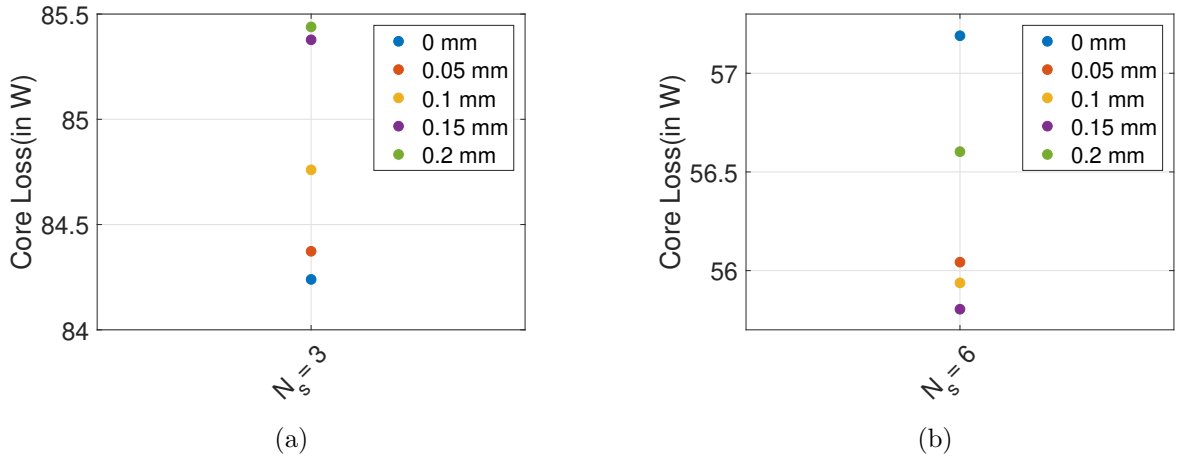

Figure 5.10: Core loss variation with the parasitic gaps (g_p) for A_{ori} of the complete stator at point O for 3 and 6 segments calculated using JMAG simulation software.

5.1.2.3 Average Torque

As discussed in section 3.5.3, for the same values of i_d and i_q, the variation of the average torque, as shown in Fig.5.11, is similar to the variation of λ_d and λ_q as shown Fig.5.6.

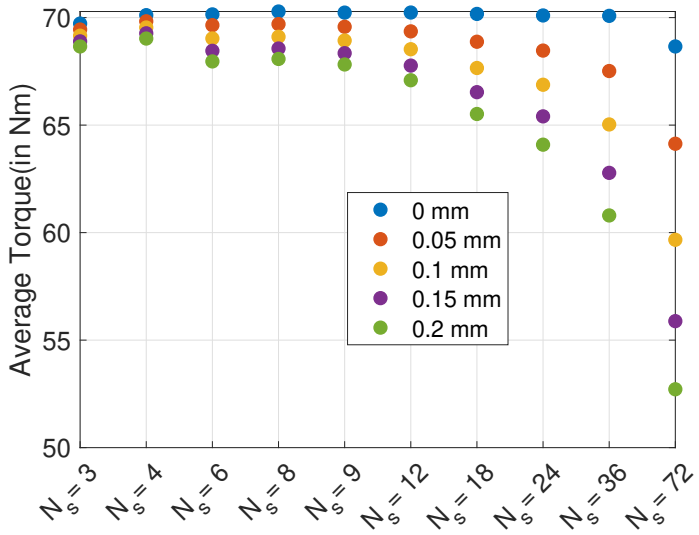

Figure 5.11: Average Torque variation with the number of segments(N_s) and parasitic gaps (g_p) for A_{ori} of the complete stator at point O calculated using JMAG simulation software.

5.1.3 Variation of Cogging Torque and BEMF in Oriented Steel Segmented Stator PMSM

The change in steel from non-oriented to oriented steel is not likely to change the d-axis flux significantly, as discussed in section 3.2. This can be shown by comparing the no-load d-axis flux linkage, λ_{pm}, between oriented and non-oriented steel segmented stator. Fig.5.12 shows the λ_{pm} comparison between oriented and non-oriented steel segmented stator at the parasitic gap at 0 mm, which shows a maximum change at $N_s = 12$ which is only 0.45%.

Moreover, the air gap flux density, at stable and unstable equilibrium conditions, is almost similar, as shown in Fig.5.13 for oriented and non-oriented steel segmented stator PMSM at 0.2 mm parasitic gap; this is because of change in reluctance due to the parasitic gaps is more significant than the change in the reluctance due to steel. Moreover, the balanced BEMF depends on the symmetric placement of the conductors.

Therefore, the impact of segmentation parameters on cogging torque and BEMF proposed

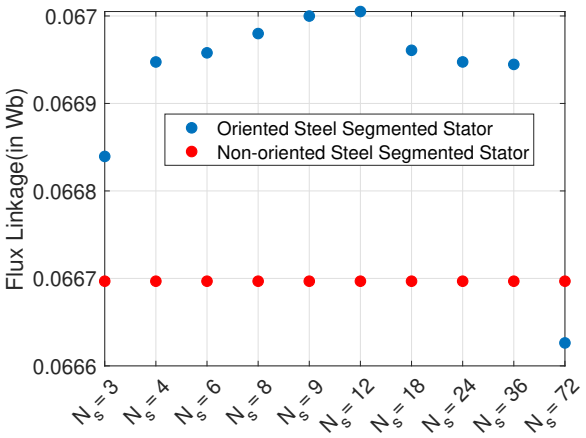

Figure 5.12: λ_{pm} variation with the number of segments(N_s) for oriented and non-oriented steel segmented stator PMSM at 0 mm parasitic gap calculated using JMAG simulation software.

and validated in chapter 4 for the cogging torque and BEMF in the segmented stator is also applicable for the A_{ori}.

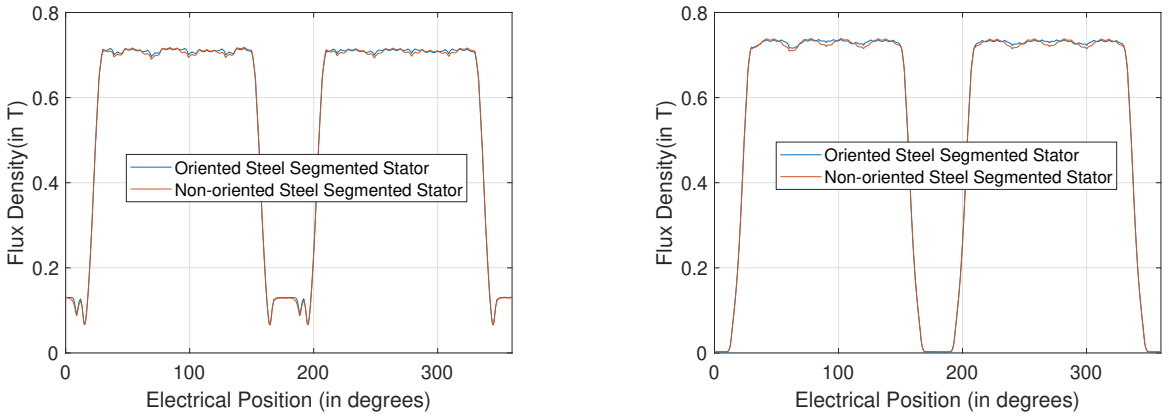

(a) Stable Equilibrium Position

(b) Unstable Equilibrium Position

Figure 5.13: Air gap flux density variation for, stable and unstable equilibrium positions, at $N_s = 12$ for oriented and non-oriented steel segmented stator PMSM at 0.2 mm parasitic gap calculated using JMAG simulation software.

Fig.5.14 shows the variation of peak-peak cogging torque, and fundamental of BEMF with the parasitic gaps, at $N_s = 12$ and $N_s = 18$ respectively, for oriented steel and non oriented steel segmented stator PMSM. The variation for cogging torque is almost similar

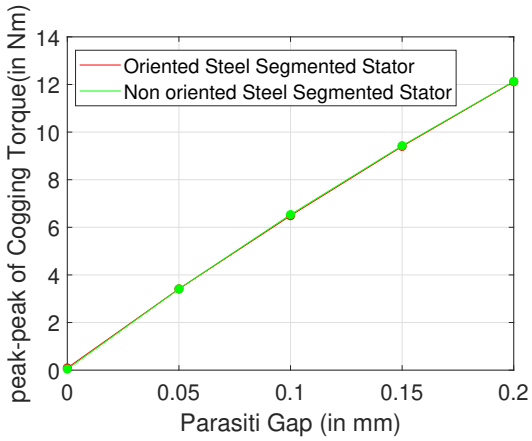

(a) Peak-peak cogging torque at $N_s = 12$

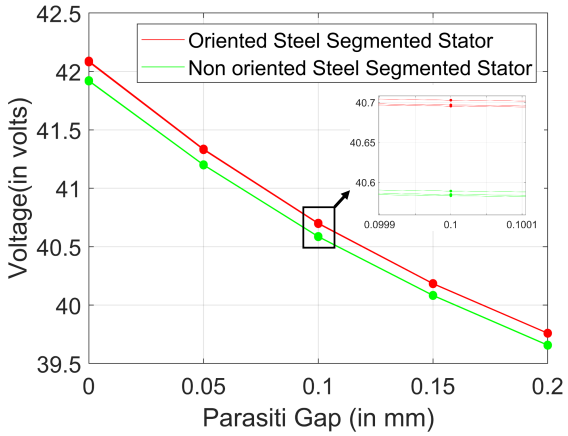

(b) Fundamental BEMF at $N_s = 18$

Figure 5.14: Cogging torque and fundamental of BEMF variation with the parasitic gap for oriented and non-oriented steel segmented stator PMSM calculated using JMAG simulation software.

with almost similar peak-peak value, while BEMF has slightly higher value but the still balanced operation.

5.2 Performance Comparison of the A_{ori} and $A_{conventional}$

In this section, the performance of the A_{ori} and $A_{conventional}$ is compared. First is a comparison between the flux linkage, core loss, and average torque at point O. Further, the comparison is performed at a drive cycle, which is the standard testing procedure. After that, the comparison between cogging torque and imbalance in BEMF is performed. Finally, the total loss from the drive cycle, cogging torque, and imbalance in BEMF are compared.

5.2.1 Comparison Under Loaded Conditions at Point O

5.2.1.1 d-axis flux linkage (λ_d) and q-axis flux linkage (λ_q)

Fig.5.15 shows the variation of λ_d and λ_q at point O for A_{ori} with the number of segments for the parasitic gap of 0 mm. As proposed in section 3.2 the change in the value of λ_q with

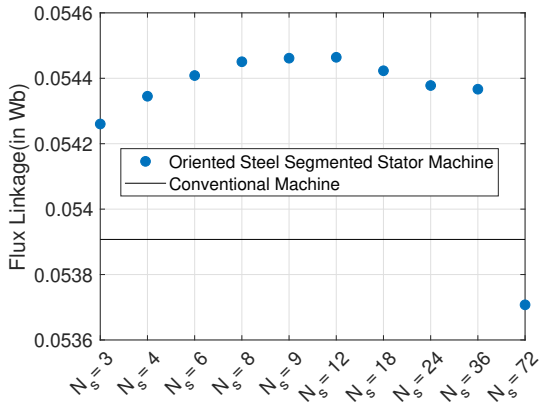

(a) λ_d variation

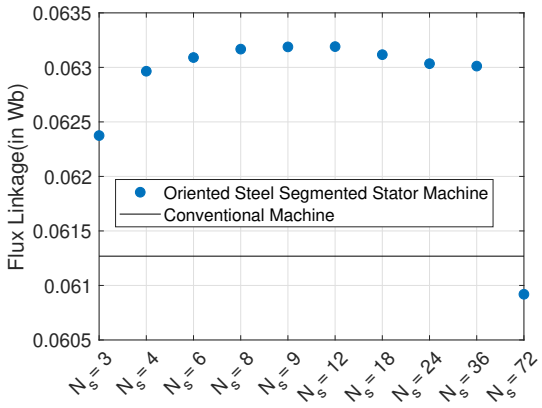

(b) λ_q variation

Figure 5.15: Variation of λ_d and λ_q for A_{ori} with $A_{conventional}$ at point O for the parasitic gap of 0 mm calculated using JMAG simulation software.

change in material from non oriented steel to oriented steel is more prominent compared to λ_d. For example: the percentage increase in the values of λ_d and λ_q from $A_{conventional}$ machine to A_{ori} machine for $N_s = 12$ are 0.93% and 3.27% respectively. Moreover, for all segments of A_{ori}, except 72, both λ_d and λ_q are higher than the conventional machine.

Fig.5.16 shows the variation of λ_d and λ_q at point O for A_{ori} machine when the parasitic gap is 0.2 mm. The increased flux linkage due to improved steel quality is entirely dominated by the parasitic gap except for λ_q when $N_s = 4$.

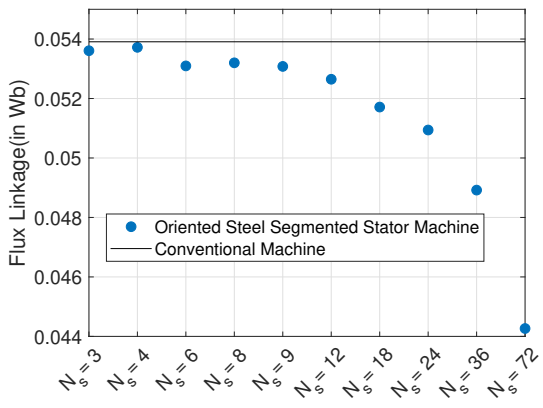

(a) λ_d variation

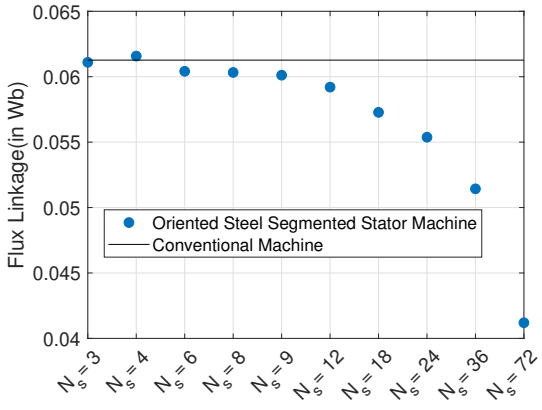

(b) λ_q variation

Figure 5.16: Variation of λ_d and λ_q for A_{ori} with $A_{conventional}$ at point O for the parasitic gap of 0.2 mm calculated using JMAG simulation software.

5.2.1.2 Core Loss

Due to the superior magnetic properties of the teeth of the A_{ori}, the losses are lower compared to $A_{conventional}$ when N_s is 12, 18, and 24 when the parasitic gap is 0 mm. Moreover, as the parasitic gap increases, the core loss of N_s as 9 and 36 decreases below the conventional machine. However, this decrease is due to the decrease in overall flux in the machine. Therefore, the losses are expected to be higher for the same levels of flux with the increase in parasitic gap. Fig.5.17 shows the variation of core loss with number of segments for A_{ori} and $A_{conventional}$.

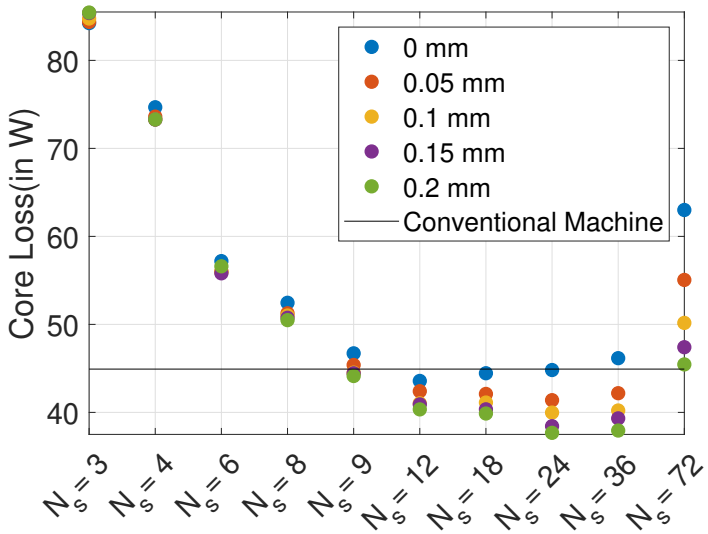

Figure 5.17: Core loss variation with the number of segments(N_s) and parasitic gaps (g_p) for A_{ori} with $A_{conventional}$ at point O

5.2.1.3 Average Torque

The average torque of A_{ori} is higher for all segments, except 72, compared to $A_{conventional}$ when the parasitic gap is 0 mm. Moreover, the average torque is lower for all segments of A_{ori}, except 4, compared to $A_{conventional}$ when the parasitic gap is 0.2 mm; this is due to

higher λ_q that compensates for lower λ_d as shown in Fig.5.16. Fig.5.18 shows the variation of average torque for A_{ori} and $A_{conventional}$ at 0 and 0.2 mm parasitic gap.

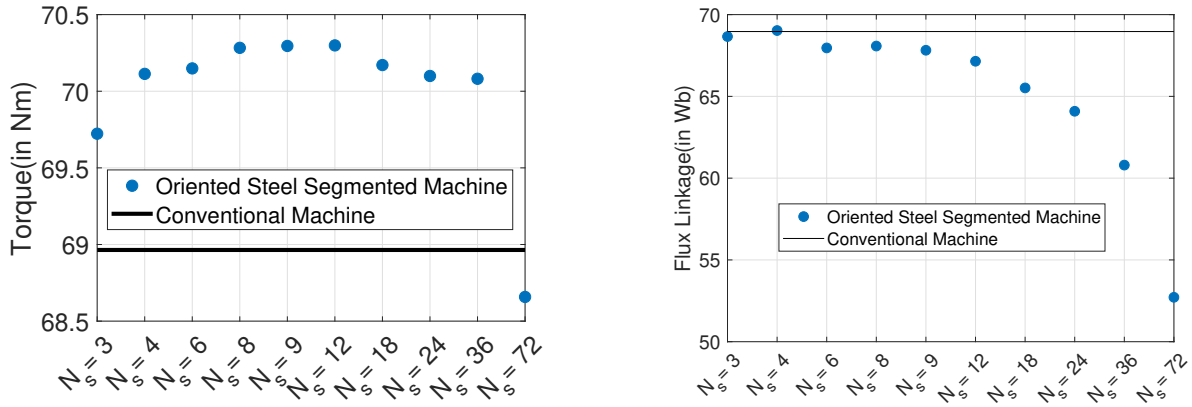

(a) 0 mm (b) 0.2 mm

Figure 5.18: Variation of Average Torque for A_{ori} with $A_{conventional}$ at point O for the parasitic gaps of 0 and 0.2 mm calculated using JMAG simulation software.

5.2.2 Comparison Over a Drive Cycle

The performance of the oriented steel segmented stator PMSM (A_{ori}) is compared with the conventional stator PMSM ($A_{conventional}$) at one operating point, as shown in Fig.5.2.1. However, at different loads and frequencies the performance might vary. Therefore, the comparison is performed at a selected drive cycle, and the selected performance parameter is the total loss. Stator segmentation, with non-zero parasitic gaps, decreases the average torque for the same values of currents. Therefore, to achieve the same average torque, a higher current is injected in the segmented stator machine than the conventional machine. Therefore, it leads to an increase in both core loss and copper loss.

The drive cycle that is used for comparison is the federal test procedure shown in [50]. The corresponding operating points are calculated using the equations presented in [51], and motor parameters and EV parameters are given in Table. 5.1.

S. No.	Parameter	Value
1	Motor Base Speed	3000 RPM
2	Motor Rated Torque	290 Nm
3	Vehicle Gross Weight	2079 Kg
4	Vehicle Drag Coefficient	0.28
5	Tyre Rolling Coefficient	0.008
6	Tyre Radius	0.32 m
7	Vehicle frontal Area	2 m^2
8	Vehicle Transmission Efficiency	0.9
9	Vehicle Gear Ratio	2.64
10	Slip	0.08
11	Slope	0 deg

Table 5.1: Machine and vehicle parameters

Fig.5.19 shows the variation of the total losses in the drive cycle of the A_{ori} with N_s and g_p, and the conventional machine. At 0 mm the A_{ori} with 8, 9, 12, 18, 24 and 36 segments has lower losses compared to $A_{conventional}$. The total losses for all segmentation increase with an increase in the parasitic gaps, and for $g_p = 0.1$ mm, all segments have higher losses compared to $A_{conventional}$. The parasitic gap is limited to 0.1 mm for this discussion as total losses increase beyond that. Moreover, the increase in loss for $N_s = 3$, and $N_s = 6$ is more rapid compared to $N_s = 4$ and $N_s = 8$ respectively due to local saturation, while for higher N_s, 24, 36 and 72, the increase is due to higher parasitic gaps.

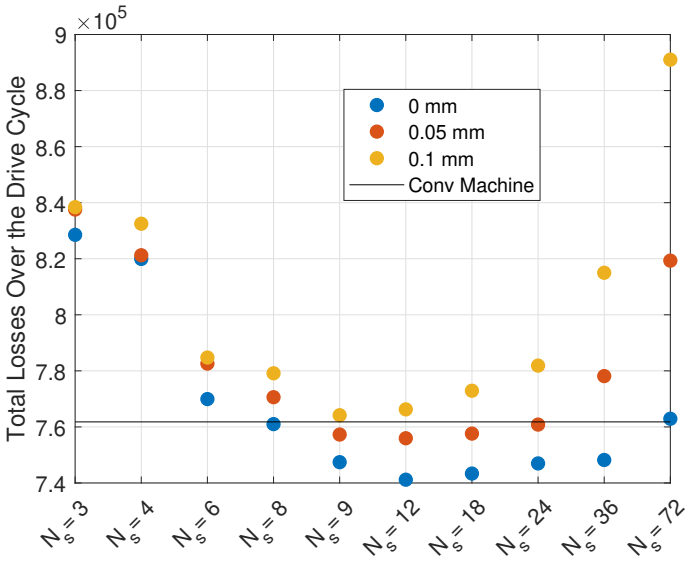

inin

Figure 5.19: Variation of total loss over a drive cycle with the number of segments (N_s) and parasitic gap (g_p) for A_{ori} with $A_{conventional}$ calculated using JMAG simulation software.

5.2.3 Comparison of Cogging Torque and BEMF

The cogging torque increase, with the parasitic gap, for all segmentation of A_{ori}, compared with $A_{conventional}$. The maximum increase for $N_s = 12$, pole per segments is 1, while minimum is for $N_s = 9$. Moreover, when pole(s) per segment is(are) an integer, the peak-peak value increases with lower poles per segment as more pole pairs transition from stable to unstable equilibrium positions. Similar trend is shown by $N_s = 8$ and $N_s = 24$, where poles per segment 1.5 and 0.5 respectively. Finally, for $N_s = 72$, the order of two cogging torques has the same order and additive effect, hence an overall net increase. Fig.5.20 shows the variation of peak-peak values of cogging torque with the number of segments for A_{ori} with $A_{conventional}$.

The imbalance in the BEMF is shown as:

$$\%\text{Imbalance in BEMF} = \frac{\text{Max fund}_{ABC} - \text{Min fund}_{ABC}}{\text{Max fund}_{ABC}} \cdot 100 \tag{5.1}$$

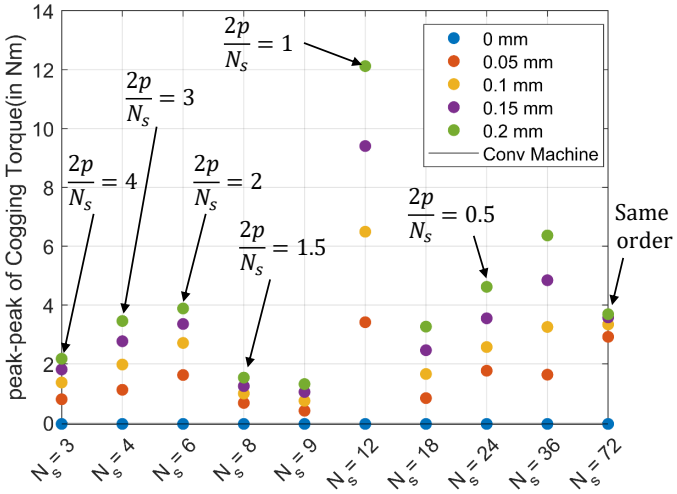

Figure 5.20: Peak-peak cogging torque variation with the number of segments(N_s) and parasitic gaps (g_p) for A_{ori} with $A_{conventional}$ calculated using JMAG simulation software.

where Max fund$_{ABC}$ and Min fund$_{ABC}$ are the maximum and minimum values of the peak of the fundamental of the three phases, respectively.

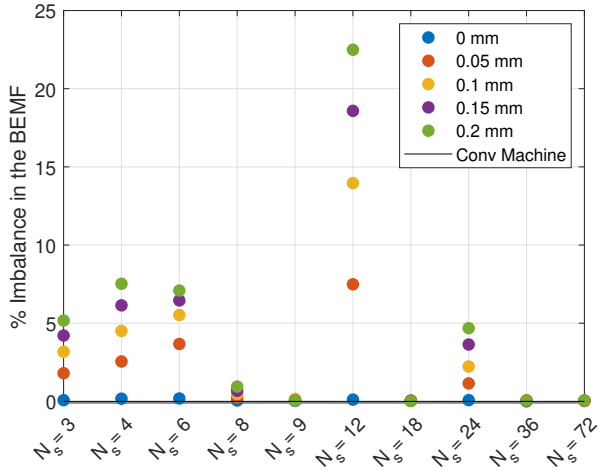

Figure 5.21: Imbalance in BEMF variation with the number of segments(N_s) and parasitic gaps (g_p) for A_{ori} with $A_{conventional}$ calculated using JMAG simulation software.

Fig.5.21 shows the variation of imbalance in the BEMF with the number of segments for A_{ori} with $A_{conventional}$, which shows imbalance increases with an increase in parasitic gap. Moreover, no imbalance is shown when N_s is 9, 18, 36, and 72, while the maximum

imbalance is shown by 12.

5.2.4 Summary of Comparison between A_{ori} and $A_{conventional}$

The percentage change of total loss over the drive cycle is defined as:

$$\% \text{ Change in total loss} = \frac{\text{Conventional Machine} - \text{Oriented Steel Machine}}{\text{Conventional Machine}} \cdot 100 \qquad (5.2)$$

Change in total loss over a drive cycle, cogging torque, and imbalance in the BEMF for all the segments, and parasitic gaps up to 0.1 mm is summarized in Table.5.2.

	% Change in Total Loss			Peak-peak Cogging Torque (in Nm)			% Imbalance in BEMF		
N_S	g_p=0 mm	g_p=0.05 mm	g_p=0.1 mm	g_p=0 mm	g_p=0.05 mm	g_p=0.1 mm	g_p=0 mm	g_p=0.05 mm	g_p=0.1 mm
3	-8.7609	-9.9440	-10.0579	0.0222	0.7943	1.3657	0	1.8018	3.1721
4	-7.6315	-7.8043	-9.2805	0.0222	1.1172	1.9753	0	2.5518	4.5070
6	-1.0687	-2.730	-3.0130	0.0222	1.6194	2.7095	0	3.6721	5.5268
8	0.1043	-1.1560	-2.2762	0.0222	0.6706	0.9907	0	0.2322	0.4691
9	1.8873	0.5922	-0.3125	0.0222	0.4052	0.7424	0	0	0
12	2.7075	0.7665	-0.5863	0.0222	3.4134	6.4892	0	7.4882	13.9625
18	2.4202	0.5482	-1.4592	0.0222	0.8340	1.6537	0	0	0
24	1.9451	0.1263	-2.6354	0.0222	1.7658	2.5697	0	1.1498	2.2297
36	1.7839	-2.1449	-6.9840	0.0222	1.6306	3.2524	0	0	0
72	-0.1462	-7.5516	-16.9637	0.0222	2.9176	3.3380	0	0	0

Table 5.2: Summary of the comparison between A_{ori} and $A_{conventional}$ calculated using JMAG simulation software.

5.3 Conclusions

In this chapter first the developed theory in chapters 3 and 4 is applied in A_{ori}. After that, performance of A_{ori} and $A_{conventional}$ is compared, and it is shown that A_{ori} has lower total losses over a drive cycle than the $A_{conventional}$ when N_s is 8, 9, 12, 24 and 36 at 0 mm parasitic gap. Moreover, with an increase in the parasitic gap, the total losses for A_{ori} increase and eventually become higher for all values of N_s when the parasitic gap is 0.1 mm. Moreover, cogging torque increases with the parasitic gap for all segments, while the imbalance in BEMF increases for 3, 4, 6, 8, 12 and 24.

Chapter 6

Conclusions and Future Work

In this work, a general method to estimate the magnetic properties of the oriented steel is proposed. The method requires specially designed devices, an experimental setup, a power supply of controlled amplitude and frequency power supply, and measuring instrumentation. The method is comparatively less expensive than the Epstein frame test. Further, a general theory to determine the impact of segmentation parameters on the selected performance parameters: core loss, average torque, cogging torque, and BEMF is discussed.

First, the proposed method to estimate the magnetic properties of the oriented steel is applied using an oriented steel segmented stator with four segments and 72 teeth, along with three devices of different spans. The experimentally estimated magnetic characteristics of the oriented steel are different from the FEA method based on the properties of rolling and transverse direction to interpolate the magnetic characteristics. Instead, the developed method determines the characteristics of the steel for different orientations, frequencies, and flux densities.

Further, the impact of segmentation parameters on the machine's performance is validated using numerical experiments using two machines with 72 slots/12 poles and 72 slots/8 poles. Finally, the obtained magnetic characteristics of the oriented steel are used to model the segmented stator machine, where the orientation is in the direction of teeth, and the oriented-steel segmented stator is compared to conventional non-oriented steel stator PMSM

with 72 slots and 12 poles.

The total losses for the conventional machine and various combinations of segment size and parasitic gaps of oriented steel machine were compared at the federal test procedure drive cycle, and it is observed that the oriented steel machine has lower total losses when the number of segments is 8, 9, 12, 18, 24, and 36 at the parasitic gap of 0 mm. Moreover, the machine with 12 segments has the lowest losses. Further, with the increase in the parasitic gap, the oriented steel has higher losses than conventional machine due to increased current requirements for the same average torque. Finally, the comparison of cogging torque shows that the oriented steel has higher cogging torque for all nonzero parasitic gaps for all segments, while the BEMF is imbalanced for 3, 4, 6, 8, 12, and 24.

Future work includes modeling increased cut edges to find the impact on the increased core losses and decreased permeability. Further, the analysis of the non-uniform gaps will be performed, followed by analyzing the impact of segmentation on torque ripple, radial forces, and eddy current losses. Finally, a new topology of segmentation and design modification of the original stator will be performed to optimize the machine's performance.

APPENDICES

Appendix A

Accuracy of the Model Proposed in [40] for Oriented Steel Stator Modeling

This section determines the accuracy of the piecewise isotropic model for modeling anisotropic steel segmented stator. Oriented steel stator was modeled in FEA using piecewise isotropic steel segments [40], and based on the direction of flux, the magnetic characteristics of the isotropic material were selected as shown in section 1.3.6.2. Modeling the tooth and the back iron between the adjacent teeth is straightforward as the flux direction is clearly defined. However, modeling the region where teeth meet the back iron is challenging as the flux bends in this region. The direction of flux is ambiguous, as shown in Fig.A.1.

The extension of the material used to model the tooth is used for modeling the region where teeth meet the back iron as discussed in section 1.3.6.2. The model was not verified with the machine with the higher number of teeth, e.g., 72 teeth in [40]. The incorrect modeling of back iron where flux bends may cause significant error in the estimation of machine performance. Hence, the proposed model discussed in section 1.3.6.2 was verified with 12-pole/72-slot IPMSM, Machine-A, made of four segments with each segment is oriented in the direction of teeth. The machine model used for analysis is shown in Fig.A.2 where a 0.2

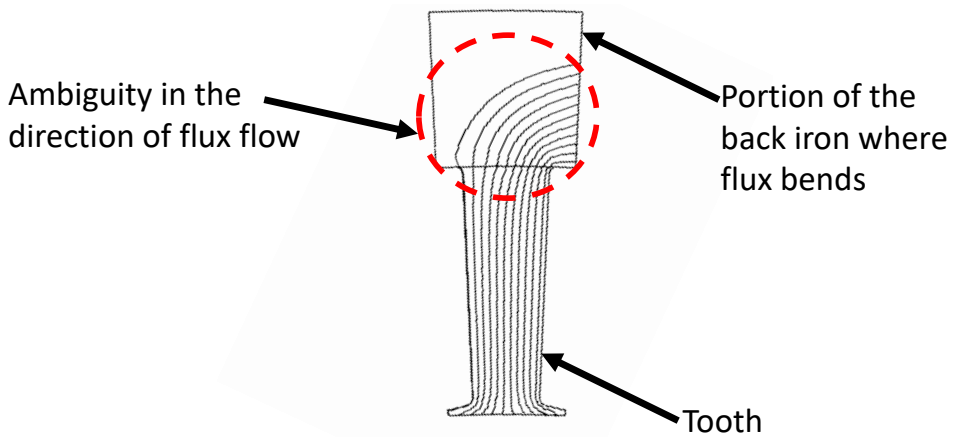

Figure A.1: Ambiguity in the direction of flux in the region where teeth meets the back iron

mm air gap is used between the segments in simulations. All the simulations were performed in JMAG FEA software.

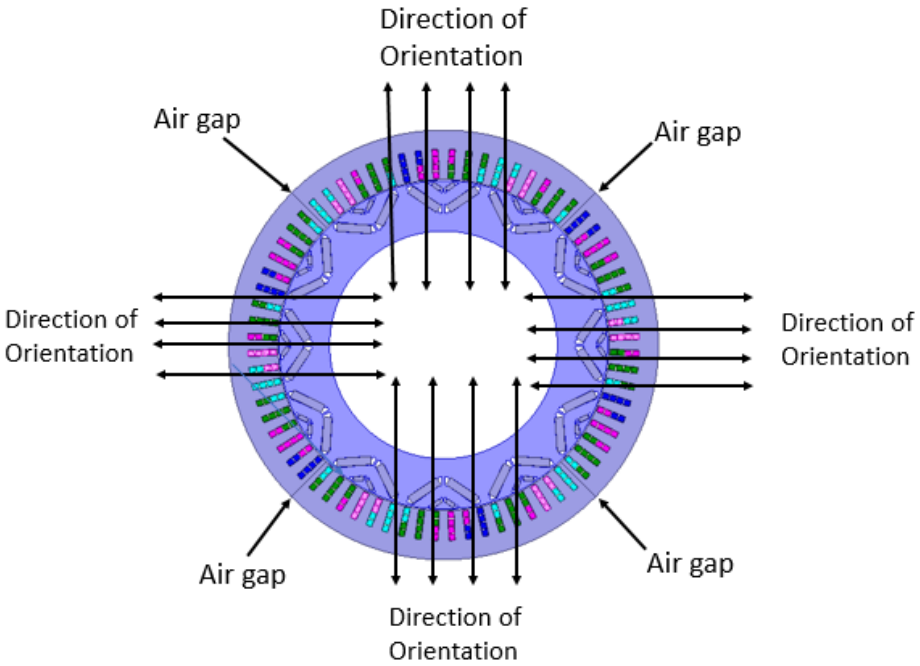

Figure A.2: Machine A model with four segments with orientation in direction of teeth

One of the four segments with orientation direction of the steel is shown in Fig.A.3.

The selection of the piecewise isotropic model is motivated from [40] which is discussed

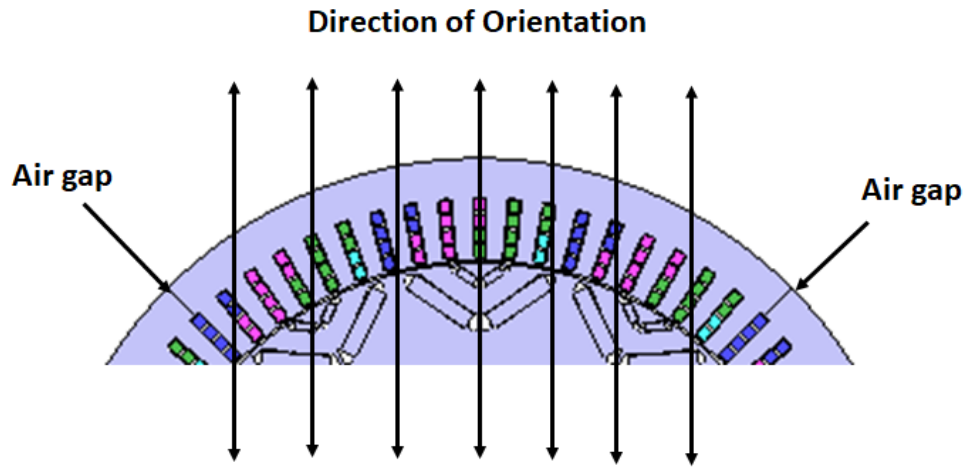

Figure A.3: One section of the anisotropic steel of the machine with orientation direction

in section 1.3.6.2. One of the four sections of the piecewise isotropic model selected for 12 poles and 72 slots IPMSM is shown in Fig.A.4.

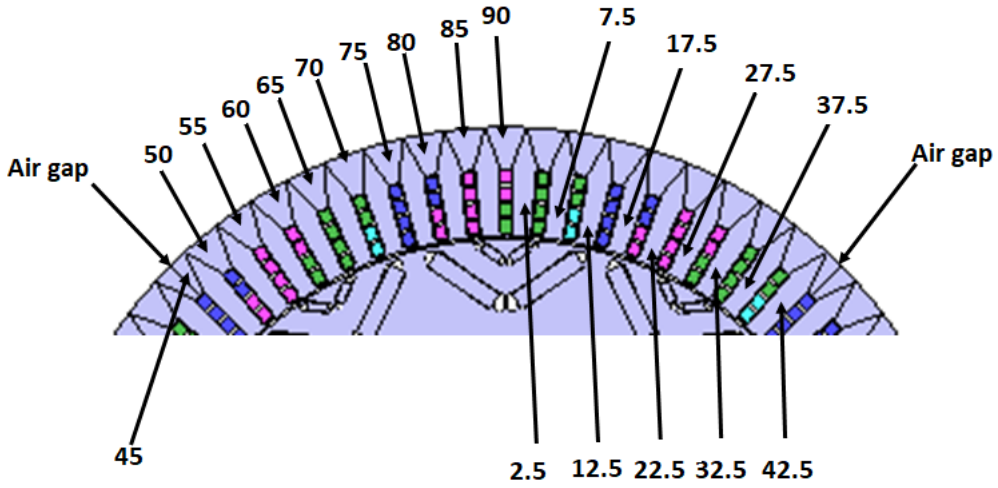

Figure A.4: One section of piecewise isotropic model selected from [40] with each number corresponds to the angle away from the rolling direction that uses the magnetic properties of the oriented steel for that angle

To estimate the accuracy of the selected model for the machine following two models were compared:

1. Model A

Anisotropic model already in FEA uses the two parameters, rolling and transverse direction BH and loss curves. The properties of the directions between rolling and transverse directions are interpolated in FEA software

2. Model B

   The selected piecewise isotropic model in Fig.A.4 that uses the BH curves and loss curves of oriented steel at different directions with respect to rolling direction used by the FEA software.

So, models A and B essentially use the same BH and loss curves in different directions away from the rolling direction. The only difference between the two models is the error in predicting the direction of flux in the region where teeth meet the back iron in Model B.

The two models were compared at selected operating points of characterization [52]. The characterization was carried out for the following operating points:

- I_s, magnitude of stator current, was swept from 25 A to 200 A in steps of 25 A. (Total 8 values)
- δ, power angle, was swept from 90° to 180° in steps of 10°.(Total 10 values)
- The mechanical speed is constant at $\omega_m = 1000$ RPM

The total number of operating points is 80, 8 different currents and ten different values of power angle, at a constant mechanical speed of $\omega_m = 1000$ RPM. For each operating point, the absolute error value between the two models was calculated for the parameters, Torque, λ_d (d-axis flux), λ_q (q-axis flux), and core losses, at all 80 points.

For all four parameters Torque, λ_d (d-axis flux), λ_q (q-axis flux), and core losses, and at all 80 points of characterization, the absolute error between the models is within 5%

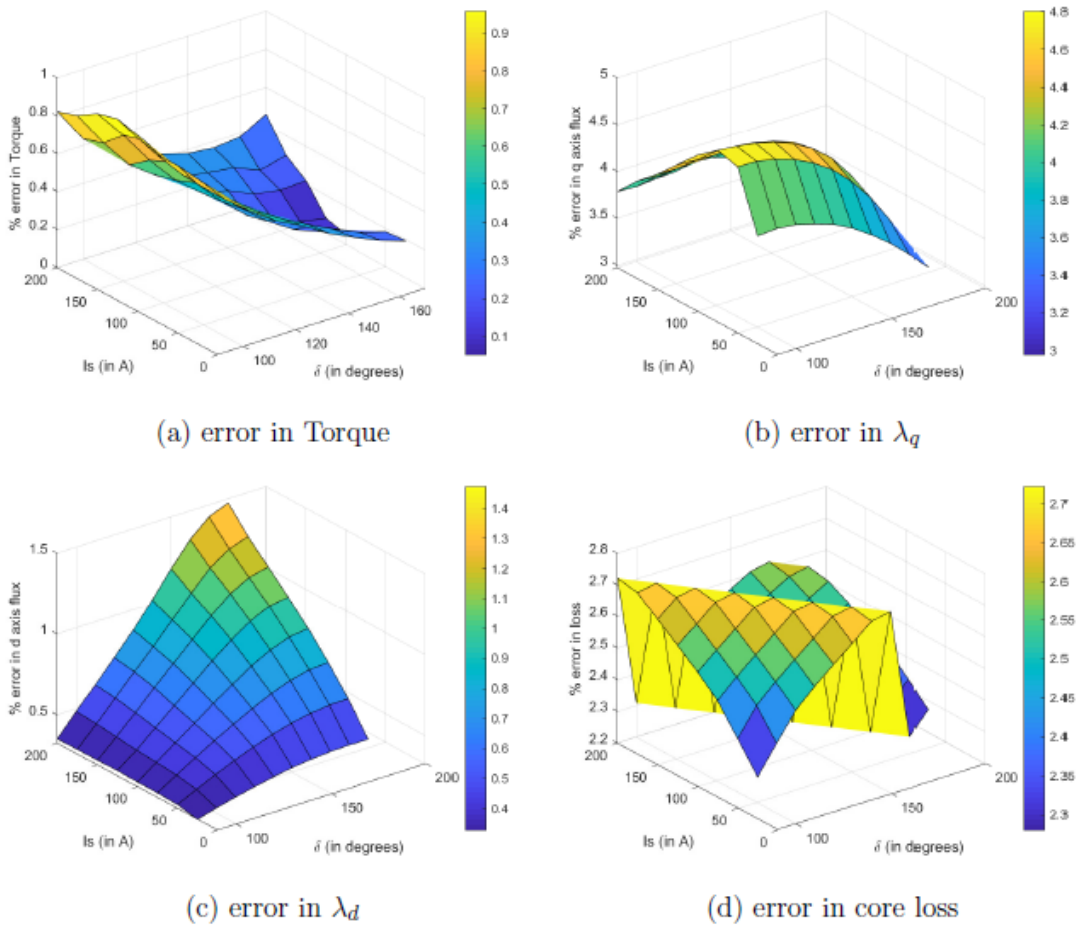

(a) error in Torque

(b) error in λ_q

(c) error in λ_d

(d) error in core loss

Figure A.5: Percentage error for Torque, q axis flux, d axis flux and core losses between the anisotropic model already in FEA and piecewise isotropic model using the magnetic characteristics of oriented steel used by FEA for all operating points used for characterization

error as shown in Fig.A.5. Therefore, the selected piecewise isotropic model for modeling of anisotropic steel model is correct. Moreover, the magnitude of error for the parameters above between the two models is sometimes positive or negative, which also shows that the error is random since the flux direction at the region where teeth meet the back iron changes with the operating conditions.

Appendix B

Data Filtering to Solve the Equations Proposed in Section 2.1

In order to eliminate the additional MMF drop and core losses due to parasitic gaps and extra cut edges, the matrices are redefined with lesser variables while still utilizing the symmetry of each segment. Fig.B.1 shows the line of symmetry, and all the symmetric back iron and teeth are colored with the same color to represent identical magnetic properties.

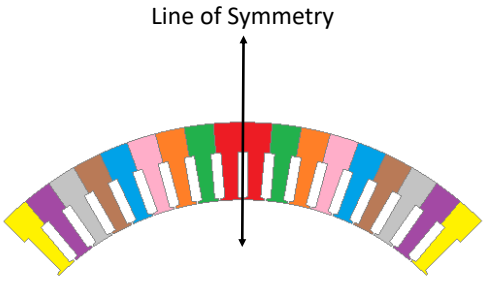

Figure B.1: One segment is shown with the line of symmetry which divides the segment into two identical halves

The division of the segmented stator into the small sections of back iron is shown in Fig.B.2. Again, the pairs of D_i are aligned identically with respect to the rolling direction and hence show similar magnetic properties.

The second identical small section is shown in Fig.B.3 which is the combination of teeth and portion of the back iron. To show the structure of this component, first, the whole segment is divided into black and white pieces where the black piece is the part of the back

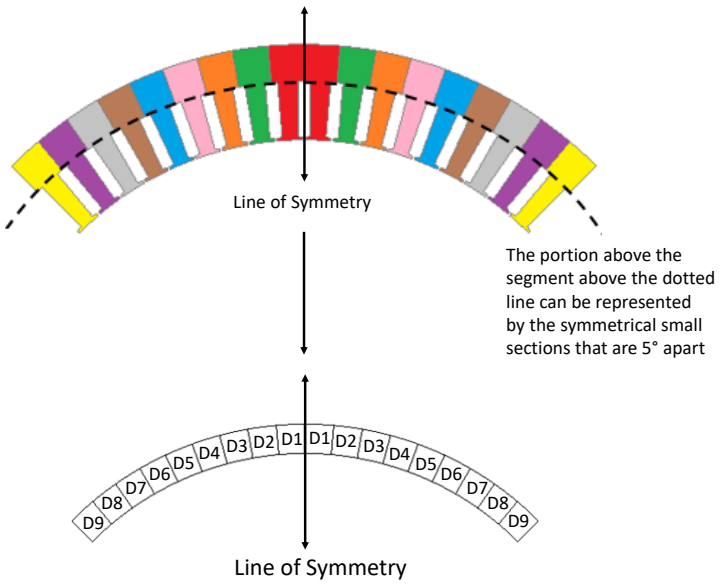

Figure B.2: The division of back iron of one segment based on symmetry

iron, and the white piece includes the teeth and portion of the back iron. Then this white and black portion is separated to obtain the white portion, as shown in Fig.B.3. Again the pairs of E_i shows identical magnetic properties due to the symmetry.

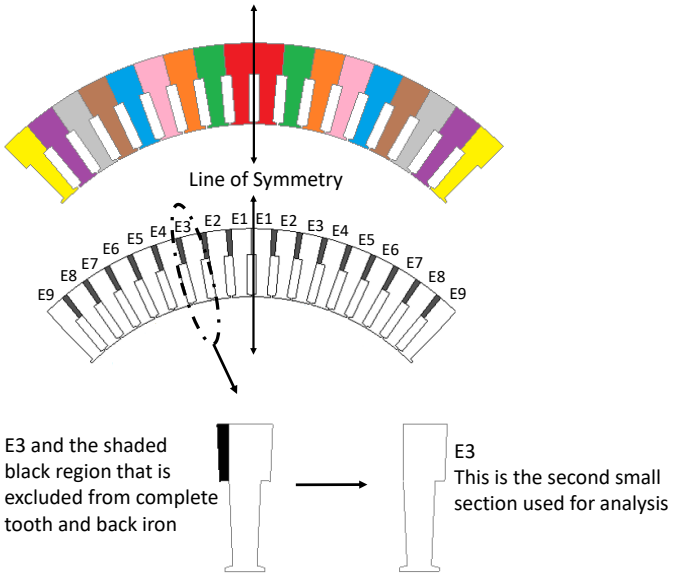

Figure B.3: Symmetrical component that consists of teeth and portion of back iron that is finally shown by E_3 excluding the black portion of the iron

D_i and E_i where the values of i vary from 1 to 9 where 1 is the closest position with

respect to the symmetrical axis as shown in Figs. B.2 and B.3. The stator contains 72 teeth; therefore, each segment is shifted by an angle 5° with respect to the adjacent segment.

The equations in matrix form for sensor A, B, and C, using the small sections D_i and E_i, are given as follows:

$$\begin{bmatrix} \hat{Y}_{A_1} \\ \hat{Y}_{A_2} \\ \hat{Y}_{A_3} \\ \hat{Y}_{A_4} \\ \hat{Y}_{A_5} \\ \hat{Y}_{A_6} \\ \hat{Y}_{A_7} \\ \hat{Y}_{A_8} \\ \hat{Y}_{A_9} \end{bmatrix} = \begin{bmatrix} 1 & 0 & 0 & 0 & 0 & 0 & 0 & 0 & 0 & 1 & 1 & 0 & 0 & 0 & 0 & 0 & 0 & 0 & 0 \\ 0 & 1 & 0 & 0 & 0 & 0 & 0 & 0 & 0 & 1 & 0 & 1 & 0 & 0 & 0 & 0 & 0 & 0 & 0 \\ 0 & 0 & 1 & 0 & 0 & 0 & 0 & 0 & 0 & 0 & 1 & 0 & 1 & 0 & 0 & 0 & 0 & 0 & 0 \\ 0 & 0 & 0 & 1 & 0 & 0 & 0 & 0 & 0 & 0 & 0 & 1 & 0 & 1 & 0 & 0 & 0 & 0 & 0 \\ 0 & 0 & 0 & 0 & 1 & 0 & 0 & 0 & 0 & 0 & 0 & 0 & 1 & 0 & 1 & 0 & 0 & 0 & 0 \\ 0 & 0 & 0 & 0 & 0 & 1 & 0 & 0 & 0 & 0 & 0 & 0 & 0 & 1 & 0 & 1 & 0 & 0 & 0 \\ 0 & 0 & 0 & 0 & 0 & 0 & 1 & 0 & 0 & 0 & 0 & 0 & 0 & 0 & 1 & 0 & 1 & 0 & 0 \\ 0 & 0 & 0 & 0 & 0 & 0 & 0 & 1 & 0 & 0 & 0 & 0 & 0 & 0 & 0 & 1 & 0 & 1 & 0 \\ 0 & 0 & 0 & 0 & 0 & 0 & 0 & 0 & 1 & 0 & 0 & 0 & 0 & 0 & 0 & 0 & 1 & 1 & 1 \end{bmatrix} \cdot K \tag{B.1}$$

where J is a column vector given by:

$$J^T = [Y_{D_1}\, Y_{D_2}\, Y_{D_3}\, Y_{D_4}\, Y_{D_5}\, Y_{D_6}\, Y_{D_7}\, Y_{D_8}\, Y_{D_9}\, Y_{E_1}\, Y_{E_2}\, Y_{E_3}\, Y_{E_4}\, Y_{E_5}\, Y_{E_6}\, Y_{E_7}\, Y_{E_8}\, Y_{E_9}\, Y_{ad}]$$

where Y_{ad} is the additional losses or MMF drop due to air gap and cut edges, also, the measured values of core losses and MMF drop are represented by a different symbol $\hat{Y}_{A_i}$ to show that the matrix incorporates Y_{ad} which was not included in Y_{A_i}. Similarly, for Sensor B and Sensor C, the two matrices are given as follows:

$$
\begin{bmatrix} \\ \hat{Y}_{B_1} \\ \\ \hat{Y}_{B_2} \\ \\ \hat{Y}_{B_3} \\ \\ \hat{Y}_{B_4} \\ \\ \hat{Y}_{B_5} \\ \\ \hat{Y}_{B_6} \\ \\ \hat{Y}_{B_7} \\ \\ \hat{Y}_{B_8} \\ \\ \hat{Y}_{B_9} \\ \\ \hat{Y}_{B_{10}} \\ \\ \end{bmatrix} = \begin{bmatrix} \\ 2\ 2\ 2\ 0\ 0\ 0\ 0\ 0\ 0\ 0\ 0\ 0\ 2\ 0\ 0\ 0\ 0\ 0\ 0 \\ \\ 2\ 2\ 1\ 1\ 0\ 0\ 0\ 0\ 0\ 0\ 0\ 1\ 0\ 1\ 0\ 0\ 0\ 0\ 0 \\ \\ 2\ 1\ 1\ 1\ 1\ 0\ 0\ 0\ 0\ 0\ 1\ 0\ 0\ 0\ 1\ 0\ 0\ 0\ 0 \\ \\ 1\ 1\ 1\ 1\ 1\ 1\ 0\ 0\ 0\ 1\ 0\ 0\ 0\ 0\ 0\ 1\ 0\ 0\ 0 \\ \\ 0\ 1\ 1\ 1\ 1\ 1\ 1\ 0\ 0\ 1\ 0\ 0\ 0\ 0\ 0\ 0\ 1\ 0\ 1 \\ \\ 0\ 0\ 1\ 1\ 1\ 1\ 1\ 1\ 0\ 0\ 1\ 0\ 0\ 0\ 0\ 0\ 0\ 1\ 1 \\ \\ 0\ 0\ 0\ 1\ 1\ 1\ 1\ 1\ 1\ 0\ 0\ 1\ 0\ 0\ 0\ 0\ 0\ 1\ 1 \\ \\ 0\ 0\ 0\ 0\ 1\ 1\ 1\ 1\ 2\ 0\ 0\ 0\ 1\ 0\ 0\ 0\ 1\ 0\ 1 \\ \\ 0\ 0\ 0\ 0\ 0\ 1\ 1\ 2\ 2\ 0\ 0\ 0\ 0\ 1\ 0\ 1\ 0\ 0\ 1 \\ \\ 0\ 0\ 0\ 0\ 0\ 0\ 2\ 2\ 2\ 0\ 0\ 0\ 0\ 0\ 2\ 0\ 0\ 0\ 1 \\ \\ \end{bmatrix} \cdot K \tag{B.2}
$$

$$\begin{bmatrix} \hat{Y}_{C_1} \\ \hat{Y}_{C_2} \\ \hat{Y}_{C_3} \\ \hat{Y}_{C_4} \\ \hat{Y}_{C_5} \\ \hat{Y}_{C_6} \\ \hat{Y}_{C_7} \\ \hat{Y}_{C_8} \\ \hat{Y}_{C_9} \end{bmatrix} = \begin{bmatrix} 2 & 2 & 2 & 2 & 2 & 2 & 1 & 0 & 0 & 0 & 0 & 0 & 0 & 0 & 0 & 1 & 1 & 0 & 0 \\ 2 & 2 & 2 & 2 & 2 & 1 & 1 & 1 & 0 & 0 & 0 & 0 & 0 & 0 & 1 & 0 & 0 & 1 & 0 \\ 2 & 2 & 2 & 2 & 1 & 1 & 1 & 1 & 1 & 0 & 0 & 0 & 0 & 1 & 0 & 0 & 0 & 1 & 1 \\ 2 & 2 & 2 & 1 & 1 & 1 & 1 & 1 & 2 & 0 & 0 & 0 & 1 & 0 & 0 & 0 & 1 & 0 & 1 \\ 2 & 2 & 1 & 1 & 1 & 1 & 1 & 2 & 2 & 0 & 0 & 1 & 0 & 0 & 0 & 1 & 0 & 0 & 1 \\ 2 & 1 & 1 & 1 & 1 & 1 & 2 & 2 & 2 & 0 & 1 & 0 & 0 & 0 & 1 & 0 & 0 & 0 & 1 \\ 1 & 1 & 1 & 1 & 1 & 2 & 2 & 2 & 2 & 1 & 0 & 0 & 0 & 1 & 0 & 0 & 0 & 0 & 1 \\ 0 & 1 & 1 & 1 & 2 & 2 & 2 & 2 & 2 & 1 & 0 & 0 & 1 & 0 & 0 & 0 & 0 & 0 & 1 \\ 0 & 0 & 1 & 2 & 2 & 2 & 2 & 2 & 2 & 0 & 1 & 1 & 0 & 0 & 0 & 0 & 0 & 0 & 1 \end{bmatrix} \cdot K \tag{B.3}$$

Let the matrices used in the in the equations B.1, B.2 and B.3 are denoted as A, B and C respectively. Also, the the column vector on the LHS of the equations B.1, B.2 and B.3 are denoted as $\hat{Y}_A$, $\hat{Y}_B$ and $\hat{Y}_C$ respectively. Therefore, the equations can be written in the combined form as:

$$\begin{bmatrix} \hat{Y}_A \\ \hat{Y}_B \\ \hat{Y}_C \end{bmatrix} = \begin{bmatrix} A \\ B \\ C \end{bmatrix} \cdot J \tag{B.4}$$

Further the combined matrix in (B.4) is written as:

$$L = \begin{bmatrix} A \\ B \\ C \end{bmatrix} \tag{B.5}$$

Since the matrix L is a full ranked matrix, the above set of equations can be solved by minimizing the following objective function using the NSGA algorithm shown in [53]:

$$\text{Objective Function} = \|L \cdot J - b\|$$

where b are the values MMF drop or core losses obtained by the experiments at all 28 positions, and where constraints are:

$$D_i > 0 \; E_i > 0$$

The solution provides all the values of Y_{E_i} and Y_{D_i}. Thereafter, using the values of Y_{E_i}

and Y_{D_i} the values of Y_{A_i}, Y_{B_i} and Y_{C_i} are calculated, and used in the equations 2.10, 2.11 and 2.12. Finally, solving the equations 2.10, 2.11 and 2.12 to calculate all the values of Y_{X_i} and Y_{T_j}. The flow of the process of data collection followed by data filtering, and finally data processing to calculate the core loss and MMF drop of X_i and T_i is shown in Fig.B.4.

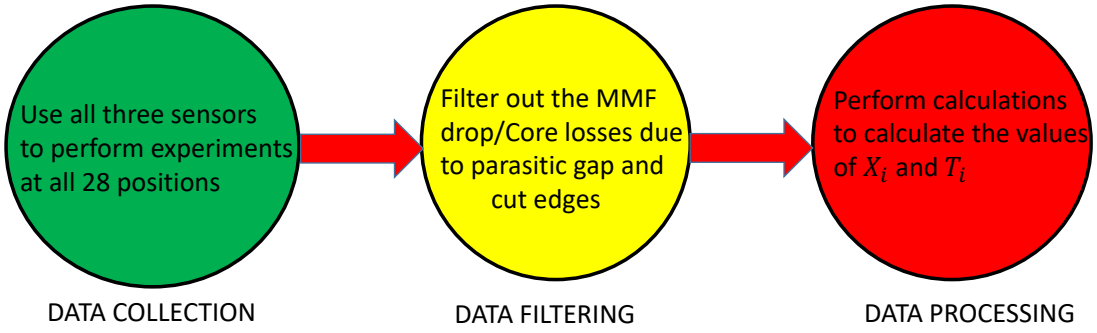

Figure B.4: The process of the data collection, data filtering and data processing

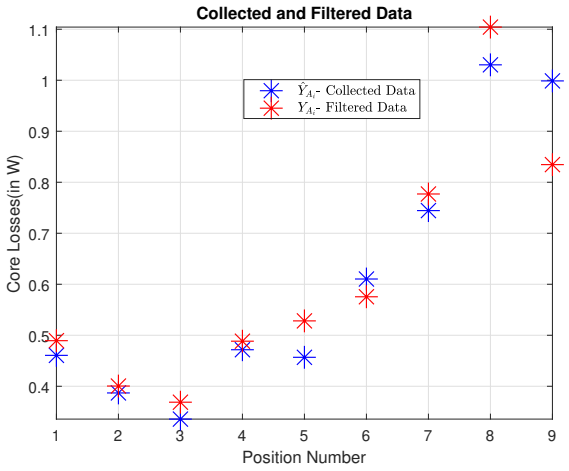

Figure B.5: Collected data and filtered data at different positions at $\hat{B}_{limb} = 1.5T$ and supply frequency of 50 Hz for sensor A

The analytical calculations were performed to obtain the values of E_i and D_i to filter out the additional MMF drop and losses. Finally, the individual values of E_i and D_i were used to obtain the values to Y_{A_i}, Y_{B_i} and Y_{C_i}. As expected there is a definite difference in the values of three set of pairs $\hat{Y}_{A_i}$-Y_{A_i}, $\hat{Y}_{B_i}$-Y_{B_i} and $\hat{Y}_{C_i}$- Y_{C_i}. Fig. B.5 shows the

difference between the core losses obtained from experiments before and after filtering at all nine positions for sensor A at 1.5 T and 50 Hz. The difference in the values for positions 1 to 8 is due to the error in the measurements among the three sensors and also due to slight changes in the symmetry. However, the difference is slightly on the higher side for position nine as it includes the additional loss component.

Appendix C

Steps to Calculate the MMF drop and Core Loss of Small Sections X_i, T_i and $\hat{T}_i$ Using the Developed Method

Core losses and MMF drop were measured for all three sensors at all unique positions in the sensor-stator arrangement as discussed in section 2.1. The data is collected at three different supply frequencies, which are 50Hz, 100 Hz, and 150 Hz. The values of flux densities at different levels of flux density, in the sensor limb, $\hat{B}_{limb}$, is shown in Table 2.3. These values are limited due to the supply current and voltage limitations of the experimental setup.

At the same levels of flux densities and frequencies, measurements were made using the sensor characterization setup. The core losses and MMF drop from the sensor characterization set up is subtracted from the core losses, and MMF drop from the sensor-stator arrangement data to obtain the values of $\hat{Y}_{A_i}$, $\hat{Y}_{B_i}$ and $\hat{Y}_{C_i}$, and the data is filtered. Thereafter, the obtained values of of Y_{A_i}, Y_{B_i} and Y_{C_i} are used to perform calculations using the equations in section 2.1, and the values of MMF drop and core losses are obtained for X_i and T_i at the selected operating points shown in Table 2.3. The summary of the data collection and calculation process is shown in Fig.C.1.

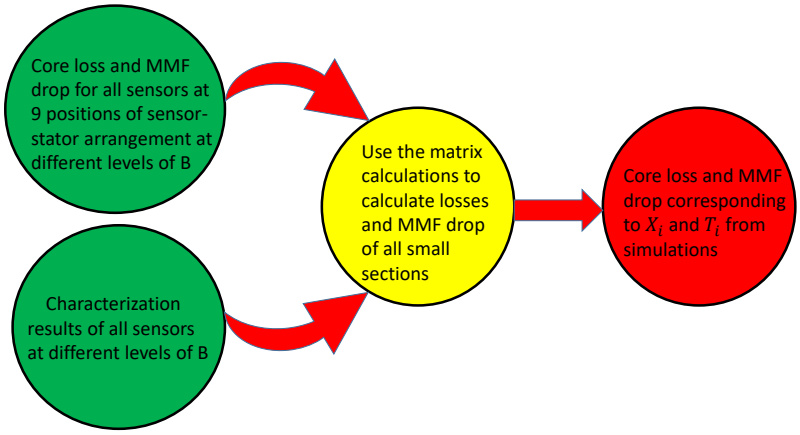

Figure C.1: Calculation of MMF drop and core losses for X_i and T_i at the selected operating points

The core losses and MMF drop data are obtained for individual values of X_i and T_i at different values of the peak of flux densities in the sensor limb ($\hat{B}_{limb}$). The data is adjusted from $\hat{B}_{limb}$ vs. core loss/MMF drop to:

1. $\hat{B}_{X_i}$ vs core loss/MMF drop of X_i.

2. $\hat{B}_{T_i}$ vs core loss/MMF drop of T_i.

where $\hat{B}_{X_i}$ and $\hat{B}_{T_i}$ are the values of peak flux density in X_i and T_i respectively. For small section X_i, the area of flux flow is uniform. Therefore, the relation between the flux densities is straightforward, considering the same amount of flux that goes from the limb of the sensor and small section X_i. The relationship is given as follows:

$$\Phi = \hat{B}_{X_i} \cdot A_{X_i} = \hat{B}_{limb} \cdot A_{limb} \tag{C.1}$$

where A_{X_i} and A_{limb} are the areas of the cross-section of X_i and limb, respectively. Since both areas are equal, the relationship between $\hat{B}_{X_i}$ and $\hat{B}_{limb}$ is:

$$\hat{B}_{X_i} = \hat{B}_{limb} \tag{C.2}$$

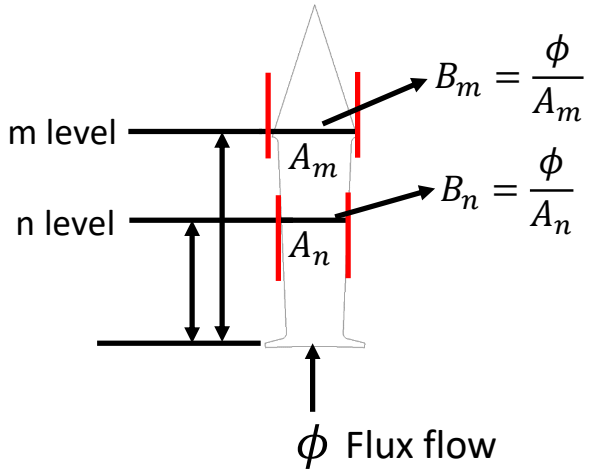

Figure C.2: Division of teeth in small areas to calculate the average flux in the teeth

For small section T_i, the area is not uniform, and hence flux densities are calculated at different areas along the flux flow direction, and the average of them is finally used as $\hat{B}_{T_i}$. Fig. C.2 shows the different levels at which flux density is calculated from the value of flux using the following equation:

$$\Phi = B_{nT_i} \cdot A_n = \hat{B}_{limb} \cdot A_{limb} \tag{C.3}$$

where n is the number of levels, $\hat{B}_{nT_i}$ is the peak of the flux density in T_i at n^{th} level and A_n is the area of the cross-section of T_i at n^{th} level. The higher the number of levels, the better the estimation. In this work total of 40 levels were considered, which are equally placed from the bottom of T_i. The estimated value of $\hat{B}_{T_i}$ is given as:

$$\hat{B}_{T_i} = \frac{\sum_{n=1}^{40} \hat{B}_{nT_i}}{40} \tag{C.4}$$

Rearranging equations C.3 and C.4 the following relation is obtained:

$$\hat{B}_{T_i} = \frac{\sum_{n=1}^{40} \frac{A_{limb}}{A_n}}{40} \cdot \hat{B}_{limb} \tag{C.5}$$

After performing the calculations using the geometry of the experimental set up the above relation reduces to:

$$\hat{B}_{T_i} = 1.4 \cdot \hat{B}_{limb} \tag{C.6}$$

Appendix D

Details of the Experimental Results

In this section, first, the characterization results for all three sensors are presented. The applicability of the proposed method is dependent on the symmetry of the oriented steel segment. Hence, the validation of the symmetry of the oriented steel is presented. The experiments were performed, and data were processed following the procedure discussed in section 2.1.2. Finally, the data is used to obtain the core losses and MMF drop of T_i and X_i.

Characterization Results

The characterization of the sensors was performed using the characterization setup discussed in section 2.2.2. The operating used for testing were as given in Table.2.3. As expected, the core losses and MMF drop-in sensor C is the highest, followed by sensor B, and finally sensor A; this is due to the relative difference in the size of the three sensors. The characterization results obtained for all three sensors at the selected operating points are shown in Fig.D.1.

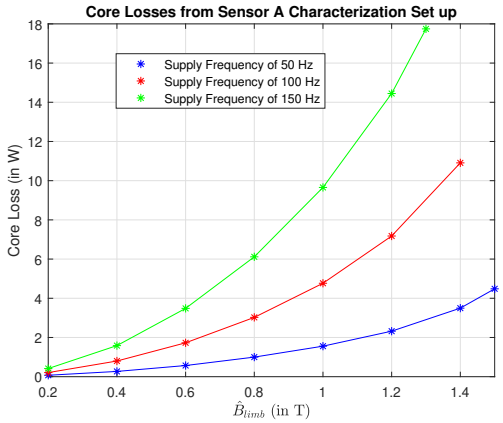

(a) Sensor A Loss Curves

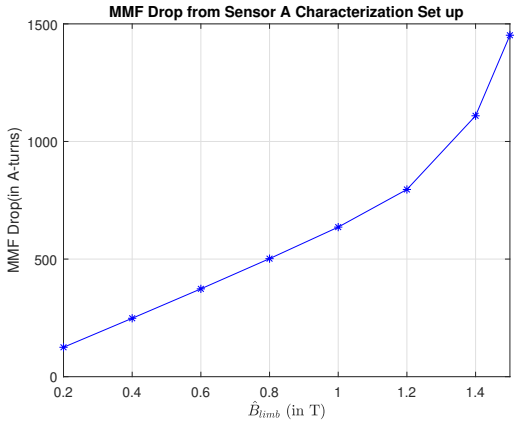

(b) Sensor A MMF Drop

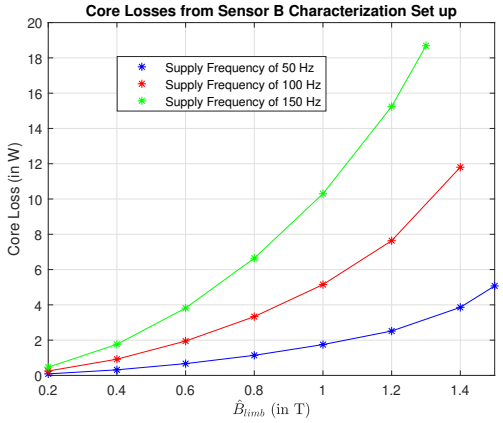

(c) Sensor B Loss Curves

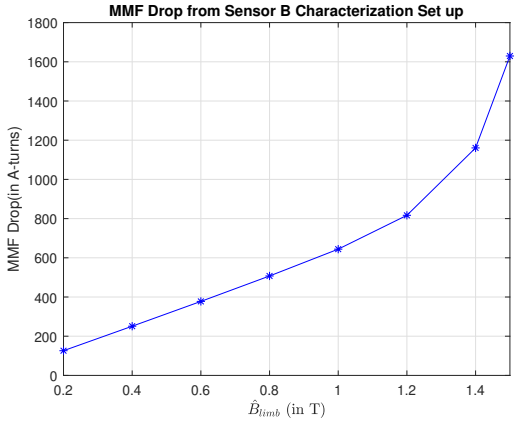

(d) Sensor B MMF Drop

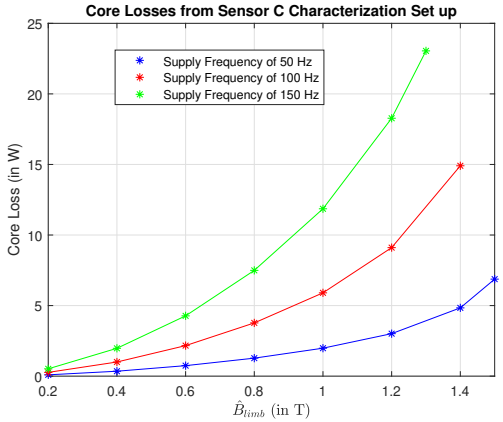

(e) Sensor C Loss Curves

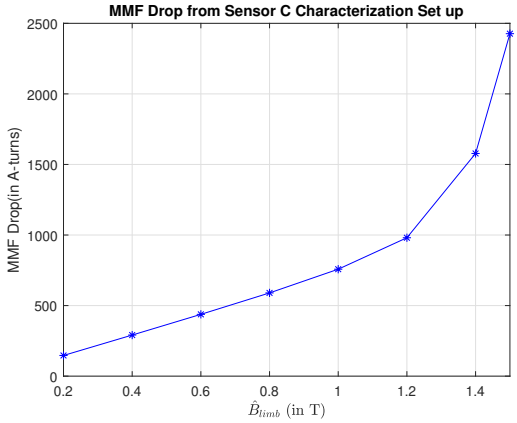

(f) Sensor C MMF Drop

Figure D.1: Characterization Results for sensor A, B and C at the selected operating points.

Proof of Symmetry

The symmetry is proven by calculating the losses using the sensor at two identical positions within a segment and identical positions in the adjacent two segments. The identical

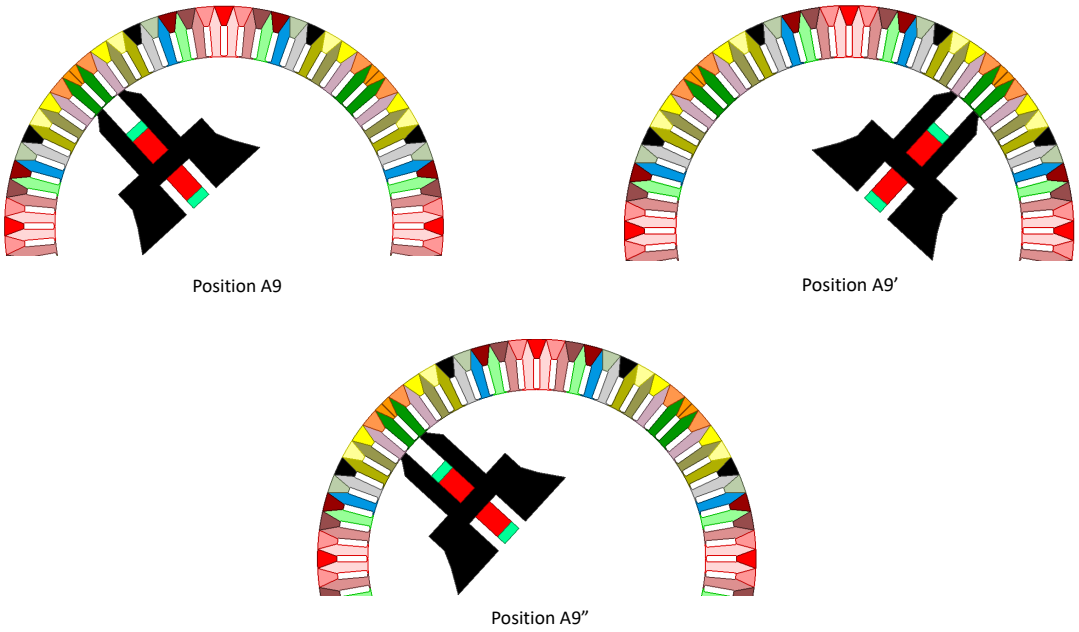

Figure D.2: Identical position within and between the segments.

position within the segment is denoted by sensor name followed by the position number followed by the symbol ', and the identical position in the adjacent segment is denoted by sensor name followed by the position number followed by the symbol ". For example for sensor A the identical position nine within the segment is denoted by $A_9^{'}$, and position in the other segment is denoted by $A_9^{"}$. Moreover, the measured values of core losses for the positions $A_9^{'}$ and $A_9^{"}$ are denoted by $Y_{A_9}^{'}$ and $Y_{A_9}^{"}$ respectively. The symmetrical positions within and the adjacent segment are shown in Fig.D.2.

It was validated that the segments are identified as the values of the measured core losses at identical positions both within and adjacent segments match the experimental error. The comparison of losses measured by sensor A at different identical positions within and adjacent segments is shown in Fig.D.3 at 1.5 T in the sensor limb at a supply frequency of 50 Hz.

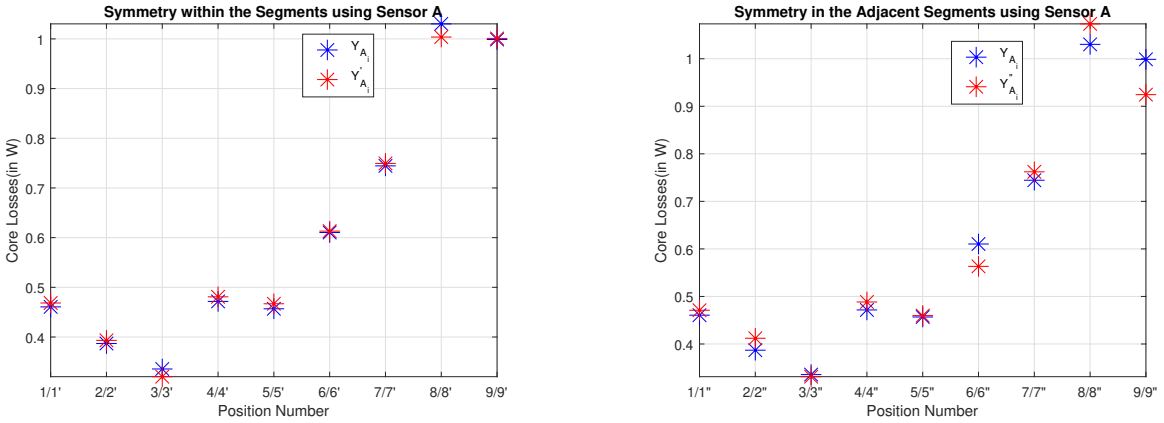

(a) Symmetry Within the segment

(b) Symmetry within adjacent segment

Figure D.3: Comparison of the core losses at $\hat{B}_{limb} = 1.5T$ and supply frequency of 50 Hz obtained at different positions within the segment and the adjacent segment using Sensor A.

Calculated Values of Core Loss and MMF Drop of X_i and T_i

The filtered data is used in equations 2.10, 2.11 and 2.12 to calculate the values of core losses and MMF drop of X_i and T_i. The following was observed from the processed data:

1. There is a decrease in core losses from X_1 to X_3, while an increase in core losses from X_3 to X_8, and again a decrease in core losses from X_9 to X_10 for all values of supply frequencies: 50Hz, 100Hz, and 150Hz.

2. Similar variation was observed for the MMF drop in X_i.

3. Moreover, there is almost no change in The core losses from T_1 to T_3. However, there is an increase in core loss from T_3 to T_9.

4. Similar variation was observed for the MMF drop in T_i.

The obtained values of core losses at 50 Hz for X_i and T_i is shown in Figs.D.4 and D.5 respectively.

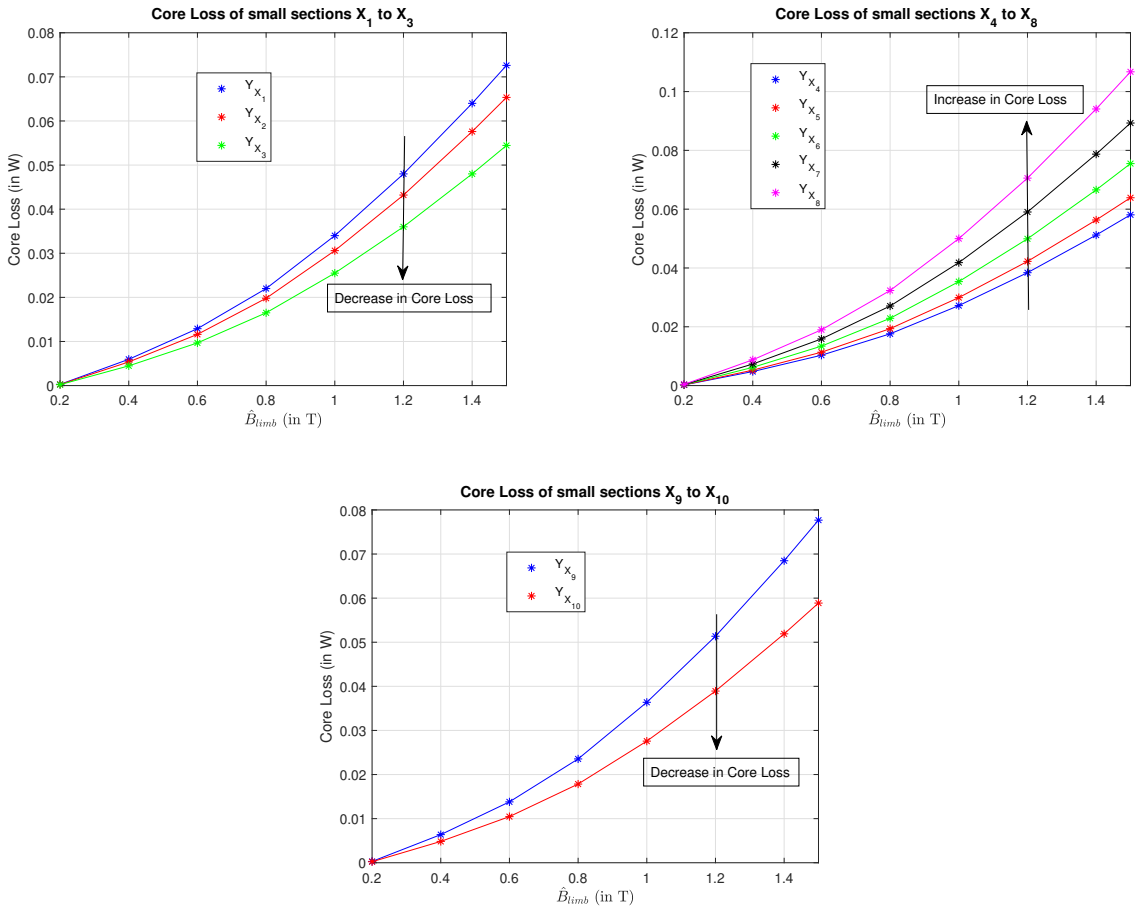

Figure D.4: Comparison of the core losses of X_i at the supply frequency of 50 Hz.

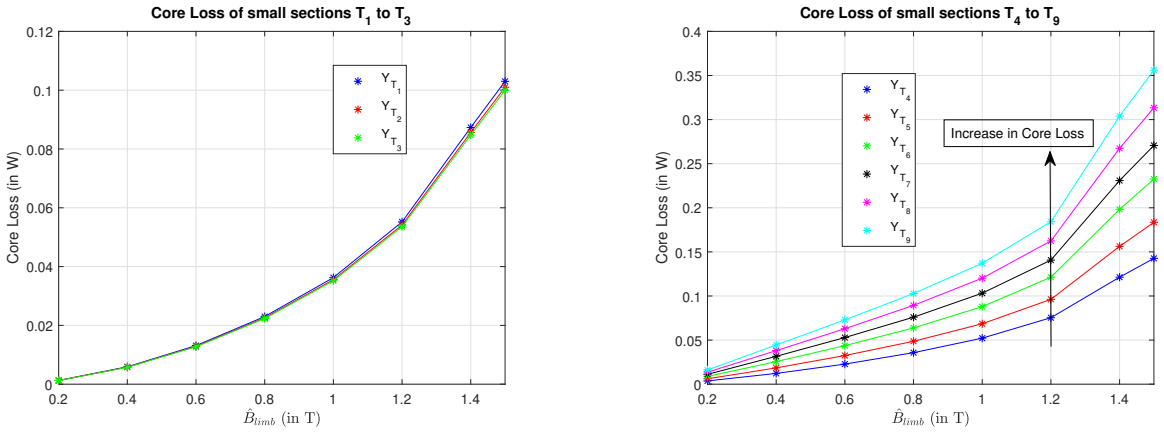

(a) (b)

Figure D.5: Comparison of the core losses of T_i at the supply frequency of 50 Hz.

BIBLIOGRAPHY

BIBLIOGRAPHY

[1] A. Aggarwal, E. G. Strangas, and A. Karlis, "Review of segmented stator and rotor designs for ac electric machines," in *2020 International Conference on Electrical Machines (ICEM)*, vol. 1, 2020, pp. 2342–2348.

[2] A. Aggarwal, E. G. Strangas, and J. Agapiou, "Analysis of unbalanced magnetic pull in pmsm due to static eccentricity," in *2019 IEEE Energy Conversion Congress and Exposition (ECCE)*, 2019, pp. 4507–4514.

[3] S. Huang, E. G. Strangas, A. Aggarwal, K. Li, and F. Niu, "Robust inter-turn short-circuit detection in pmsms with respect to current controller bandwidth," in *2019 IEEE Energy Conversion Congress and Exposition (ECCE)*, 2019, pp. 3897–3904.

[4] S. Huang, A. Aggarwal, E. G. Strangas, K. Li, F. Niu, and X. Huang, "Robust stator winding fault detection in pmsms with respect to current controller bandwidth," *IEEE Transactions on Power Electronics*, vol. 36, no. 5, pp. 5032–5042, 2021.

[5] A. Aggarwal, E. G. Strangas, and J. Agapiou, "Robust voltage based technique for automatic off-line detection of static eccentricity of pmsm," in *2019 IEEE International Electric Machines Drives Conference (IEMDC)*, 2019, pp. 351–358.

[6] A. Aggarwal, I. M. Allafi, E. G. Strangas, and J. S. Agapiou, "Off-line detection of static eccentricity of pmsm robust to machine operating temperature and rotor position misalignment using incremental inductance approach," *IEEE Transactions on Transportation Electrification*, vol. 7, no. 1, pp. 161–169, 2021.

[7] A. Aggarwal and E. G. Strangas, "Review of detection methods of static eccentricity for interior permanent magnet synchronous machine," *Energies*, vol. 12, no. 21, p. 4105, 2019.

[8] A. Aggarwal, E. G. Strangas, and J. Agapiou, "Comparative study of offline detection methods of static eccentricity for interior permanent magnet synchronous machine," in *2019 IEEE 12th International Symposium on Diagnostics for Electrical Machines, Power Electronics and Drives (SDEMPED)*, 2019, pp. 75–81.

[9] S. Huang, A. Aggarwal, E. G. Strangas, B. Khoshoo, K. Li, and F. Niu, "Mitigation of interturn short-circuits in ipmsm by using mtpcc control adaptive to fault severity," *IEEE Transactions on Power Electronics*, pp. 1–1, 2021.

[10] G.-J. Li, Z.-Q. Zhu, M. P. Foster, D. A. Stone, and H.-L. Zhan, "Modular permanent-magnet machines with alternate teeth having tooth tips," *IEEE Transactions on Industrial Electronics*, vol. 62, no. 10, pp. 6120–6130, 2015.

[11] T. Tomida, N. Sano, S. Hinotani, K. Fujiwara, H. Kotera, N. Nishiyama, and Y. Ikkai, "Application of fine-grained doubly oriented electrical steel to IPM synchronous motor," *IEEE Transactions on Magnetics*, vol. 41, no. 10, pp. 4063–4065, Oct 2005.

[12] Y. Sugawara and K. Akatsu, "Characteristics of a switched reluctance motor using grain-oriented electric steel sheet," in *2013 International Conference on Electrical Machines and Systems (ICEMS)*, Oct 2013, pp. 18–23.

[13] J. Ma, J. Li, H. Fang, Z. Li, Z. Liang, Z. Fu, L. Xiao, and R. Qu, "Optimal design of an axial-flux switched reluctance motor with grain-oriented electrical steel," *IEEE Transactions on Industry Applications*, vol. 53, no. 6, pp. 5327–5337, 2017.

[14] J. Rens, S. Jacobs, L. Vandenbossche, and E. Attrazic, "Effect of stator segmentation and manufacturing degradation on the performance of ipm machines, using icare® electrical steels," *World Electric Vehicle Journal*, vol. 8, no. 2, p. 450–460, Jun 2016.

[15] Y. Y. Du, Y. Sun, X. L. Zhu, M. Cheng, F. Xiao, and H. S. Zhu, "Comparison of doubly salient permanent magnet machines with e-shaped and -shaped stator iron core segments," *2015 IEEE Magnetics Conference (INTERMAG)*, pp. 1–1, 2015.

[16] Y. Sun and J. Shen, "Extra end effect of axially segmented stator core of high speed high power permanent magnet electric machines," in *2017 20th International Conference on Electrical Machines and Systems (ICEMS)*, Aug 2017, pp. 1–6.

[17] J. Ma, J. Li, H. Fang, Z. Li, Z. Liang, Z. Fu, L. Xiao, and R. Qu, "Optimal design of an axial-flux switched reluctance motor with grain-oriented electrical steel," *IEEE Transactions on Industry Applications*, vol. 53, no. 6, pp. 5327–5337, 2017.

[18] W. Ding, Y. Hu, H. Fu, and Q. Chen, "Evaluation of a segmented-stator hybrid excitation switched reluctance machine with permanent magnets for electric vehicles," in *2016 Eleventh International Conference on Ecological Vehicles and Renewable Energies (EVER)*, April 2016, pp. 1–8.

[19] O. Kaneki, T. Higuchi, Y. Yokoi, T. Abe, Y. Miyamoto, and M. Ohto, "Performance of segment type switched reluctance motor using grain-oriented," in *2012 15th International Conference on Electrical Machines and Systems (ICEMS)*, Oct 2012, pp. 1–4.

[20] C. A. Lopez, W. R. Jensen, S. Hayslett, S. N. Foster, and E. G. Strangas, "A review of control methods for PMSM torque ripple reduction," in *2018 XIII International Conference on Electrical Machines (ICEM)*, Sep. 2018, pp. 521–526.

[21] Z. Q. Zhu, Z. Azar, and G. Ombach, "Influence of additional air gaps between stator segments on cogging torque of permanent-magnet machines having modular stators," *IEEE Transactions on Magnetics*, vol. 48, no. 6, pp. 2049–2055, June 2012.

[22] N. J. Baker, D. J. B. Smith, M. C. Kulan, and S. Turvey, "Design and performance of a segmented stator permanent magnet alternator for aerospace," *IEEE Transactions on Energy Conversion*, vol. 33, no. 1, pp. 40–48, 2018.

[23] J. Le Besnerais, "Effect of lamination asymmetries on magnetic vibrations and acoustic noise in synchronous machines," in *2015 18th International Conference on Electrical Machines and Systems (ICEMS)*, 2015, pp. 1729–1733.

[24] J. L. Besnerais, V. Lanfranchi, M. Hecquet, P. Brochet, and G. Friedrich, "Acoustic noise of electromagnetic origin in a fractional-slot induction machine," *Compel-the International Journal for Computation and Mathematics in Electrical and Electronic Engineering*, vol. 27, pp. 1033–1052, 2008.

[25] R. Penin, J. . Lecointe, G. Parent, J. . Brudny, and T. Belgrand, "Estimation of relative magnetostriction and maxwell's forces in stacked grain oriented steel structures," in *2012 XXth International Conference on Electrical Machines*, 2012, pp. 1971–1976.

[26] G. Dajaku and D. Gerling, "Low costs and high-efficiency electric machines," in *2012 2nd International Electric Drives Production Conference (EDPC)*, Oct 2012, pp. 1–7.

[27] G. J. Li, Z. Q. Zhu, M. Foster, and D. Stone, "Comparative studies of modular and unequal tooth pm machines either with or without tooth tips," *IEEE Transactions on Magnetics*, vol. 50, no. 7, pp. 1–10, July 2014.

[28] G. J. Li, Z. Q. Zhu, W. Q. Chu, M. P. Foster, and D. A. Stone, "Influence of flux gaps on electromagnetic performance of novel modular pm machines," *IEEE Transactions on Energy Conversion*, vol. 29, no. 3, pp. 716–726, Sep. 2014.

[29] G. Li, Z. Zhu, M. P. Foster, D. A. Stone, and H. Zhan, "Modular permanent-magnet machines with alternate teeth having tooth tips," *IEEE Transactions on Industrial Electronics*, vol. 62, no. 10, pp. 6120–6130, Oct 2015.

[30] A. Nollau and D. Gerling, "Novel cooling methods using flux-barriers," in *2014 International Conference on Electrical Machines (ICEM)*, Sep. 2014, pp. 1328–1333.

[31] L. Vandenbossche, S. Jacobs, D. Van Hoecke, B. Weber, E. Leunis, and E. Attrazic, "Improved iron loss modelling approach for advanced electrical steels operating at high frequencies and high inductions in automotive machines," in *2012 2nd International Electric Drives Production Conference (EDPC)*, Oct 2012, pp. 1–8.

[32] L. Vandenbossche, S. Jacobs, F. Henrotte, and K. Hameyer, "Impact of cut edges on magnetization curves and iron losses in e-machines for automotive traction," *World Electric Vehicle Journal*, vol. 4, no. 3, p. 587–596, Sep 2010.

[33] T. Nakata, M. Nakano, and K. Kawahara, "Effects of stress due to cutting on magnetic characteristics of silicon steel," *IEEE Translation Journal on Magnetics in Japan*, vol. 7, no. 6, pp. 453–457, June 1992.

[34] A. Moses, N. Derebasi, G. Loisos, and A. Schoppa, "Aspects of the cut-edge effect stress on the power loss and flux density distribution in electrical steel sheets," *Journal of Magnetism and Magnetic Materials*, vol. 215-216, pp. 690 – 692, 2000.

[35] G. Crevecoeur, P. Sergeant, L. Dupre, L. Vandenbossche, and R. Van de Walle, "Analysis of the local material degradation near cutting edges of electrical steel sheets," *IEEE Transactions on Magnetics*, vol. 44, no. 11, pp. 3173–3176, Nov 2008.

[36] A. Peksoz, S. Erdem, and N. Derebasi, "Mathematical model for cutting effect on magnetic flux distribution near the cut edge of non-oriented electrical steels," *Computational Materials Science*, vol. 43, no. 4, pp. 1066 – 1068, 2008.

[37] Y. Kashiwara, H. Fujimura, K. Okamura, K. Imanishi, and H. Yashiki, "Estimation model for magnetic properties of stamped electrical steel sheet," *Electrical Engineering in Japan*, vol. 183, no. 2, pp. 1–11, 2013.

[38] F. Ossart, E. Hug, O. Hubert, C. Buvat, and R. Billardon, "Effect of punching on electrical steels: Experimental and numerical coupled analysis," *IEEE Transactions on Magnetics*, vol. 36, no. 5, pp. 3137–3140, Sep. 2000.

[39] L. Vandenbossche, S. Jacobs, X. Jannot, M. McClelland, J. Saint-Michel, and E. Attrazic, "Iron loss modelling which includes the impact of punching, applied to high-efficiency induction machines," in *2013 3rd International Electric Drives Production Conference (EDPC)*, Oct 2013, pp. 1–10.

[40] J. Maraví-Nieto, Z. Azar, A. Thomas, and Z. Zhu, "Utilisation of grain-oriented electrical steel in permanent magnet fractional-slot modular machines," *The Journal of Engineering*, vol. 2019, pp. 3682–3686, 2019.

[41] A. Aggarwal, M. Meier, E. Strangas, and J. Agapiou, "Analysis of modular stator pmsm manufactured using oriented steel," *Energies*, vol. 14, p. 6583, 2021.

[42] S. Nazrulla, E. G. Strangas, J. S. Agapiou, and T. A. Perry, "A device for the study of electrical steel losses in stator lamination stacks," *IEEE Transactions on Industrial Electronics*, vol. 61, no. 5, pp. 2217–2224, 2014.

[43] K. Jeong, Z. Ren, H. Yoon, and C. Koh, "Measurement of stator core loss of an induction motor at each manufacturing process," *Journal of Electrical Engineering & Technology*, vol. 9, pp. 1309–1314, 2014.

[44] G. J. Li, Z. Q. Zhu, M. Foster, and D. Stone, "Comparative studies of modular and unequal tooth pm machines either with or without tooth tips," *IEEE Transactions on Magnetics*, vol. 50, no. 7, pp. 1–10, 2014.

[45] D. Wang, X. Wang, Y. Yang, and R. Zhang, "Optimization of magnetic pole shifting to reduce cogging torque in solid-rotor permanent-magnet synchronous motors," *IEEE Transactions on Magnetics*, vol. 46, no. 5, pp. 1228–1234, 2010.

[46] Z. Q. Zhu and D. Howe, "Influence of design parameters on cogging torque in permanent magnet machines," *IEEE Transactions on Energy Conversion*, vol. 15, no. 4, pp. 407–412, 2000.

[47] S. Hayslett and E. Strangas, "Analytical design of sculpted rotor interior permanent magnet machines," *Energies*, vol. 14, no. 16, p. 5109, 2021.

[48] J. X. Shen, S. Cai, J. Yuan, S. Cao, and C. W. Shi, "Cogging torque in spm machine with segmented stator," *COMPEL - The international journal for computation and mathematics in electrical and electronic engineering*, vol. 35, no. 2, pp. 641–654, 2016.

[49] N. Bianchi and S. Bolognani, "Design techniques for reducing the cogging torque in surface-mounted PM motors," *IEEE Transactions on Industry Applications*, vol. 38, no. 5, pp. 1259–1265, 2002.

[50] U. S. E. P. Agency. (2021) Dynamometer drive schedules. [Online]. Available: http://https://www.epa.gov/vehicle-and-fuel-emissions-testing/dynamometer-drive-schedules,urldate={03-21-2021}

[51] K. H. Nam, "Ac motor control and electrical vehicle applications," in *CRC Press Taylor and Francis Group*, 2019, pp. 489–511.

[52] J. G. Cintron-Rivera, A. S. Babel, E. E. Montalvo-Ortiz, S. N. Foster, and E. G. Strangas, "A simplified characterization method including saturation effects for permanent magnet machines," in *2012 XXth International Conference on Electrical Machines*, 2012, pp. 837–843.

[53] N. Srinivas and K. Deb, "Muiltiobjective optimization using nondominated sorting in genetic algorithms," *Evolutionary Computation*, vol. 2, no. 3, pp. 221–248, 1994.